

BANGLADESH UNIVERSITY OF ENGINEERING AND TECHNOLOGY

**DESIGN AND ANALYSIS OF EFFICIENT AND  
TUNABLE PLASMONIC LASERS WITH  
DIRECTIONAL RADIATION**

*by*

**Zabir Ahmed**

Student ID: 1014062214 P


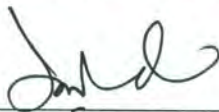

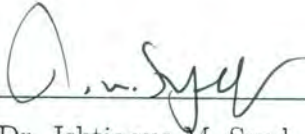
*A thesis submitted in partial fulfillment of the requirements  
for the degree of Masters of Science  
in the  
Department of Electrical and Electronic Engineering*

August 2016

# Approval

This thesis titled “**DESIGN AND ANALYSIS OF EFFICIENT AND TUN-  
ABLE PLASMONIC LASERS WITH DIRECTIONAL RADIATION**” sub-  
mitted by Zabir Ahmed, Student No: 1014062214 P, Session: October/2014, has been  
accepted as satisfactory in partial fulfillment of the requirements for the degree of  
Master of Science in Electrical and Electronic Engineering on August 29, 2016.

## Board of Examiners:

1.   
\_\_\_\_\_  
Dr. Muhammad Anisuzzaman Talukder  
Professor  
Department of EEE, BUET, Dhaka.  
Chairman  
(Supervisor)
2.   
\_\_\_\_\_  
Dr. Quazi Deen Mohd Khosru  
Professor and Head  
Department of EEE, BUET, Dhaka.  
Member  
(Ex-Officio)
3.   
\_\_\_\_\_  
Dr. Md. Zahurul Islam  
Associate Professor  
Department of EEE, BUET, Dhaka.  
Member
4.   
\_\_\_\_\_  
Dr. Ishtiaque M. Syed  
Professor  
Department of Physics, University of Dhaka, Dhaka.  
Member  
(External)

# Declaration of Authorship

I, Zabir Ahmed, declare that this thesis titled, "DESIGN AND ANALYSIS OF EFFICIENT AND TUNABLE PLASMONIC LASERS WITH DIRECTIONAL RADIATION" and the work presented in it are my own. I confirm that:

- This work was done wholly or mainly while in candidature for a degree at this University.
- Where I have consulted the published work of others, this is always clearly attributed.
- Where I have quoted from the work of others, the source is always given. With the exception of such quotations, this thesis is entirely my own work.
- I have acknowledged all main sources of help.

Signed:



---

(Zabir Ahmed)

# Acknowledgment

First, I would like to express my gratitude towards the Almighty Allah for the strength, courage, and perseverance that He has bestowed throughout my academic life. I am thankful to Him for whatever I have achieved thus far in my educational pursuit. Next, I would like to express gratitude towards my thesis supervisor, Dr. Muhammad Anisuzzaman Talukder for the patient guidance, encouragement, and advice that he has provided throughout the time I have been his student. I consider myself extremely lucky to have such a wise, inspiring, and helpful supervisor who not only answered all the questions and queries and but also provided ample computational resources to aid my research endeavor. I will always be grateful to him for introducing me to the world of research and teaching a systematic approach towards research work.

Completing this thesis work would have been all the more difficult were it not for the continuous help and support I received from fellow researchers in ‘Photonics Lab’: Avijit Das, Rifat Kaiser, Sakib Hassan, and Mehedi Hasan.

I would like to take this opportunity to thank my parents for their love, guidance, and influence. Their belief in me has always been the source of strength in the most trying times.

# Contents

<b>Acknowledgment</b>	<b>1</b>
<b>1 Introduction</b>	<b>1</b>
1.1 Plasmonic Nanolaser: Current Progress . . . . .	2
1.2 Challenges in Plasmonic Nanolaser Design . . . . .	4
1.3 Overview of Thesis . . . . .	5
<b>2 Plasmonics</b>	<b>7</b>
2.1 Dielectric Function of Metals . . . . .	7
2.2 Surface Plasmon Polariton . . . . .	9
2.2.1 SPP at Single Metal/Dielectric Interface . . . . .	9
2.3 Localized Surface Plasmon . . . . .	13
2.3.1 Excitation of LSP . . . . .	14
2.3.2 Dependence on Dielectric Medium and Particle Shape . . . . .	15
2.4 Prospect of plasmonics . . . . .	17
2.5 Summary . . . . .	18
<b>3 Numerical Simulation Methodology</b>	<b>19</b>
3.1 Finite Difference Time Domain Model . . . . .	20
3.2 Boundary Conditions . . . . .	21

3.2.1	Perfectly Matched Layer . . . . .	21
3.2.2	Periodic and Bloch Boundary Condition . . . . .	22
3.2.3	Determining Spatial and Temporal Cell Size . . . . .	23
3.3	Dispersive Material Modeling . . . . .	24
3.4	Gain Medium Modeling . . . . .	26
3.4.1	Four Level Two Electron System . . . . .	26
3.5	Simulation of a Photonic Cavity Laser . . . . .	29
3.6	Summary . . . . .	35
<b>4</b>	<b>Design of Plasmonic Nanolaser</b>	<b>37</b>
4.1	Plasmonic Nanocavity Design . . . . .	38
4.2	Plasmonic Crystal Based Nanocavity . . . . .	40
4.2.1	Extraordinary Transmission . . . . .	42
4.2.2	Mechanisms of EOT . . . . .	43
4.3	Improving Nanocavity Response . . . . .	51
4.3.1	Optical Tamm State . . . . .	52
4.3.2	Optical Tamm State Enhanced Transmission through Sub-wavelength Hole Array . . . . .	55
4.4	Summary . . . . .	59
<b>5</b>	<b>Proposed Nanolaser</b>	<b>61</b>
5.1	Nanolaser Design and Simulation Setup . . . . .	62
5.2	Performance Analysis . . . . .	65
5.3	Effect of 1D PhC . . . . .	67
5.4	Tuning Mechanisms of Emission Wavelength . . . . .	71
5.4.1	Terminating TiO <sub>2</sub> Layer Thickness . . . . .	72
5.4.2	Gain Layer Thickness . . . . .	73
5.4.3	Nanohole Depth and Width . . . . .	74

<i>CONTENTS</i>	4
5.4.4 Angle of Incidence of Pump Pulse . . . . .	75
5.4.5 Polarization of Incident Pump Pulse . . . . .	76
5.5 Far-field Directionality . . . . .	76
5.6 Summary . . . . .	82
<b>6 Conclusion and Future Works</b>	<b>83</b>
6.1 Future Works . . . . .	85

# List of Figures

2.1	Propagation geometry at Air/Metal interface. . . . .	10
2.2	Dispersion relation of SPPs at the interface between a Drude metal with negligible collision frequency and air (gray curves) and silica (black curves) [22]. . . . .	11
2.3	Dispersion relation of SPPs at a silver/air (gray curve) and silver/silica (black curve) interface. Due to the damping, the wave vector of the bound SPPs approaches a finite limit at the surface plasmon frequency [22]. . . . .	12
2.4	An evanescent wave propagating along the interface of a metal and a dielectric. Electric field component along z-axis decays exponentially [23].	13
2.5	Mechanism of localised surface plasmon resonance [23]. . . . .	14
2.6	Scattering spectra of Ag nano-particles of different shapes [27]. . . . .	16
3.1	Yee grid in three dimensional simulation domain. . . . .	21
3.2	Fitting of Au permittivities with multi-coefficient material model. . .	25
3.3	4 level 2 electron system . . . . .	27
3.4	Schematic of a simple photonic cavity laser. A gain medium is placed between two DBRs. . . . .	29
3.5	Amplitude envelop of the electromagnetic wave used to optically pump the photonic cavity laser. . . . .	30



3.6	Time evolution of normalized populations in the four levels of the laser gain medium. . . . .	31
3.7	Time evolution of normalized populations in two lasing levels of the laser gain medium. . . . .	32
3.8	Emission spectra along with the frequency domain filters to extract pump and lasing emission. . . . .	33
3.9	Extracted pump signal and lasing signal on the output side of the photonic cavity laser. . . . .	34
3.10	Emission intensity of the photonic cavity laser as pumping intensity is increased. . . . .	35
4.1	Schematic of a simplified lattice plasmon based nanolaser structure.	40
4.2	(a) Far-field pattern observed in reflection side. (b) Emission spectra recorded in transmission and reflection side. . . . .	41
4.3	Au nanohole array with square holes demonstrating extraordinary transmission. . . . .	43
4.4	EOT spectra for square and circular holes. . . . .	45
4.5	Electric field intensity at surface of the nanohole at resonant wavelength of extraordinary transmission. . . . .	46
4.6	Transmission spectra of nanohole array for different square hole dimensions. The sub-wavelength array consists of square holes with period of 350 nm on 100 nm thick Au layer. . . . .	47
4.7	Transmission spectra of nanohole array for different metal thicknesses. The sub-wavelength array consists of 170 nm $\times$ 170 nm square holes with period of 350 nm. . . . .	48
4.8	Schematic of EOT-based nanocavity. . . . .	49

4.9	Emission spectra at reflection and transmission side for the structure shown in Fig. 4.8. . . . .	50
4.10	Schematic of the structure demonstrating optical Tamm resonance. . . . .	52
4.11	Normalized reflection spectra of the OTS structure and 1D photonic crystal. . . . .	53
4.12	(a) Refractive index profile of the OTS structure. (b) Normalized electric field intensity distribution in OTS structure. . . . .	54
4.13	Reflection spectra demonstrating the behavior of OTS resonance as spacer thickness, $d_s$ and terminating $\text{TiO}_2$ thickness, $d_l$ are varied. . . . .	55
4.14	Cross-sectional view of the proposed nanohole array structure using 1D PhC. . . . .	56
4.15	Transmission spectra showing the increased transmission through nanohole array due to inclusion of 1D PhC. . . . .	57
4.16	Electric field intensity distribution throughout the structure with 1 dimensional photonic crystal on top of square nanohole array. . . . .	58
4.17	Normalized transmission spectra as spacer thickness, $d_s$ and terminating $\text{TiO}_2$ thickness, $d_l$ are varied. . . . .	59
5.1	Schematic of the Nanolaser structure consisting of 1D photonic crystal terminated by Au nanohole array with square holes. The 1D PhC is formed by alternating layers of $\text{TiO}_2$ and $\text{MgF}_2$ . Gain material thickness is 350 nm and metallic layer thickness is 100 nm. The holes have width and breadth of 170 nm and periodicity of 350 nm. . . . .	62
5.2	Cross-sectional view of unit cell of the proposed nanolaser structure. This section is taken through the center of the square nanohole. Here, $t_h = 100$ nm, $d_g = 325$ nm, $d_l = 200$ nm, $d_M = 165$ nm, $d_T = 108$ nm, $d_h = 170$ nm, $t_h = 100$ nm, and $\Lambda = 350$ nm. . . . .	63

5.3	Emission spectra for different pump intensities. . . . .	64
5.4	Emission characteristics of the nanolaser as a function of pumping amplitude. This laser shows threshold behavior at approximately $5 \times 10^7$ V/m of input pump amplitude. . . . .	65
5.5	Time evolution of normalized population densities of upper and lower lasing levels. This measurement is taken at a point 10 nm away from nanohole edge (a) for $0.8 \times$ pump threshold (b) for $1.2 \times$ pump threshold. . . . .	66
5.6	Emission spectra of of the proposed nanolaser structure for different number of 1D PhC layers. Here, $N =$ pairs of $\text{TiO}_2$ and $\text{MgF}_2$ layers in PhC. . . . .	68
5.7	Emission spectra for nanolaser structures with Au, Ag, and Silica nanohole array of the same dimension. . . . .	69
5.8	E-field intensity in the vicinity of the square hole array at lasing frequency(XY plane). (a) Bare plasmonic nanohole array structure (b) Proposed nanolaser structure with 1D PhC. . . . .	70
5.9	E-field intensity in the vicinity of the square hole array at lasing frequency(XZ plane). (a) Bare plasmonic nanohole array structure (b) Proposed nanolaser structure with 1D PhC. . . . .	70
5.10	Emission spectra of the laser for different $\text{TiO}_2$ layer thicknesses, $d_l$ . . . . .	72
5.11	Emission spectra of the laser for different gain material thicknesses, $d_g$ . . . . .	73
5.12	Effect of (a) hole depth and (b) hole width on lasing spectra. . . . .	74
5.13	Emission spectra of the laser for different angles of incidence. . . . .	75
5.14	Emission spectra of the laser for different polarizations of input pulse. . . . .	76
5.15	Far field E-field intensity distribution. Far-field simulations were run considering a structure of $70 \mu\text{m} \times 70 \mu\text{m}$ dimension with plane wave incident on the structure. . . . .	77
5.16	Far field E-field intensity distribution as a function of polar angle, $\theta$ . . . . .	78

5.17	Magnitudes of poynting vector recorded in near field monitor at lasing frequency. (a) magnitude of poynting vector (b-d) orthogonal components of poynting vector. . . . .	79
5.18	Vector diagram of the poynting vectors drawn on the plane of the near field monitor. . . . .	80
5.19	Far field distribution of at 800 nm wavelength for a structure with lattice period of 900 nm. . . . .	81

## Abstract

In this work, we propose room-temperature plasmonic crystal based nanolaser with low divergence emission. Usually, performance of nanolasers based on plasmonic crystal nanocavity is affected by a couple of issues: coupling of lasing emission to both reflection and transmission side of the device and multiple diffracted orders of lasing emission. In our proposed nanolaser design, we have overcome these bottlenecks to substantially increase the emission intensity and efficiency. Our proposed structure consists of periodic apertures in thin metallic film. In this design, feedback action necessary for lasing action is provided by localized hole resonance of the nanohole array. To improve the lasing intensity and efficiency, a one dimensional photonic crystal is incorporated on top of the metallic nanohole array. Under optical pumping, this photonic crystal structure excites optical Tamm states in the locality of the metal hole array. Field enhancement due to Tamm state results in pronounced amplification of extraordinary transmission leading to substantially increased lasing emission in near-IR wavelength. Moreover, the photonic bandgap of the crystal selectively guides laser emission towards the transmission side of the device. Due to sub-wavelength lattice period of the nanohole array, lasing emission is confined only to the zeroth order of diffracted mode. Resonant emission through each of the holes in periodic array interfere constructively to produce narrow-beam emission with low divergence in the direction normal to the nanolaser surface. Besides, emission peak wavelength of this nanolaser can be tuned in real-time by changing the angle of incidence. Moreover, the laser emission wavelength can be engineered over a broad range of wavelength by changing thicknesses of the photonic crystal layers.

# Chapter 1

## Introduction

In search of faster, smaller, and cheaper computational and communication tools, semiconductor devices research has undergone a number of breakthroughs. However, we have noticed that miniaturization of electronic devices is reaching its physical limits. With transistors of few nanometer dimensions, further reduction in size leads to exponential increase in fabrication cost and difficulty. As a result, keeping up with Moore's law is becoming increasingly challenging. To cope with this problem, researchers are looking into replacing electrons by photons of light. Doing so opens up multitudes of approaches to achieve faster speed and smaller size.

Computation and communication with light has the potential of breaking the barriers of current electronics. We have seen recent surge in the field of optical integrated circuits where photonic analog of electrical and electronic elements are implemented. For such devices, we need a coherent source of light, which has bolstered the research in the field of lasers. Laser technology has evolved from gas laser to semiconductor p-n junction lasers. After that, double heterostructure, quantum dot, quantum cascade lasers have been implemented [1]. Significant improvement in laser performance was brought about through discovery of distributed feedback lasers, vertical cavity surface emitting lasers, photonic crystal lasers, and many other types of lasers [2]. In

each of iterations of laser research, researchers have pursued to make the dimensions of lasers as small as possible. However, the laser structure consisting exclusively of dielectric material are fundamentally constrained by the diffraction limit. In other words, there is a physical limit that prevents such lasers to be smaller than half of the wavelength of operation [3]. To overcome this limit, novel waveguiding mechanism capable of coupling electromagnetic energy within subwavelength dimensions was explored. This endeavor has ushered in a new era of nanolasers using plasmonic or metal-optics. In this work, we present design and analysis of such a nanolaser based on plasmonic phenomena which can act as a nanoscale coherent light-source operating beyond diffraction limit.

## 1.1 Plasmonic Nanolaser: Current Progress

Plasmonics is a natural choice for coupling photons in nanoscale dimensions. Surface plasmon polariton (SPP) modes propagate along a flat metal-dielectric interface typically at visible or infrared wavelengths. Apart from flat metal-dielectric interface, other metal structures- metallic nano-particles, grooves, holes, gaps, and slits on metal films- can couple plasmonic mode. This plasmonic mode propagates via resonant energy transfer between electromagnetic wave and charge density wave in metal. Interaction with free electrons in metal causes plasmonic waves to dissipate energy which leads to exponential decaying along the propagation direction. This metallic loss is a fundamental property of plasmonic modes. To achieve lasing emission from plasmonic structure, the gain medium has to overcome these metallic losses.

The feasibility of stimulated emission from plasmonic structure was first theoretically proposed in 2003 [4]. It took until 2007 to experimentally demonstrate lasing in near infrared region using metallic structure [5]. This structure utilized

semiconductor-insulator-metal core-shell structure with electrical injection to produce lasing emission. Such structures supported hybrid mode with reasonable Q at the cryogenic temperature (77 K). Since then, various types of plasmonic nanolasers have been demonstrated and proposed.

A number of plasmonic laser and surface plasmon amplification structure is based on prism and grating coupling [6, 7]. First SPP lasing emission at optical wavelength was demonstrated using widely-known Kretschmann structure structures comprising 39 nm and 67 nm thick silver films on BK7 prisms with the other silver surface being in contact with the gain medium. The gain medium used in this device was Rhodamine 101 and cresyl violet in ethanol solution [8]. Similar structure, but with gain medium comprising a 10  $\mu\text{m}$  thick layer of poly(methyl methacrylate) (PMMA) was also reported to produce visible light stimulated emission [9].

Plasmonic lasing is also demonstrated on CdS<sub>2</sub> nanowire placed on Ag plate covered by Silica spacer layer. This structure facilitates occurrence of Fabry Perot mode along the longitudinal direction and confinement along radial direction through coupling of hybrid photonic-plasmonic mode. Lasing was observed around 490 nm under optical pumping in both room temperature and cryogenic temperature [10]. Similar structure with CdS<sub>2</sub> patch on top of Ag-SiO<sub>2</sub> was also reported by the same research group. Room temperature multimodal lasing was achieved when this device was optically pumped with Ti:sapphire laser [11]. Field localization of energy in cylindrical structures such as metal rods, or dielectric rods clad by a metal sheath has also been observed. SPP propagation in such structures with gain material has also been reported recently [12].

A number of plasmonic laser based on extraordinary transmission of light operating in optical communication wavelength has been proposed in last few years [13, 14]. In such structures, semiconductor gain medium deposited on top of metallic hole array provides loss compensation. Lasing emission at visible wavelength has also



been reported using Ag metallic hole array and R101-PVA gain layer [15]. Apart from nanohole array, other kinds of plasmonic crystals have been reported to produce lasing emission. In 2013, Zhou et. al. reported room temperature surface normal lasing action in strongly coupled plasmonic nanocavity array due to excitation of band-edge lattice plasmon modes [16]. Au nano-particle array surrounded by organic gain material (IR-140) produced lasing emission in near-IR regime. Similar structure using plasmonic bow-tie antenna was reported to produce lasing emission [17]. Off normal lasing emission from similar structure with plasmonic nanodome array has been studied as well [18].

Metal nano-particles shows exhibits resonant plasmonic modes known as localized surface plasmon resonance(LSP). The strength and spectral position of LSP depends on shape, size and composition, and also on the surrounding dielectric medium. Noginov et al. demonstrated lasing emission occurring in the wavelength around 530 nm with Au nano-particles of 14 nm diameter. These nano-particles were enclosed by dye doped silica shell. Resonant energy transfer between the localised surface plasmon and dye molecules contributed to the lasing emission[19, 20, 21]

## 1.2 Challenges in Plasmonic Nanolaser Design

In last decade, much work has been done in the field of plasmonic nanolaser. However, there are a number of aspects plasmonic nanolaser research that needs to be addressed. Firstly, most of demonstrations of plasmonic nanolaser mentioned in the preceding section involves optical pumping. There are relatively few number of reports of electrically pumped surface plasmon laser. For ubiquitous application in photonic integrated circuits and many other applications, optical pumping poses the engineering challenge to include another light source to pump the laser. Another fundamental issue with plasmonic laser is the associated Ohmic loss. Due to this

loss, Q factor of the plasmonic nanocavity cannot reach very high values. As a result, spectral coherence of the lasing emission suffers and material supporting high gains to compensate these losses is required. Another issue for such lasers is the divergence of emission. In many applications, spatial coherence from laser emission is essential. However, when plasmonic modes couple to free space radiation, it shows significant divergence. Minimizing divergence of emission is another active research topic for such lasers. Room temperature operation is another issue for nanolasers. The first few experimental demonstrations of plasmonic laser was conducted in cryogenic temperatures. In recent years, organic gain mediums have facilitated room temperature operations of such devices.

Despite the challenges, plasmonic laser shows great prospect as coherent source of light with nanoscale dimensions. Since the first demonstration, nanolaser research has made great strides in improvement of laser performance. In this thesis, we present our work as an incremental advancement towards tackling some of the challenges and bottlenecks of plasmonic nanolaser.

### 1.3 Overview of Thesis

In the following chapter, brief overview of plasmonics is provided. Firstly, Drude model of metal is formulated which is essential for understanding of the existence of plasmonic modes. It is followed by discussions on surface plasmon polariton modes and localized surface plasmon modes. These modes are essential for operation of plasmonic crystal based nanocavities employed in our proposed nanolaser design. We look into the dispersion and excitation methods of these plasmonic modes. We also discuss a number of applications and challenges of research in the field of plasmonics.

In chapter 3, discussions on numerical techniques utilized in this work are presented. The full field vectorial simulator used in this work is based on finite difference

time domain (FDTD) method. We discuss the numerical model used for modeling the laser gain medium. To verify the consistency of the numerical methods, we have simulated a simple photonic cavity laser. We also discuss few important considerations for passive and active device simulations.

In chapter 4, we present our design methods of designing the plasmonic laser. We discuss how plasmonic nanolaser cavity provides feedback and how it differs from conventional photonic cavities. We also discuss different types of nanocavities in recent reports. Design considerations for plasmonic nanocrystal based cavity is presented. We study how extraordinary transmission can be tuned by different design parameters. To achieve optimal nanocavity performance, we explore extraordinary transmission in conjunction with optical tamm states. These optical phenomena have been utilized in our proposed nanolaser design. We have included the results obtained from the numerical study of these phenomena with different types of structures. Guided by the findings presented in this section, we finally designed a plasmonic nanocavity demonstrating optimal performance.

In chapter 5, we present the performance of proposed nanolaser structure. In the proposed nanocavity, 1D photonic crystal is added on top of the metallic nanohole array. We present the results and findings of the active structure in response to optical pumping. We have systematically investigated the emission properties as different design parameters were varied. Finally, analysis on the improvements observed in the emission characteristics and far-field radiation for our proposed structure is presented.

In chapter 6, we present our conclusions of this work on efficient plasmonic nanolaser design. We also present scopes of future works and possible next steps to further improve the performance of the proposed nanolaser.

# Chapter 2

## Plasmonics

Free electron gas of metals exhibit macroscopic oscillation under proper excitation. The quantized oscillation of free electron plasma is called plasmon. Surface plasmon polariton and localized surface plasmon- both modes have proved pivotal in various photonic applications. Understanding both of these phenomena is essential for designing our proposed nanolaser device. In this section, we briefly discuss fundamentals of plasmonics both quantitatively and phenomenologically.

A neutral gas of heavy ions and light electrons is called a plasma. Metals and heavily doped semiconductors can be treated as plasmas because they contain equal numbers of fixed positive ions and free electrons. The free electrons experience no restoring forces when they interact with electromagnetic waves. This contrasts with bound electrons that have natural resonant frequencies in the visible or ultraviolet spectral range.

### 2.1 Dielectric Function of Metals

The optical properties of metals can be explained by a plasma model for a broad range of wavelengths. For alkali metals, this range extends up to the ultraviolet, while for

noble metals inter-band transitions occur at visible frequencies, limiting the validity of this approach. In this model, a number of interactions like lattice potential and electron-electron interactions are not taken into account. The significant contribution of such interaction in metal dynamics causes the deviation of metal response from that of plasma. In such cases, Drude model can provide much more accurate representation of metal. In this model, oscillation of a free electron is to be considered under the influence of an AC electric field of an EM field. The equation of motion for the displacement  $x$  of the electron is given by

$$m_0 \frac{d^2x}{dt^2} + m_0\gamma \frac{dx}{dt} = -eE(t) = -eE_0 \exp(-j\omega t). \quad (2.1)$$

Here,  $\omega$  is the frequency of light. The first term represents the acceleration of the electron, while the second is the frictional damping force of the medium. The term on the right hand side is the driving force exerted by the light. Solving this equation, we can get the displacement,  $x(t)$ . This displacement is related to polarization  $P$  of metal. Moreover, as we know from the definition of electric displacement,  $D = \epsilon_r \epsilon E = \epsilon_0 E + P$ . Here,  $\epsilon_r$  is the relative permittivity of metal. With mathematical manipulations, we can write permittivity in the following concise form:

$$\epsilon_r = 1 - \frac{\omega_p^2}{\omega^2 + j\gamma\omega}, \quad (2.2)$$

where,

$$\omega_p^2 = \frac{Ne^2}{\epsilon_0 m_0}. \quad (2.3)$$

For a lightly damped system,  $\epsilon_r$  can be assumed to be

$$\epsilon_r = 1 - \frac{\omega_p^2}{\omega^2}. \quad (2.4)$$

Drude model is essential for understanding the mechanism of surface plasmon polariton and localized surface plasmon modes. However, it is important to keep in mind that its accuracy is much better in the infrared regime compared to that in the visible range. The reason is that the Drude model only accounts for the contribution of the free electrons in the conduction band. When the frequency increases, multiple new absorption channel opens up, which results in significant deviation in response from Drude model. Nevertheless, Drude model is sufficient for discussion of dispersion of surface plasmon modes to be discussed in the next section.

## 2.2 Surface Plasmon Polariton

An interesting phenomenon occurs at metal-dielectric interfaces. An EM wave can be confined at the interface. Surface plasmon polaritons(SPP) are electromagnetic excitations propagating at the interface between a dielectric and a conductor, evanescently confined in the perpendicular direction. These electromagnetic surface waves arise via the coupling of the electromagnetic fields to oscillations of the conductor's electron plasma.

### 2.2.1 SPP at Single Metal/Dielectric Interface

Fig. 2.5 shows the propagation geometry with a Air/Metal interface. For simplicity we are assuming a one dimensional problem, i.e.,  $\varepsilon$  depends only on one spatial coordinate. Specifically, the waves propagate along the x-direction of a Cartesian coordinate system, and show no spatial variation in the perpendicular, in-plane y-direction; therefore,  $\varepsilon = \varepsilon(z)$ . In all generality, assuming harmonic time dependence,  $\mathbf{E}(\mathbf{r}, t) = \mathbf{E}(\mathbf{r}) \exp(-j\omega t)$  of the electric field, we can write Helmholtz equation given by

$$\nabla^2 \mathbf{E} + k_0^2 \varepsilon \mathbf{E} = 0. \quad (2.5)$$

Here,  $k_0 = \omega/c$  is the wave vector of propagating wave in vacuum.

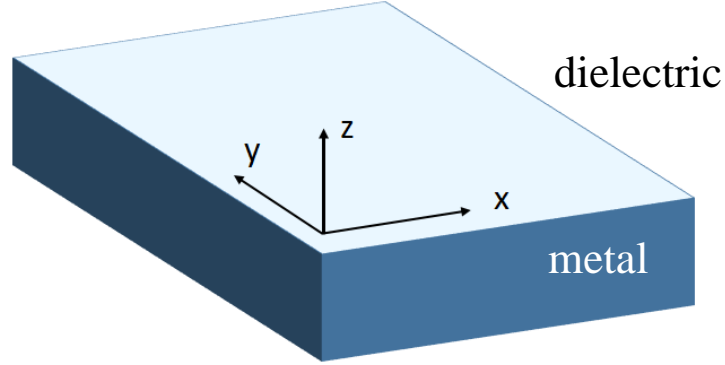


Figure 2.1: Propagation geometry at Air/Metal interface.

For electromagnetic wave propagating in x direction,  $\mathbf{E}(x, y, z) = \mathbf{E}(z) \exp(j\beta x)$ . Here, complex parameter  $\beta = k_x$  is called the propagation constant of the traveling wave and corresponds to the component of wave vector in the direction of propagation. Inserting this expression into Eq. (2.5) gives

$$\frac{\partial^2 \mathbf{E}}{\partial z^2} + (k_0^2 \varepsilon - \beta^2) \mathbf{E} = 0. \quad (2.6)$$

We can obtain a system of equations for each of the orthogonal directions. This system allows two sets of self-consistent solutions with different polarization properties of the propagating waves. For TM polarization at the interface between two materials with dielectric constants  $\varepsilon_1$  and  $\varepsilon_2$ , continuity conditions require that  $k_2/k_1 = -\varepsilon_2/\varepsilon_1$ . Therefore, confinement to the surface demands  $\text{Re}[\varepsilon_1] < 0$  if  $\varepsilon_2 > 0$  implying that the surface waves exist only at interfaces between materials with opposite signs of the real part of their dielectric permittivities, i.e. between a conductor and an insulator.

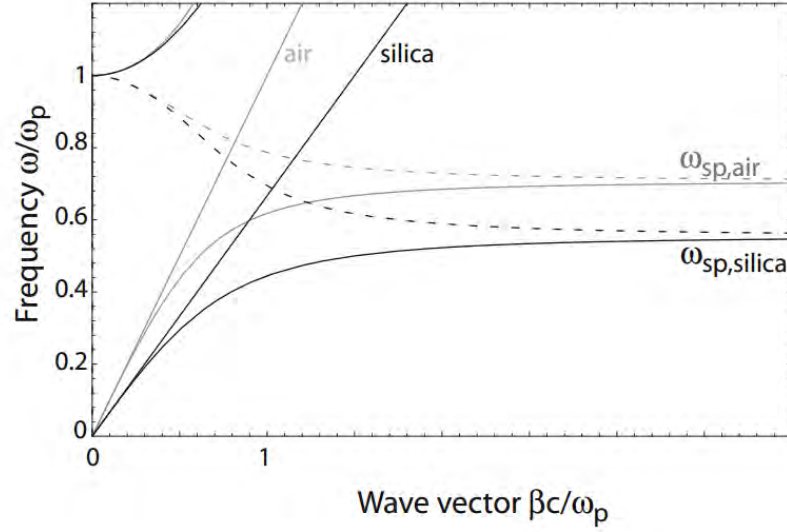


Figure 2.2: Dispersion relation of SPPs at the interface between a Drude metal with negligible collision frequency and air (gray curves) and silica (black curves) [22].

From continuity conditions, we can obtain the dispersion equation

$$\beta = k_0 \sqrt{\frac{\varepsilon_1 \varepsilon_2}{\varepsilon_1 + \varepsilon_2}}. \quad (2.7)$$

Now, Fig. 2.2 shows the dispersion relation of SPPs at the interface between a Drude metal with negligible collision frequency and air and silica. In the limit of negligible damping of the conduction electron oscillation ( $\text{Im}[\varepsilon_1(\omega)] = 0$ ), the wave vector  $\beta$  goes to infinity as the frequency approaches surface plasmon frequency,  $\omega_{\text{sp}}$ , and the group velocity  $v_g \rightarrow 0$ . The mode thus acquires electrostatic character, and is known as the surface plasmon.

For real metals, the damping is not negligible giving rise to finite wave vector  $\beta$  at plasma frequency. The dispersion plot for real metal considering the losses is shown in Fig. 2.4.



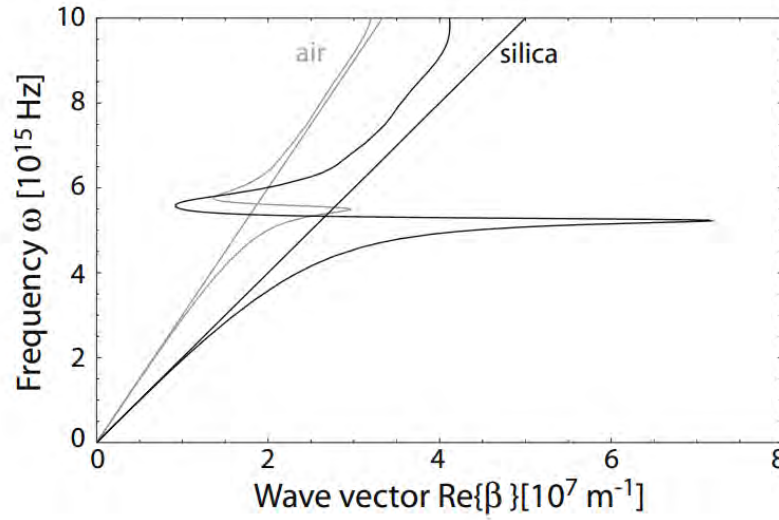


Figure 2.3: Dispersion relation of SPPs at a silver/air (gray curve) and silver/silica (black curve) interface. Due to the damping, the wave vector of the bound SPPs approaches a finite limit at the surface plasmon frequency [22].

Plasmonic confinement is achieved in metal dielectric interface as the propagation constant  $\beta$  is greater than the wave vector  $k$  in the dielectric, leading to evanescent decay on both sides of the interface. The SPP dispersion curve therefore lies to the right of the light line of the dielectric which is given by  $\omega = ck$ . As a result, excitation by three-dimensional light beams is not possible unless special techniques for phase-matching are employed. Methods of efficient excitation of surface plasmon mode is an active field of research. The typical methods of SPP excitation are prism coupling, grating coupling, near-field excitation, etc.

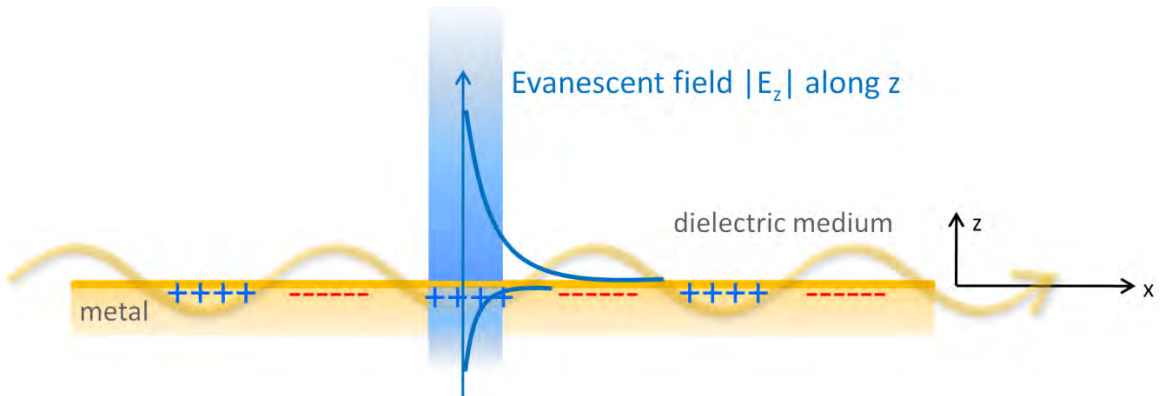


Figure 2.4: An evanescent wave propagating along the interface of a metal and a dielectric. Electric field component along z-axis decays exponentially [23].

## 2.3 Localized Surface Plasmon

In the operation of our proposed plasmonic nanolaser, localized surface plasmon plays a pivotal role. The oscillation of the surface charge density in metallic nano-particles, commonly named localized surface plasmons (LSPs), is a result of the collective oscillation of the conduction electrons under the constraints imposed by the physical boundaries of the nano-particle geometry. The optical properties of metallic nano-particles are determined by the excitation of electromagnetic surface modes. Localized plasmon modes are stationary oscillations of the surface charge density at optical frequencies along the metal boundaries of a metallic particle. The ability to control its resonance makes LSP modes suitable in a number of applications such as photovoltaics, biosensing, spectroscopy, molecular fluorescence, etc [24, 25, 26].

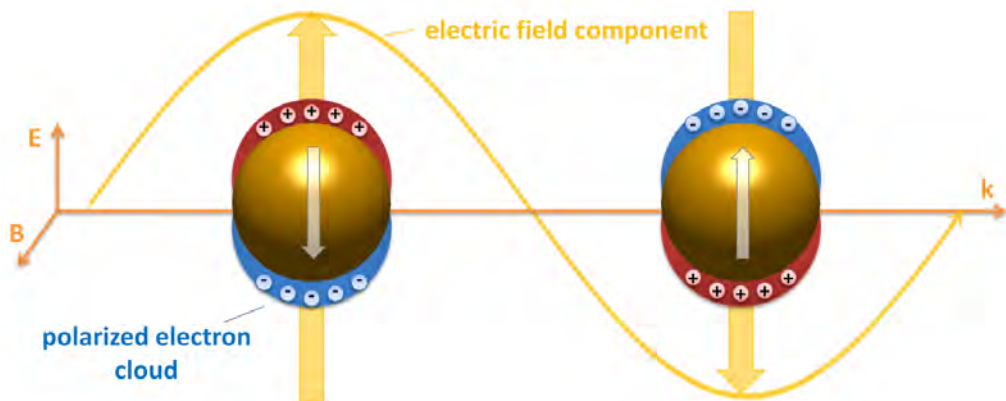


Figure 2.5: Mechanism of localised surface plasmon resonance [23].

### 2.3.1 Excitation of LSP

If an electromagnetic wave impinges on a metallic (whose spatial dimension is assumed to be much smaller than the wavelength of light), the electron gas gets polarized (polarization charges at the surface) and the arising restoring force again forms a plasmonic oscillation. The metallic particle thus acts like an oscillator and the corresponding resonance behavior determines the optical properties.

Localized surface plasmon mode differs from surface plasmon polariton mode in a number of ways. Light cannot couple directly to plasmon excitations of a flat, semi-infinite metal surface since energy and momentum cannot be conserved simultaneously. Whereas, localized modes in metal nano-particles can be coupled by free space radiation of light. For surface plasmon polariton modes, the resonant wavelength is mainly dependent on the material properties. For localized surface plasmon modes, resonance strongly depends on shape of the particles.

### 2.3.2 Dependence on Dielectric Medium and Particle Shape

Coupling of LSP modes can be described through the particle polarizability,  $\alpha$  that relates the incoming electric field,  $E$  with the electric dipole moment  $p = \alpha E$ . Generally, the polarizability of a metallic object is a frequency-dependent magnitude that depends on the dielectric function of the metal and on the surrounding medium, as well as on the particle geometry. A localized surface plasmon resonance is associated with a pole of the polarizability of the metal nano-particle as a function of frequency (wavelength). To see how localized resonances affect the response of metal nano-particles, we need to look at absorption and scattering crosssections for that particle. For spherical particles with radius  $a$ , the scattering crosssection,  $C_{\text{scat}}$  is related to polarizability,  $\alpha_{\text{sph}}$  by the following equation

$$C_{\text{scat}} = \frac{8\pi}{3} k^4 a^6 \left| \frac{\varepsilon_{\text{sph}} - \varepsilon_{\text{med}}}{\varepsilon_{\text{sph}} + \varepsilon_{\text{med}}} \right|^2 = \frac{k^4}{\pi} |\alpha_{\text{sph}}|^2. \quad (2.8)$$

The dipolar polarizability of a spherical particle with radius  $a$  is given by

$$\alpha_{\text{sph}} = 4\pi\varepsilon_0 a^3 \frac{\varepsilon_{\text{sph}} - \varepsilon_{\text{med}}}{\varepsilon_{\text{sph}} + 2\varepsilon_{\text{med}}}. \quad (2.9)$$

Here,  $\varepsilon_{\text{sph}}$  is the dielectric function of the sphere and  $\varepsilon_{\text{med}}$  is the dielectric function of the surrounding medium. If the dielectric value of sphere is constant and with negligible imaginary part of the dielectric function, the scattering cross-section shows a rather flat spectral response and almost zero absorption. When the sphere is made of a metal characterized by a plasma frequency, which was discussed in previous section, the metal particle shows resonant behavior. From Eq. 2.9, we can see that polarizability depends on the dielectric constant of metal and its dielectric environment.

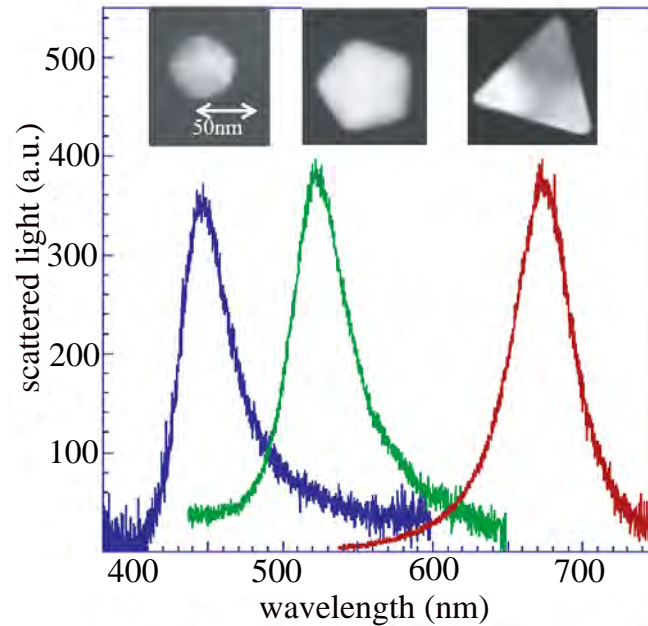


Figure 2.6: Scattering spectra of Ag nano-particles of different shapes [27].

An exciting aspect of LSP is that its resonance changes with particle shape. This enables engineering the response of particles for applications in different purposes. The modification of the particle shape modifies the spectral position of the plasmonic resonance, thus providing a tool to tune the optical response at the nanoscale. Several effects, strongly dependent on the particle shape, play a role in determining the actual LSP resonance frequency and the field enhancement. The shape dependence of localized resonance of silver nano-particle is shown in Fig. 2.6. For nanorod structure, elongation results in strong anisotropy in optical response. Due to change of aspect ratio, the scattering response of the particle shows drastically different response for longitudinal and transverse polarization. Similarly, curvature of nano-particles also affect the resonant frequency. As curvature of the particle is reduced, strong localization of surface charge results in high field intensity.

## 2.4 Prospect of plasmonics

Surface plasmon polariton and localized surface polariton modes can give rise to a number of unique optical phenomena. Extraordinary transmission through sub-wavelength hole arrays is attributed to coupling of surface plasmon polariton modes [28]. Localized surface plasmon is responsible for shape dependence transmission through nanoapertures [29]. In recent years, we have seen great many number of SPP and LSP based devices. SPP modes have been extensively studied for applications in sub-wavelength guiding of light [30, 31, 32, 33]. It has also been studied for application in photovoltaics, as it can couple light along the structure, which in turn leads to increased optical absorption [34, 35, 36, 37]. There also have been reports of highly sensitive biosensors based on SPP resonances [38, 39]. SPP has also been studied for directional radiation and optical cloaking applications. Apart from such passive devices, researchers have worked on incorporating active components into plasmonic devices. Various devices have been proposed to modulate transmitted field or phase, or detect output radiation [40, 41]. The challenges in most of these applications are the short-range propagation of SPP modes. To solve this issue, plasmonic waveguides and devices with gain materials have been studied [7]. Extensive study and growth of the field of plasmonics have lead to exploration of nanoscale active coherent source for light sources.

The tunability of localized surface plasmon resonance has made this resonance highly applicable for biosensing and other spectroscopic applications [42, 43]. Apart from sensing, LSP has also been used in photovoltaics. Nanoparticles suspended in active layer of solar cell can lead to field enhancement in the vicinity of the particles leading to enhanced efficiency [44, 45]. Another emerging application of LSP is its interaction with gain medium. When coupled with gain medium, the metallic loss associated with plasmonic resonance can be significantly reduced [46]. Moreover, there

are theoretical studies suggesting the increase of localized resonances in presence of gain medium [9]. This increased resonance and reduced losses can be useful in number of applications. The promising results from this reports have lead to studying localized surface plasmon lasing in dipolar gain medium [19].

## 2.5 Summary

In this chapter, we have looked into the fundamentals of plasmonic resonance. Surface plasmon polariton and localized surface plasmon resonances are essential for extraordinary transmission phenomenon used in our proposed nanolaser design. In this chapter, we have briefly discussed the origins of these modes and how they can be efficiently excited. We have also discussed the fundamental challenges and prospects of plasmonics in future applications. However, these future applications are dependent on the successful development of experimental methods and techniques for the reliable fabrication of optimally designed structures.

# Chapter 3

## Numerical Simulation

### Methodology

Several commercial numerical tools/software are available for time domain and frequency domain analysis which can be used to analyze a plasmonic/photonic structure. However, every such tool comes with certain limitations in regard to custom geometry or simulation conditions. Moreover, material characterization, definition of different parameters are some of the key aspects of customized simulation. Among a number of commercial softwares, we chose Lumerical FDTD Solutions based on finite difference time domain (FDTD) algorithm. Compared to frequency domain method, FDTD methods provide a number of advantages. In this chapter, a brief introduction to the FDTD algorithm is presented. It is followed by discussions on a few important simulation parameters and preferences in the Lumerical FDTD solver. Then, we present the model used to simulate the gain medium used in the proposed laser system. This chapter is concluded by numerical simulation results of a simple photonic cavity laser. The results of this simulation are used to verify the integrity of the simulation setup and laser material model.



### 3.1 Finite Difference Time Domain Model

The FDTD simulator is based on the simultaneous time dependent solution of Maxwell's third and fourth equations which are given by

$$\frac{\partial D}{\partial t} = \nabla \times H, \quad (3.1a)$$

$$D(\omega) = \varepsilon_0 \varepsilon_r^*(\omega) E(\omega), \quad (3.1b)$$

$$\frac{\partial H}{\partial t} = -\frac{1}{\mu_0} \nabla \times E. \quad (3.1c)$$

The time-dependent Maxwell's equations are discretized using central-difference approximations to the space and time partial derivatives. These finite-difference equations are then solved in a leapfrog manner. In other words, the electric field vector components in a volume of space are solved at a given instant in time and then the magnetic field vector components in the same spatial volume are solved at the next instant in time. This process is repeated over and over again. Depending on the type of source used in the simulation domain, this leapfrogging time steps are run a finite number of time.

This method of solving Maxwell's equation was first proposed by Yee, in a seminal paper published in 1966 [47]. Solutions of set of finite difference equations for time and space dependent equations for loss-less materials was proposed in that paper. The commercial electromagnetic simulator used in our work is also based on Yee's algorithm. A spatially staggered vector components of the E-field and H-field about rectangular unit cells of a Cartesian computational grid was proposed in this algorithm. It was arranged in a way so that each E-field vector component is located midway between a pair of H-field vector components. This grid was later referred to as Yee grid. Figure 3.1 shows arrangement of Yee grid for three dimensional simulation region. Apart from proposing spatially staggered field vectors, Yee also proposed

a leapfrog scheme for stepping in time such that electric field and magnetic field are temporally staggered. As a result, electric field updates are computed halfway of each time-step between consecutive H-field updates and vice versa.

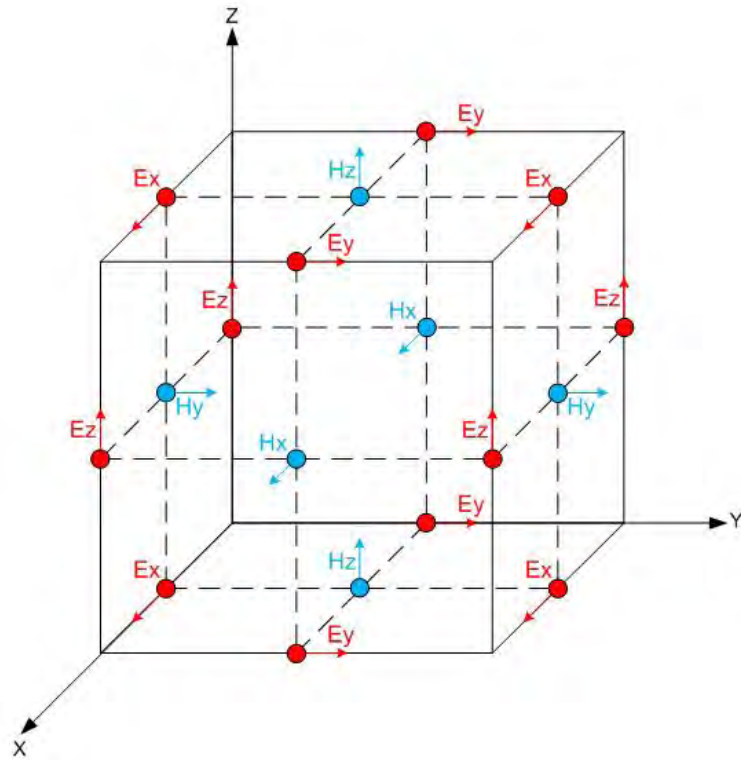


Figure 3.1: Yee grid in three dimensional simulation domain.

## 3.2 Boundary Conditions

### 3.2.1 Perfectly Matched Layer

Reflection from simulation boundaries is one of the major sources of error in FDTD simulators. At least one or more boundaries of typical electromagnetic simulation needs to be infinitely extended. To make the simulation domain wide enough to let the scattered wave decay is not a computationally efficient approach. As a result,

absorbing boundaries are incorporated into the simulation space. Various types of absorbing boundary conditions may be employed in order to resolve this problem [48, 49]. One of the most effective among all ABCs is the perfectly matched layer developed by Berenger [50]. The basic idea of the PML technique is to add an additional lossy layer around the simulation region with intrinsic impedance matched with the media at the outermost simulation region which ensures zero reflection from the interfaces and the field is attenuated while propagating through the media. It is ensured that the field intensity attenuates to zero before it hits the simulation boundary. In a continuous space, the PML absorber and the host medium are perfectly matched. However, FDTD simulation, the electric and magnetic material parameters are discretized and are spatially staggered. This results in discretization errors that can affect ideal behavior of the PML. In Lumerical FDTD Solutions, there are a number of topologies for PML to choose from. Each of the topologies has its own advantages and drawbacks. In our laser simulation, we have mostly studied with normally incident light. In those simulations, we have employed Uniaxial PML model [51]. In few of the cases where obliquely incident light was used, we have implemented stretched coordinate PML formulation [52].

### 3.2.2 Periodic and Bloch Boundary Condition

In our study, we have mainly studied three dimensional plasmonic crystal structure consisting of periodic elements. In FDTD simulations, total response of a periodic structure can be extracted from simulation results of just one unit cell. To achieve that, periodic boundary condition is applied along the axis of symmetry. Periodic boundary condition can be applied in one or more boundaries of the simulation.

Bloch boundary condition is similar to periodic boundary condition. The application of this boundary condition is necessary when the structure is periodic but the EM field has phase shift between each period. Such case arises when incident light is

obliquely incident.

Lumerical FDTD supports both of these boundary conditions. In our simulations, we have mostly used Bloch boundary conditions due to its robustness. When Bloch boundary condition is used, the simulator uses complex values of electric and magnetic field. Few normalizations were needed to be applied in simulations where continuous wave normalizations were disabled.

This commercial simulator also supports symmetric and anti-symmetric boundary conditions. These boundaries are applicable when there is one or more planes of symmetry in the simulation domain. Since our proposed designs has multiples planes of symmetry, we had used symmetric and anti-symmetric boundary conditions to reduce the simulation time drastically.

### 3.2.3 Determining Spatial and Temporal Cell Size

Choosing correct values of spatial cell size is an important aspect of electromagnetic simulation with FDTD method. Numerical dispersion can occur from discrete spatial sampling of FDTD mesh. Not only that, if meshing is coarse, it can result in slight anisotropy of speed of light on direction of propagation. Determining the cell size is much like sampling a signal. Like any sampling process higher sampling rate results in more accurate representation of the real quantity. Though the minimum number of points per wavelength depends on various factors involving the simulation medium, at least ten points per wavelength restricts simulation errors to acceptable limit. To ensure this, ten points per wavelength in the material with the largest refractive index in the simulation medium is required to be used. Therefore,

$$\Delta x \leq \frac{\lambda_0}{n_{\max} \times 10}. \quad (3.2)$$

Here,  $\lambda_0$  is the free space wavelength and  $n_{\max}$  is the largest refractive index contained in the simulation medium. Once the spatial cell size is chosen, the temporal step size requires to be so set. For this case, Courant condition [48, 49] must be satisfied which is given by

$$\Delta t \leq \frac{\Delta x}{\sqrt{n} \times c_0}. \quad (3.3)$$

As discussed, as the value of spatial mesh size is defined by the material index, FDTD algorithm allows the use of graded meshes. Such a non-uniform mesh can make FDTD calculations more accurate, while requiring less memory and less computation time than uniform mesh. Non-uniform meshing allows relatively larger mesh sizes in medium with lower refractive index, while using small meshes in high refractive index material.

Apart from non-uniform meshing, Lumerical FDTD provides a number of conformal meshing methods. Conformal meshing a number of mesh refinement options which can give sub-cell accuracy from a simulation. That means, we can get accurate representation of device response using much higher mesh sizes. This is achieved by using an integral solutions of Maxwell's equations near interface [53]. In our linear and active material simulations, we have used non-uniform grids with conformal meshing applied to all materials.

### 3.3 Dispersive Material Modeling

One of the main advantages of finite difference time domain method is its ability to produce broadband response of a device in a single simulation. However, as different materials exhibit variation of material index with wavelength, this dispersion has to be incorporated into the material system in FDTD algorithm. FDTD simulators typically employ Drude, Debye, or Lorentz materials. But, these models are highly

simplified representation of real materials. As a result, relying on these models for a wide band simulation would result in significant deviation from the actual response. One of the ways to solve this problem is to use multi-pole model, which is a dispersion model that results from combining two or more distinct Lorentz models. This model has some limitations when it comes to modeling real materials impacted by impurities, defects, and other more complicated material issues. In some electromagnetic simulators, materials are modeled with a polynomial fitting. While this method can provide accurate representation of the model, it is prone to cumbersome calculation and high computational cost depending on the order of the polynomial.

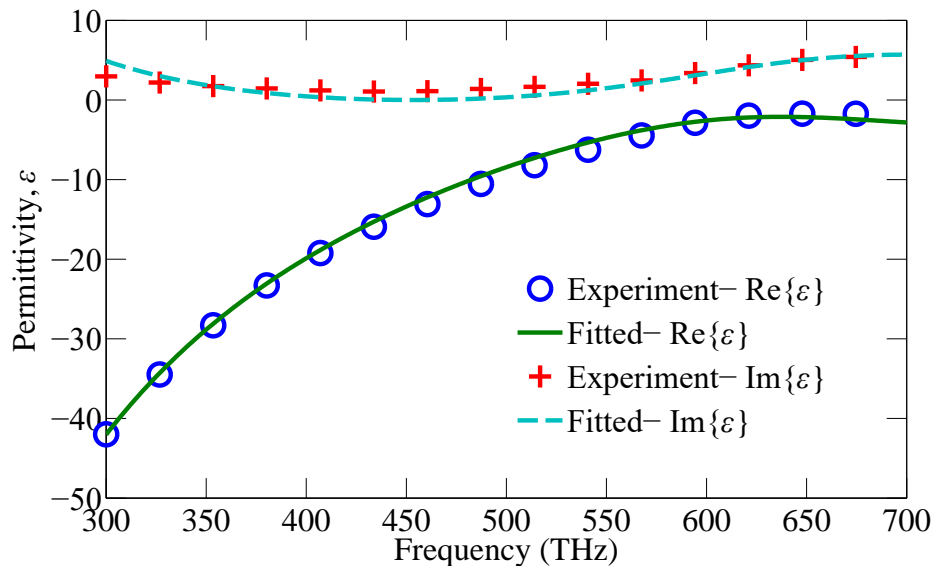


Figure 3.2: Fitting of Au permittivities with multi-coefficient material model.

To solve this broadband simulation challenge, Lumerical uses multi-coefficient materials (MCMs). MCMs rely on a more extensive set of basis functions to better fit dispersion profiles that are not easily described by Drude, Debye, and Lorentz materials. It also provides designers with the ability to automatically and optimally choose the type and number of terms required to accurately describe their materials. The type of fit that can be automatically generated to imported material data as

well, which enables us to model any material as long as the material indices are available. In our simulations of passive and active devices in this work, we have used this multicoefficient materials to model Au. The dielectric materials used in our simulation was assumed non-dispersive over the frequency of interest. Figure 3.2 shows the experimental data and MCM fit of real and imaginary part of permittivity of Au. Experimental data for Au was obtained from Ref. [54].

### 3.4 Gain Medium Modeling

In this work on plasmonic nanolaser, the laser gain medium was modeled using four level two electron system. This model utilizes simplified quantized electron energies which provide four energy levels for each of the two electrons. This model also takes into account the effect of Pauli's exclusion principle. The population levels of the gain mediums are governed by the coupled rate equations. To simulate the response of gain medium, these rate equations and Maxwell's equations are self-consistently solved through the FDTD algorithm. In this section, firstly, we will discuss this modeling methodology. Then we will verify the consistency of this material model by simulating the laser dynamics of a photonic cavity laser and compare it to the results reported in Ref. [55]. We will also discuss the post-processing tools developed for plasmonic nanolaser simulation.

#### 3.4.1 Four Level Two Electron System

To model the gain medium in numerical simulation, a semi-quantum framework was utilized. In this framework, the gain medium (dye molecules) was modeled as four level quantum system, whereas the electromagnetic field was modeled classically. Fig. 3.3 shows the four level system used in this formulation. Pumping electromagnetic pulse induces absorption from ground level  $|0\rangle$  to highest level  $|3\rangle$  from which

a fast non-radiative emission increases the population in the higher lasing level  $|2\rangle$ . Radiative transition between level  $|2\rangle$  and level  $|1\rangle$  leads to lasing emission if there is population inversion between this two levels. Finally, another non-radiative transition induces emission from level  $|1\rangle$  to level  $|0\rangle$ .

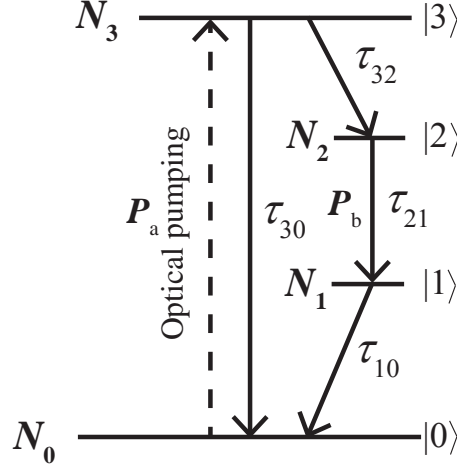


Figure 3.3: 4 level 2 electron system

These transitions in this 4 level system are treated as two coupled dipole oscillators. Level 1 and level 2 corresponds to dipole  $P_a$ , whereas, level 3 and level 0 corresponds to dipole  $P_b$ . Polarization densities  $P_a$  and  $P_b$  are found to be driven by the product of electric field  $E$  and population difference between two corresponding levels, i.e.,

$$\frac{\partial^2 P_a}{\partial t^2} + \gamma_a \frac{dP_a}{dt} + \omega_a^2 P_a = \xi_a (N_2 - N_1) E, \quad (3.4a)$$

$$\frac{\partial^2 P_b}{\partial t^2} + \gamma_b \frac{dP_b}{dt} + \omega_b^2 P_b = \xi_b (N_3 - N_0) E. \quad (3.4b)$$

Here,  $\xi_{a,b} = 6\pi\epsilon_0 c^3 / (\omega_{21,30}^2 \tau_{21,30})$ ,  $\gamma_{a,b}$  = damping coefficients,  $\omega_{a,b}$  = resonant frequencies. In this formulation, Pauli's exclusion principle (PEP) is enforced. Due to PEP, presence of electron in one energy level reduces the rate/efficiency of pumping or relaxation from other levels. Therefore, the rate of transition is function of both



the source and destination population level. Using this principle, the rate equations for the 4 level system becomes,

$$\frac{dN_3}{dt} = -\frac{N_3(1-N_2)}{\tau_{32}} - \frac{N_3(1-N_0)}{\tau_{30}} + \frac{1}{\hbar\omega_b} E \cdot \frac{dP_b}{dt}, \quad (3.5a)$$

$$\frac{dN_2}{dt} = \frac{N_3(1-N_2)}{\tau_{32}} - \frac{N_2(1-N_1)}{\tau_{21}} + \frac{1}{\hbar\omega_a} E \cdot \frac{dP_a}{dt}, \quad (3.5b)$$

$$\frac{dN_1}{dt} = \frac{N_2(1-N_1)}{\tau_{21}} - \frac{N_1(1-N_0)}{\tau_{10}} - \frac{1}{\hbar\omega_a} E \cdot \frac{dP_a}{dt}, \quad (3.5c)$$

$$\frac{dN_0}{dt} = \frac{N_3(1-N_0)}{\tau_{30}} + \frac{N_1(1-N_0)}{\tau_{10}} - \frac{1}{\hbar\omega_b} E \cdot \frac{dP_b}{dt}. \quad (3.5d)$$

In Eq. 3.5,  $N_i$  is the population density probability in level  $i$ , and  $\tau_{ij}$  is decay time constant between levels  $i$  and  $j$ . These four rate equations are coupled to Maxwell's law through polarization densities,  $P_a$  and  $P_b$  by the following equation,

$$\frac{dE}{dt} = \frac{1}{\varepsilon} \nabla \times H - \frac{1}{\varepsilon} N_{density} \left( \frac{dP_a}{dt} + \frac{dP_b}{dt} \right). \quad (3.6)$$

Therefore, the four rate equations along with this Ampere's law provide a self-consistent set of equations describing the interactions between gain molecules and electromagnetic fields associated with nano-particles. Using this model, we can simulate different gain mediums if parameters related to emission and absorption characteristics are known. In this work, the gain medium we have used is an organic gain medium, IR-140. The parameters used for this model are as follows:

- **Absorption transition:**  $\lambda_a = 800$  nm,  $\Delta\lambda_a = 100$  nm,
- **Emission Transition:**  $\lambda_b = 870$  nm,  $\Delta\lambda_b = 100$  nm,
- **Emission Transition:**  $\lambda_b = 870$  nm,  $\Delta\lambda_b = 100$  nm,
- **Lifetimes:**  $\tau_{21} = \tau_{30} = 1$  ns,  $\tau_{32} = \tau_{10} = 10$  fs,

- **Concentration of dye molecules:**  $C = 2 \times 10^{18} \text{ cm}^{-3}$ .

### 3.5 Simulation of a Photonic Cavity Laser

To verify the material model for gain medium and simulation setup, a simple photonic cavity laser was simulated. Figure 3.4 shows the schematic of this optically pumped laser. Optical feedback of this laser is implemented by a single-defect distributed Bragg reflector (DBR) cavity.

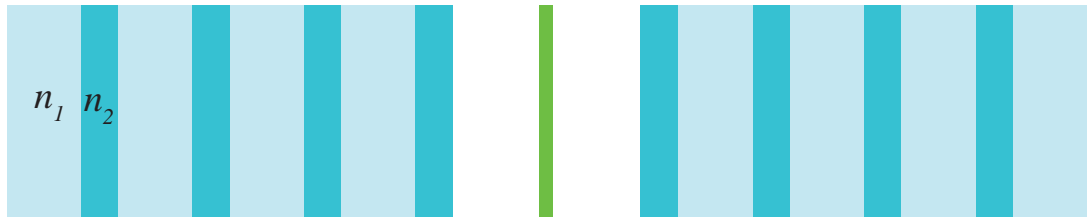


Figure 3.4: Schematic of a simple photonic cavity laser. A gain medium is placed between two DBRs.

The DBR cavity consists of two Bragg reflectors and each of them consists of three layer of refractive indices alternating between 1.0 and 2.0 with thicknesses 375 nm and 187.5 nm. The length of the gap between these two DBR is 750 nm. A gain medium of 50 nm is placed at the center of this gap. The layers are designed so that the defect mode occurs at 1500 nm and its passband is at 750 nm. The quality factor of the cavity is found to be 100. In this device, the gain medium is pumped with a light of 750 nm wavelength and lasing emission is expected to be observed at 1500 nm. That is why the stopband was designed to be around 1500 nm which confines the lasing emission within the cavity. For the gain medium of this structure, we chose  $\tau_{32} = \tau_{10} = 100 \text{ fs}$  and  $\tau_{21} = \tau_{30} = 300 \text{ ps}$ . The initial population density was chosen to be  $5 \times 10^{23} / m^3$ . Finally we pump the structure with continuous wave input of 750

nm. We modify the input 750 nm electromagnetic CW signal so that it increases gradually from a small value to its steady state amplitude. The amplitude envelop of this pumping signal with  $1 \times 10^6$  V/m amplitude signal is shown in Fig. 3.5. This modification was necessary to reduce the numerical noise caused by sudden onset of high amplitude CW pulse.

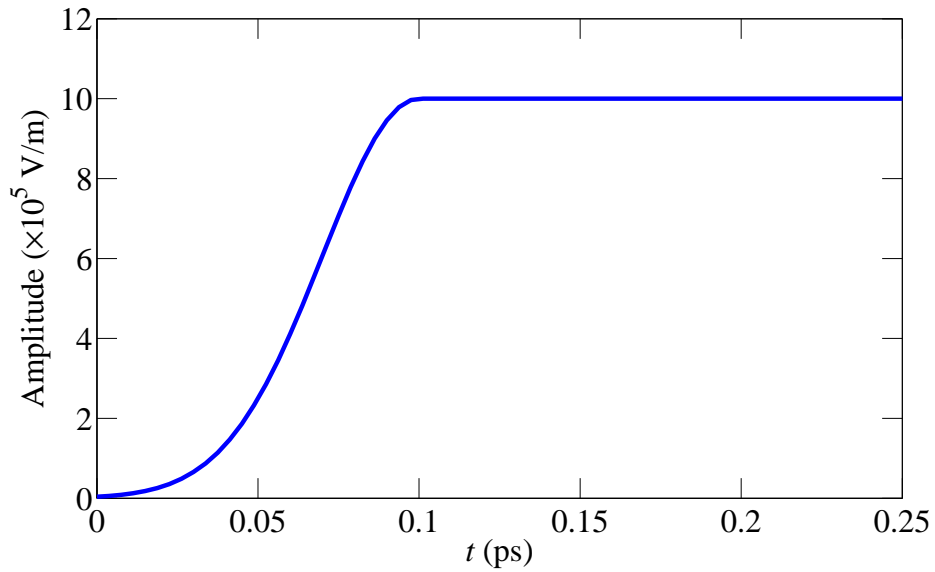


Figure 3.5: Amplitude envelop of the electromagnetic wave used to optically pump the photonic cavity laser.

Considering the lifetimes of different levels of the gain medium, the FDTD simulation was terminated after simulating for 30 ps. Throughout this time, time evolution of electron populations of all four levels were recorded. We present the variation of these populations as a function of time in Fig. 3.6.

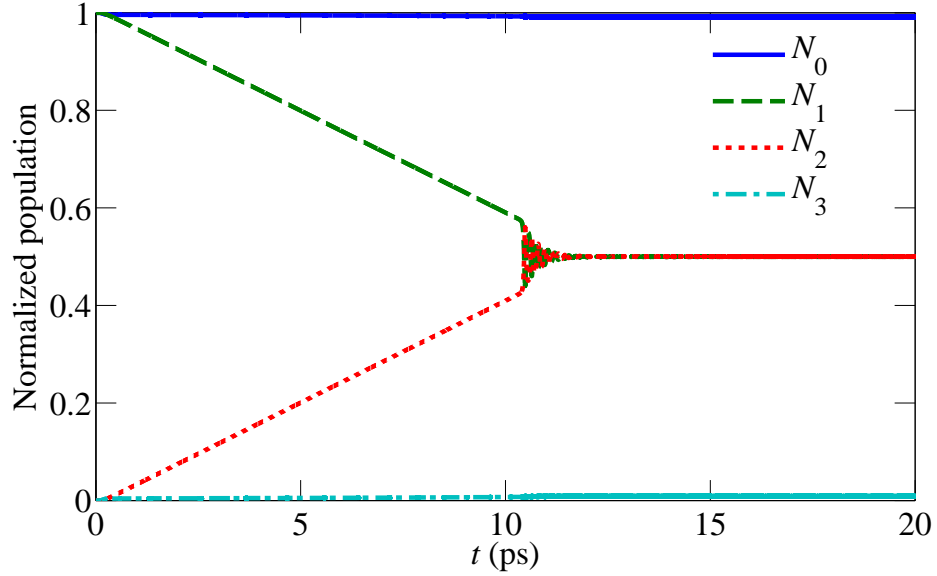


Figure 3.6: Time evolution of normalized populations in the four levels of the laser gain medium.

From this figure, we note that, in the initial state, only level 0 and level 1 is occupied and other two levels are empty. As pumping signal is introduced, the population density of level 1 starts to decrease and level 2 starts to increase drastically. We also note, that populations of level 0 and level 3 shows small variation with time. This is due to the fact that pumping energy causes electrons from level 1 to move to level 0. Then the electrons from level 0 is also pumped to level 3 from where it transitions to level 2. Due to the relatively slower transition from level 2 to level 1, the population of level 2 keeps on increasing until it becomes greater than that of level 1, i.e., until population inversion occurs. It is precisely at that moment, we expect to observe onset of lasing emission.

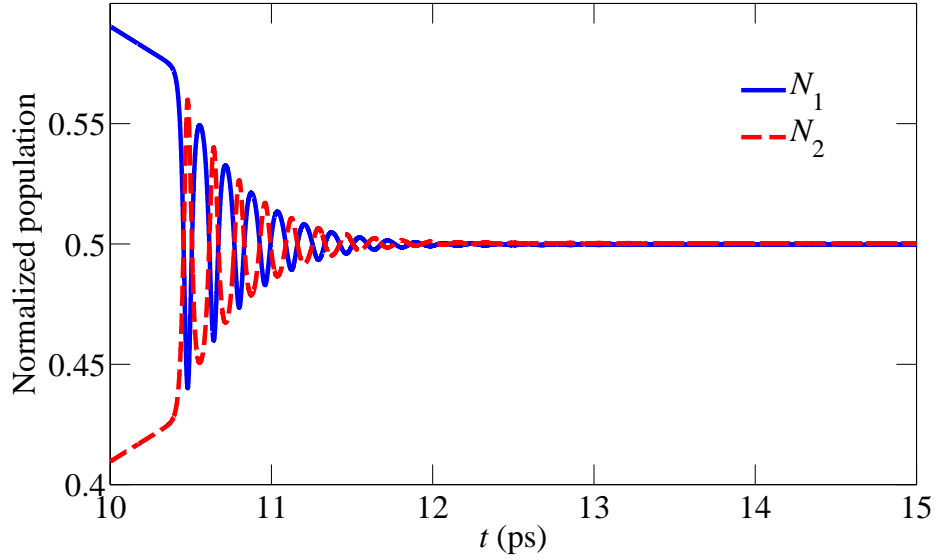


Figure 3.7: Time evolution of normalized populations in two lasing levels of the laser gain medium.

To analyze the dynamics of the lasing population levels in greater detail, we plot the population levels of just the two lasing levels in Fig. 3.7. This figure shows population probability of the lasing levels 10 ps after the pumping signal was introduced. We can see that at approximately 10.5 ps, population inversion occurs. It shows fluctuations of the population levels until 12 ps and then reaches steady state value. We note that in steady state condition, population inversion is maintained which is sufficient to sustain continuous lasing emission.

We also capture the electromagnetic field at the output end of the laser using a time monitor throughout the simulation duration. This time-domain data consists both the lasing signal and the transmitted pumping signal.

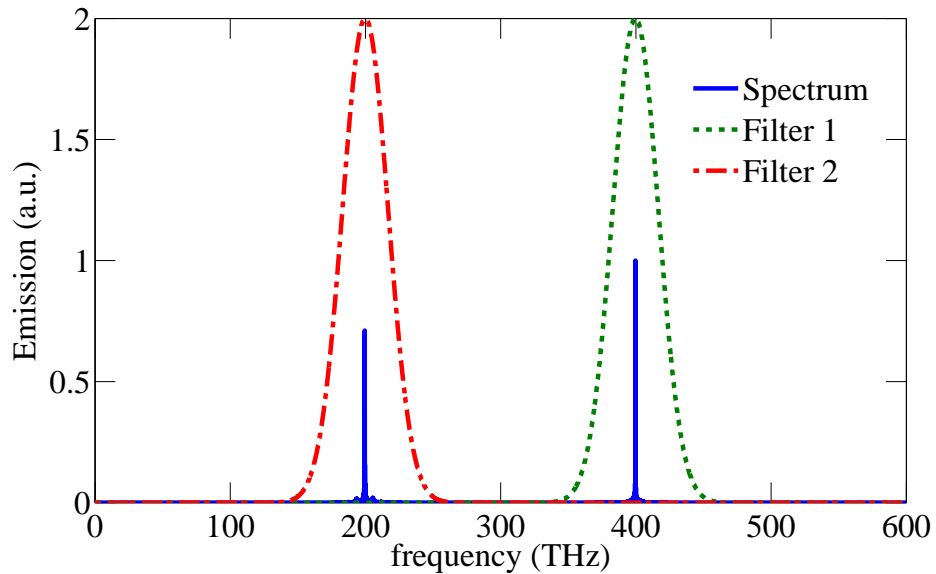


Figure 3.8: Emission spectra along with the frequency domain filters to extract pump and lasing emission.

To extract the lasing and pumping signal from this data, we resort to frequency domain filtering. Firstly, we put the time domain data through fast Fourier transform which decomposes the signals into their frequency components. Then, we apply two Gaussian filters centered at the pumping and lasing frequency. Figure 3.8 shows frequency response of the captured time domain data along with two Gaussian filters. The peaks at 200 THz and 400 THz correspond to lasing and pumping wavelength respectively. Once the spectra is filtered, the resultant frequency responses are put through inverse fast Fourier transform, which translates the pumping and lasing signal to time domain signal. Figure 3.9 shows the magnitude of the electric field of lasing and pumping signal as a function of time.

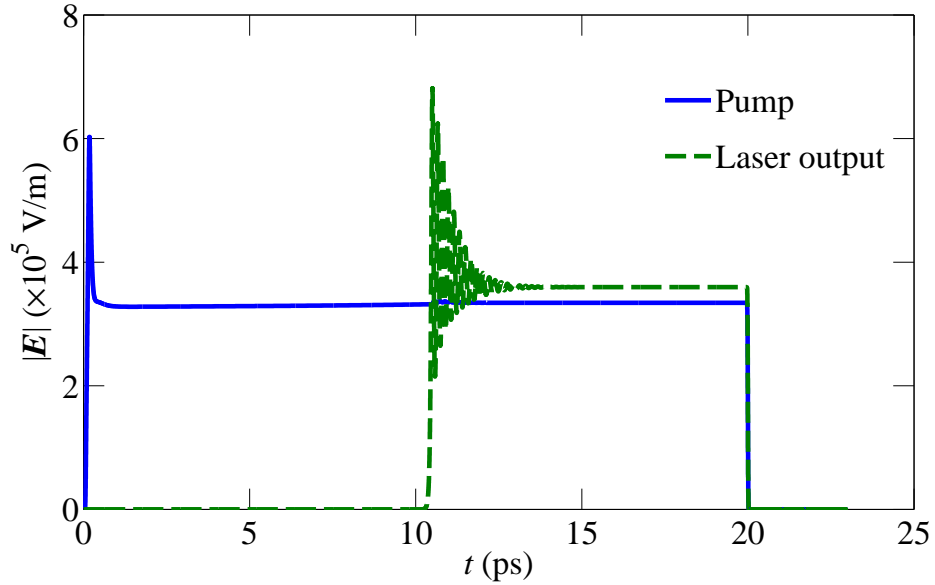


Figure 3.9: Extracted pump signal and lasing signal on the output side of the photonic cavity laser.

The onset of lasing at approximately 10.5 ps is observed from this figure. This correlates with the occurrence of population inversion discussed in the preceding section. Much like the oscillations of population inversion, the laser output shows fluctuations in magnitude that eventually stabilizes to a steady state value.

To observe threshold behavior of this simple photonic cavity laser, we have calculated emission intensities of laser at different pumping intensity. The output intensity vs pump intensity plot is shown in Fig. 3.10. At pumping intensity of 5.5 (a.u.), clear threshold behavior is observed. We also note that emission saturates when pumping intensity is increased beyond a certain level. The results obtained from the simulations are in good agreement of the published results in Ref. [55].

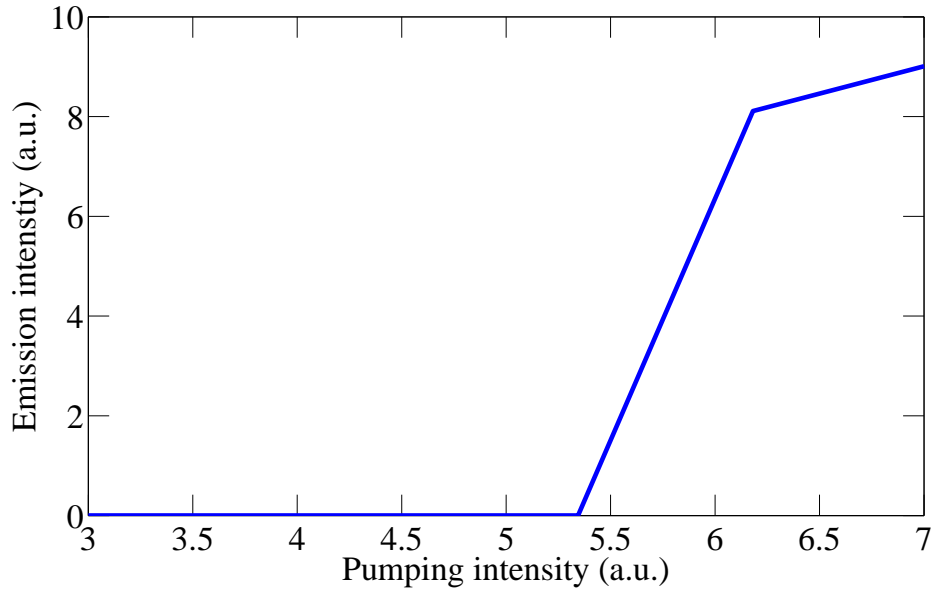


Figure 3.10: Emission intensity of the photonic cavity laser as pumping intensity is increased.

As it has already been mentioned, this simple 1 dimensional photonic cavity laser is pumped using continuous wave source. However, for plasmonic lasers, pulsed pumping is used in most of the reported cases [6, 8]. Moreover, in 2 dimensional and 3 dimensional simulations, simulations with continuous wave source would result in huge computational overhead. In those cases, using pulsed sources can prove to be a numerically efficient approach. To this end, we have modified the simulation setups to make it compatible to pulse pump signals. Necessary post-processing modules were created to calculate laser emission spectra and far-field pattern in both 2 dimensional and 3 dimensional simulation domain.

## 3.6 Summary

In finite difference time domain method, the constituent equations are solved simultaneously to give the time evolution of the different field components in a defined



medium. It allows to calculate broadband response of a system from a single system by using fourier transform of the system response to a broadband input. Among various commercial simulation tools, we have used Lumerical FDTD Solutions for our work. We have discussed our choice of boundary conditions and meshing methodologies for different simulations using this simulation tool. This electromagnetic solver facilitates the modeling of dispersion of passive materials using multi-coefficient models. For laser simulation, a 4 level 2 electron system was used for gain medium. This model was incorporated into the time-stepping algorithm of FDTD. We have also presented our results of simulation of a simple photonic crystal cavity. These results were used to verify the consistency of material model and simulation setup. We have also discussed briefly about a number of post-processing tools developed for simulating two and three dimensional plasmonic nanolasers.

# Chapter 4

## Design of Plasmonic Nanolaser

In the last decade, field of nanophotonics has seen remarkable progress in a number of applications. Nanoscale manipulation of light has lead to drastic miniaturization of many optical devices such as, bio-sensors, solar cells, photodetectors, waveguiding, etc. In various photonic applications, a coherent source of electromagnetic energy with nanoscale footprint is often required. Conventional lasers employing macroscopic photonic cavities are diffraction limited with a fundamental lower limit of device dimension. Downscaling of these devices leads to increased losses which render them useless in most applications. Plasmonic modes- surface plasmon polariton and localized surface plasmon- can confine electromagnetic energy beyond the diffraction limit, which make them a promising choice for implementing lasers with nanoscale dimensions.

Laser has two principle constituents: gain medium and resonantor. The gain medium achieves population inversion through electrical or optical pumping and is capable of supplying energy to the lasing modes. Whereas the resonator is an optical cavity necessary to produce feedback for lasing action. A cavity stores electromagnetic energy inside the laser structure. Strength of the resonance is dependent on the feedback supported by the cavity. In other words, stronger the resonance, a photon

is stored inside the cavity for a longer duration of time, which leads to higher energy buildup within the gain medium resulting in stronger emission. In conventional lasers, cavity feedback is obtained by designing the resonator such that standing wave can form inside the cavity. However, to form a standing wave, at least one dimension of the cavity must be longer than the diffraction limit of light. In photonic cavities, diffraction limit of light is given by  $\lambda/2n_m$ , where  $n_m$  is the effective mode index and  $\lambda$  is free-space wavelength of light. Using Nanoplasmonic techniques, we can design nanocavities with dimensions beyond the diffraction-limit. In this chapter, we thoroughly discuss our design methods and performance analysis of proposed plasmonic nanolaser.

## 4.1 Plasmonic Nanocavity Design

The first step of designing plasmonic nanolaser is to design the nanocavity. In most of the conventional photonic lasers, the standing wave of light occurring between two sides of the resonator provides feedback mechanism. However, in plasmonic nanocavity, feedback can be established by surface plasmon resonances excited at metal-dielectric interface, or from localized or collective resonances of metallic nanostructures- nano-particles or nanoapertures in dielectric environment. At plasmonic resonances, high field enhancement at the vicinity of metallic nanostructures can facilitate resonant energy transfer between the gain medium and the plasmonic mode and thereby produce laser emission.

A fundamental bottleneck for the realization of SPP nano-optical functional devices stems from large intrinsic metal loss induced by resistive heating. Hence, any type of plasmonic resonator based on a plasmonic waveguiding principle is inevitably limited by the intrinsic metal loss in addition to other sources of losses, such as, scattering due to inhomogeneity of metal layer, radiation into free space and the substrate.

To minimize the effect of Ohmic losses on plasmonic resonance strength, a number of structures have been proposed. Hybrid plasmonic-photonic modes excited between metal and dielectric layer separated by a dielectric spacer layer has been reported to produce low loss propagation of surface plasmon [56]. Additionally, long-range surface plasmon mode coupled at metal-dielectric interface has also been explored for nanolaser application [57]. However, in such structures, low-loss plasmonic mode was achieved at the expense of reduced modal confinement.

In nanolasers based on surface plasmon polariton mode excitation, divergent far-field radiation is another issue. This is due to the fact that, surface plasmon dispersion lies below the light line. As a result, plasmonic modes have very high wavevectors compared to free-space wavevectors. Therefore, when plasmonic mode is coupled to radiative mode from the gratings, or from edges of plasmonic cavities, this phase mismatch leads to diverging radiation. To counter this issue, a number of nanocavity structures employing plasmonic crystals have been explored [10, 11, 12]. In such devices, resonances of periodically arranged metallic nanostructures lead spatially coherent emission. Nanolasers based plasmonic crystals have been reported to produce room-temperature lasing. Narrow-beam emission with very low divergence, along with room temperature operation makes such nanolaser structures a promising candidate for wide-scale applications. However, such nanocavities have a number of limitations that affect the emission efficiency and laser performance significantly. In this thesis, we present our work on designing nanolaser structure based on periodic arrangement of nanostructures. Moreover, we study the underlying physics of these structures and propose novel nanoresonator designs to overcome their limitations to drastically improve the performance and efficiency. In addition to that, our proposed nanocavity design allows to tune the peak stimulated emission wavelength over a substantial range.

## 4.2 Plasmonic Crystal Based Nanocavity

Recently reported plasmonic crystal based nanolaser structures consist of either periodic array metallic nano-particles suspended in gain medium or periodic metallic hole array covered by gain medium. Periodic arrangement of nano-particles can excite band-edge lattice plasmon polariton mode which can produce lasing emission. Different types of nano-particle- cylindrical, bowtie, nanodome- array has been reported to produce plasmonic lasing in near-IR region [10, 11, 12]. Similar plasmonic crystal structure, but with periodic circular nanohole array in Ag layer has been reported to produce visible wavelength lasing [15].

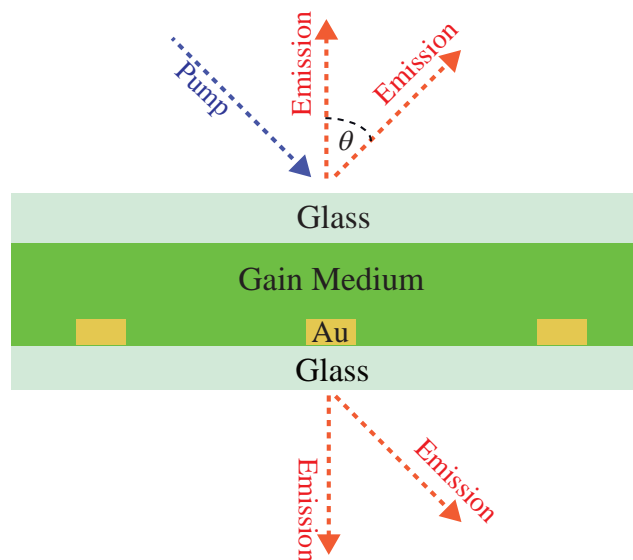


Figure 4.1: Schematic of a simplified lattice plasmon based nanolaser structure.

Periodic circular nanohole arrays can couple surface plasmon polariton- bloch (SPP-bloch) mode and exhibit resonant transmission at certain wavelengths. This phenomenon is termed as extraordinary transmission (EOT) [28]. In most of the reported lattice plasmon and extraordinary transmission based laser, pump beam is incident obliquely, and lasing emission was observed normal to the surface. However,

part of the emission was also coupled into off-normal diffracted radiation. In addition to that, lasing emission was observed in both the transmission and reflection side. So, the emitted energy is distributed in a number of modes at a number of angles in both sides of the nanolaser devices. As a result, emission efficiency is affected significantly. To illustrate these phenomena, in Fig. 4.2, we show the far-field response and emission spectra of a simplified lattice plasmon based structure [16]. The schematic of the structure is shown in Fig. 4.1. This device is optically pumped by pump pulse centered at 800 nm wavelength and lasing emission is observed at 870 nm. Pump beam is incident at  $45^\circ$  to surface normal. Far-field emission spectra of this device at reflection side is shown in Figure 4.2(a). We note multiple number of diffracted modes: one approximately along surface normal, another along  $50^\circ$ . Figure 4.2(b) shows the emission spectra calculated from monitors placed in reflection and transmission side. As previously discussed, we observe that emission of comparable intensity at both sides.

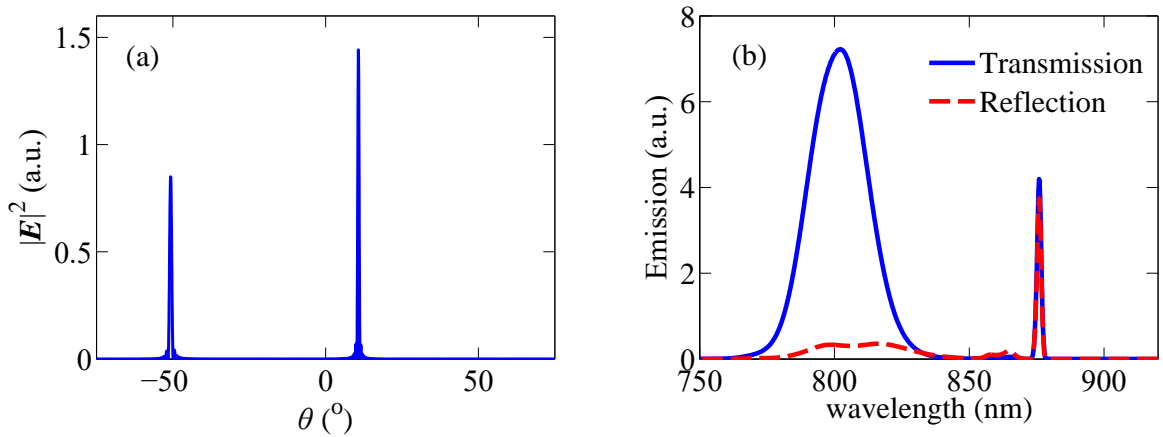


Figure 4.2: (a) Far-field pattern observed in reflection side. (b) Emission spectra recorded in transmission and reflection side.

Confining lasing emission to a single diffracted mode and to one side of the nanolaser structure can lead to tremendous improvement in laser performance and

superior efficiency. Our primary objective of this work is to achieve such emission characteristics with low beam divergence and spectral tunability in near-IR range. Considering the potential of plasmonic crystal based nanoresonator, firstly we concentrate on periodic array of sub-wavelength holes exhibiting extraordinary transmission. In the next section, we study the mechanisms and dynamics of enhanced and resonant transmission to design our nanocavity suitable for operation in near-IR region.

### 4.2.1 Extraordinary Transmission

Discovery of extraordinary transmission is one of the important milestones in the research of sub-wavelength optics. Extraordinary transmission (EOT) is defined as the appearance of series of peaks and dips in the transmission spectra which is observed in single sub-wavelength hole or periodic arrangement of sub-wavelength holes in metal. At resonant extraordinary transmission wavelengths, a periodic array of sub-wavelength holes transmits more light than a large macroscopic hole with the same area. Before the discovery of EOT, sub-wavelength apertures were thought to be poor transmitter of electromagnetic energy. This low transmission was explained using Bethe's theory of light transmission through circular hole perforated in thin metallic film [58]. Transmission normalized to the area according to this theory is

$$T \approx \frac{64}{27\pi^2} \frac{r^4}{\lambda^4}, \quad (4.1)$$

where,  $\lambda$  is wavelength of incoming light and  $r$  is the radius of the hole. A great number of applications of this phenomena ranging from spectroscopy, lasers, photovoltaics, biosensing, etc [59, 60]. Moreover, extensive numerical, analytical and experimental studies have been done [29, 61, 62]. In the following sections, we will study the the characteristics of this optical phenomenon to design optimal nanocavity

structure for our nanolaser.

## 4.2.2 Mechanisms of EOT

### Hole resonance and hole shape

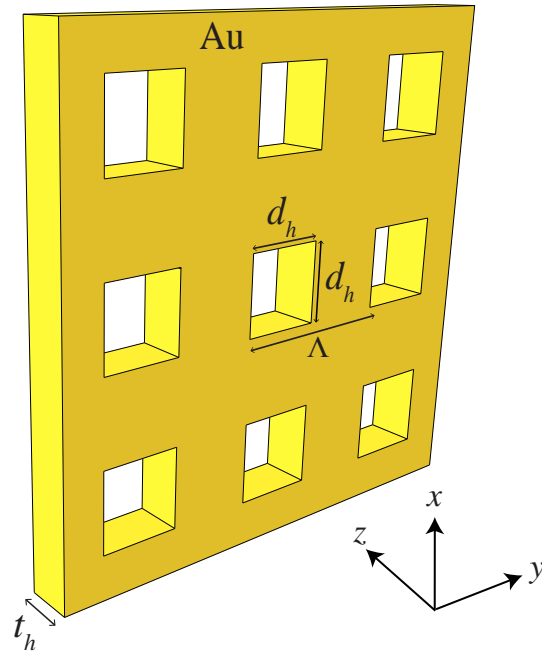


Figure 4.3: Au nanohole array with square holes demonstrating extraordinary transmission.

A typical transmission spectra for EOT is characterized by a series of maxima and minima. These peaks and dips exceed the value predicted by conventional aperture theory. Manifestation of extraordinary transmission was first observed by Ebbesen et al. in sub-wavelength hole array on 200 nm thick gold and silver films [28]. Since then, a number of studies with different hole size, lattice size, thickness, and symmetry have been reported [63, 64, 65]. It was observed that spectral peak position of sub-wavelength array shows almost linear dependence on the lattice period. At first, this



dependence was attributed to occurrence of Wood-Raleyigh anomaly. However, it was discovered that, those transmission minimas coincide with the optical frequencies for which the wavevector is equal to surface plasmon polariton. That means at those wavelengths, the periodic corrugations on metallic structures leads to momentum matching condition between in-plane wavevector of the incident photon and surface plasmon polariton and causes increased absorption. This condition can be given mathematically by

$$\vec{k}_{\text{SP}} = \vec{k}_x \pm i\vec{G}_x \pm j\vec{G}_y. \quad (4.2)$$

Here,  $\vec{k}_{\text{SP}}$  is the surface plasmon wavevector,  $\vec{k}_x$  is the incident light wavevector parallel to metal surface,  $(i, j)$  is the grating order for reciprocal lattice vector  $\vec{G}_x$  and  $\vec{G}_y$  of the square lattice. From the dispersion relation of surface plasmon polariton wave, we know

$$|\vec{k}_{\text{SP}}| = \frac{\omega}{c} \sqrt{\frac{\epsilon_d \epsilon_m}{\epsilon_d + \epsilon_m}}, \quad (4.3)$$

where,  $\omega$  is the frequency of incident light and  $\epsilon_m/\epsilon_d$  is the dielectric constant of metal/dielectric.

However, it was later argued that coupling of surface plasmon mode cannot completely explain the extraordinary transmission phenomenon [64]. Changing the shapes of the holes while keeping the reciprocal lattice vectors unchanged results in significant changes in emission spectra and transmission intensity [66]. This result suggested significant contribution of individual hole resonances to extraordinary transmission. Following this finding, a number of experimental results were published exploring the influence of hole dimensions, metal thickness, and other structural parameters on resonance peaks, linewidth, transmission intensity and far-field emission [65]. In this work, we have conducted numerical study of sub-wavelength hole array with a view to engineer resonant emission of such structure for our laser design.

To study the spectral response of sub-wavelength hole array, we begin with a

Au metallic film perforated with square holes with square lattice. Fig. 4.3 shows the schematic of metallic nanohole array device. It is to be noted that, we mostly confine our study to nanohole array to structures with sub-wavelength periods. For such lattice periods, EOT is dominated by individual hole resonances. The reason for choosing such dimensions is to design a cavity that couples energy into a single diffracted mode to the output side. While choosing larger periods can result in increased emission via collective resonance of nanoholes, it can lead to multiple order of diffracted beam in output, which will affect the efficiency of laser.

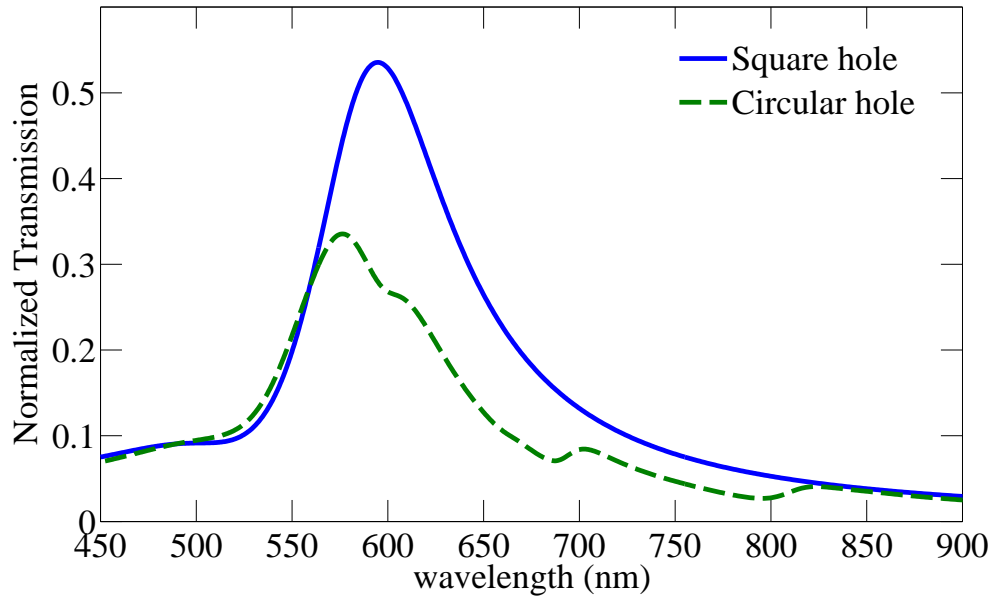


Figure 4.4: EOT spectra for square and circular holes.

At first, we study emission dependence of nanohole structures for different hole shapes. The first reported EOT structure used circular hole array. After that, different studies have discussed the resonant behavior for square, rectangular, elliptical holes. These structures have been reported to exhibit polarization effects and shape resonances. Apart from these, few complex designs using triangular, trapezoidal structures also have been studied [29]. In this study, we mostly concentrated on the circular

holes and square holes with square lattice array. Figure 4.4 shows the transmission spectra for nanohole array with square and circular holes. In both devices, the lattice period,  $\Lambda$  is 350 nm and metal thickness,  $t_h$  is 100 nm. Transmissible area of the apertures in both devices is same. We note EOT resonance at longer wavelength in case of square hole compared to circular holes. This result can be understood by considering these sub-wavelength holes as waveguide cavity. For perfect electric conductor, circular hole cavity has lower cut-off wavelength when compared to square hole waveguide with same transmissible area. As a result, square hole array produces resonant peaks at larger wavelength compared to the structure with circular holes.

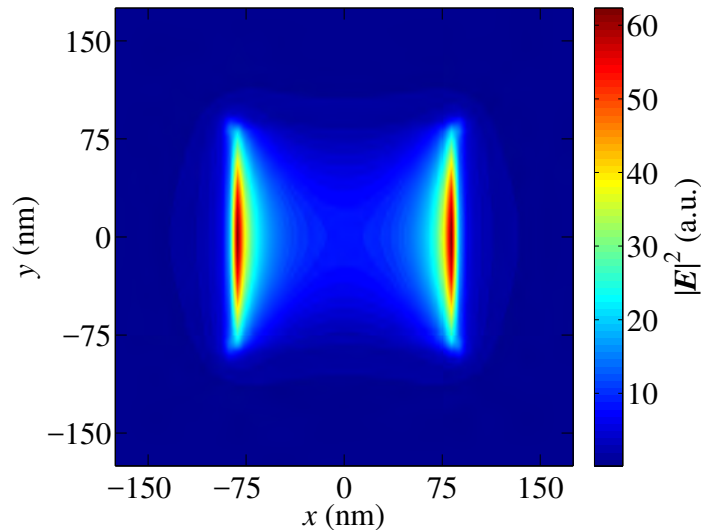


Figure 4.5: Electric field intensity at surface of the nanohole at resonant wavelength of extraordinary transmission.

We also observe higher normalized transmission through square holes for the same transmissible area as the circular holes. The resonant transmission for square holes occur at wavelength of 594 nm. Figure 4.5 shows the electric field intensity on Au-Air interface on top of the nanohole at this resonant wavelength. The width and breadth of the square nanohole is 170 nm. From this figure, we note that electric field is highly confined to the edges of the nanoaperture. The field profile suggests the occurrence

of localized surface resonance of individual hole.

### Hole size and thickness of metal

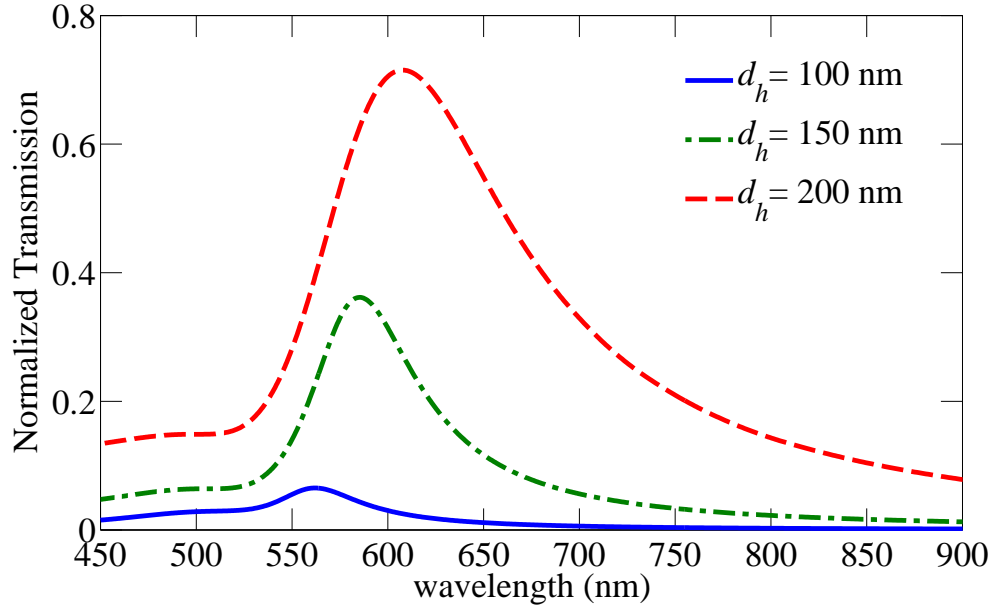


Figure 4.6: Transmission spectra of nanohole array for different square hole dimensions. The sub-wavelength array consists of square holes with period of 350 nm on 100 nm thick Au layer.

Size of sub-wavelength holes has significant influence on the transmission spectra of periodic nanohole array. An increase in square hole dimension leads to much greater increase in transmission than expected from conventional aperture theory. Molen et. al. have studied size dependent transmission in Ref. [66, 63]. They argued that, as re-radiation of surface plasmon polariton wave scales with fourth power of hole width, using time reversal argument, excitation of plasmonic mode also scale with fourth power. Since, the holes mediate SPP coupling between two sides of nanohole array, extraordinary transmission intensity should scale with the eighth power of hole dimension. It was also observed that the spectral peak position depends very weakly with variation of hole dimension. In Fig. 4.6 transmission spectra for different width

and breadth of square holes. The transmission intensity reduces drastically as hole dimension is reduced. Transmission peaks also shows small blue-shifting behavior.

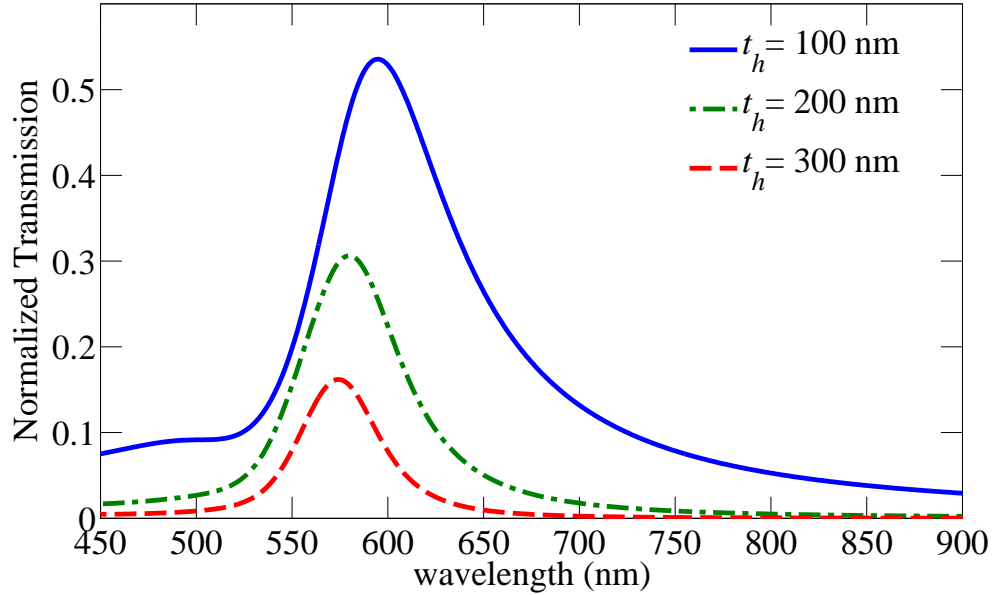


Figure 4.7: Transmission spectra of nanohole array for different metal thicknesses. The sub-wavelength array consists of  $170 \text{ nm} \times 170 \text{ nm}$  square holes with period of  $350 \text{ nm}$ .

Thickness of the metallic film also influences the transmission properties of the nanohole structure. The effect of thickness can be analyzed in two different thickness regime. For optically thick films, i.e. for metallic film with thickness at least 3 times the skin depth the transmission intensity decreases with increasing thickness. This is due to the fact that, the electromagnetic fields of two sides of the nanohole array are coupled by exponentially decaying field within the nanohole [65]. As film becomes thicker, the field between the two sides of the nanohole becomes increasingly decoupled, which leads to decreased emission. However, for metallic film becomes thinner ( $\leq 3 \times$  skin depth), surface plasmon mode excited on two sides of the metallic structure can interfere. This interaction leads to splitting of the plasmonic mode into two modes, namely short range plasmon mode and long-range plasmon mode. The

splitting of mode leads to some additional peaks in the transmission spectra. We have numerically simulated the transmission spectra of a nanohole array structure for different metal film thickness. The results are shown in Fig. 4.7. As predicted by the theory, emission intensity drops as metal thickness is increased.

In the preceding section, we have systematically studied the effect of different design parameters on nanohole transmission spectra. Based on the understanding developed in this study, we have chosen the appropriate hole shape, hole dimension, metal thickness and other parameters to design our plasmonic cavity. The schematic of the designed EOT-based nanocavity structure is shown in Fig. 4.8.

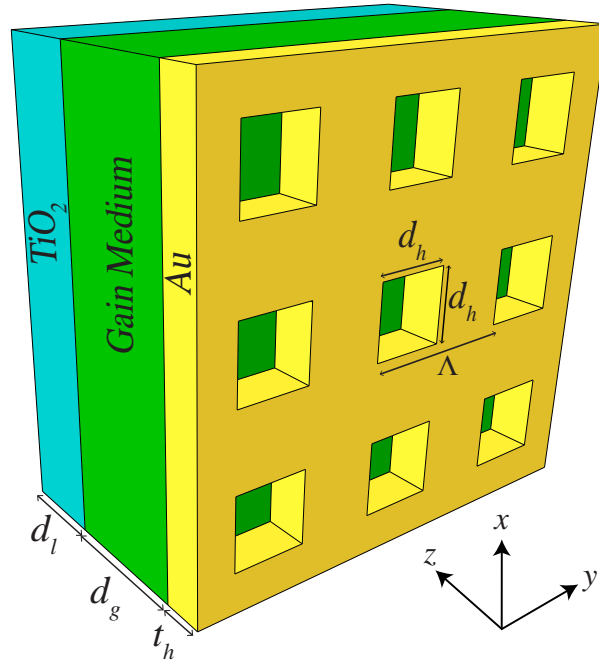


Figure 4.8: Schematic of EOT-based nanocavity.

In this design, we have chosen square metallic periodic nanoholes with square lattice symmetry. The metallic film is covered by PU mixed with IR-140 dye molecule. This layer with thickness of 325 nm provides the gain of this laser device. On top of this layer, we have  $\text{TiO}_2$  superstrate having the thickness of  $d_l = 434$  nm. We

have pumped this device with normally incident 40 fs pulse centered at 800 nm. The emission spectra obtained for a pump pulse with  $1 \times 10^8$  V/m amplitude is shown in Fig. 4.9. In this figure, the emission spectra on both the transmission side and reflection side is shown. While in the transmission side, lasing emission around 885 nm wavelength is observed, broad emission intensity around 800 nm wavelength is also noted. This emission around 800 nm denotes the scattered pump beam. Moreover, in the reflection side, the lasing emission around 885 nm is higher than the emission observed in the transmission side. Similarly, high intensity spectra around pumping wavelength is also observed in the reflection side.

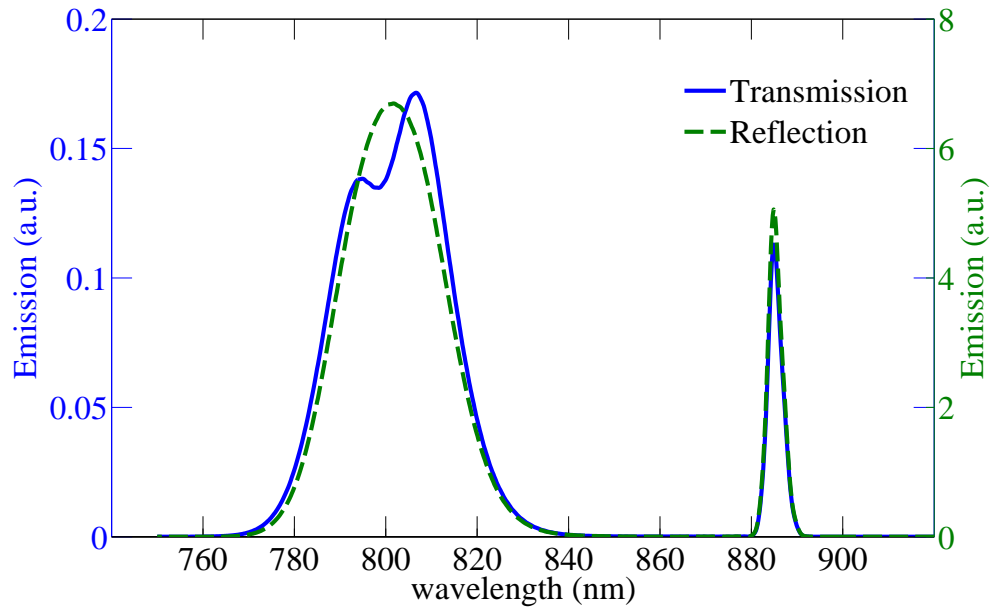


Figure 4.9: Emission spectra at reflection and transmission side for the structure shown in Fig. 4.8.

This design ensures single diffracted emission through the periodic nanohole array, but there are a number of limitations and drawbacks of this design. While this nanolaser design can achieve lasing through individual localized resonance, the lasing emission in the transmission is not sufficiently strong. Apart from that, significant

energy of stimulated emission is also observed in the side from which the device was pumped. In order to achieve efficient nanolaser, we need to guide most of the energy towards the transmission side. To achieve that we need to explore ways to further improve emission through such structures. In addition to that, we need to suppress the scattering of pump spectra in the transmission side. Hence, we investigate potential approaches to incorporate such emission properties into plasmonic crystal based nanocavity structure.

### 4.3 Improving Nanocavity Response

Since the discovery of extraordinary transmission, different attempts have been made to improve the transmission through single sub-wavelength aperture and periodic apertures. Nanocavity antenna, plasmonic bragg gratings, and bull's eye apertures have been used successfully to improve emission through single nanoaperture [67, 68, 69]. For periodic nanohole array, bridged nanoholes have produced enhanced emission suitable for biosensing application [70]. Recently, enhanced transmission of single nanohole with photonic crystal microcavity has been observed [71]. This enhancement was later attributed to excitation of optical Tamm state at metal-PhC interface [72].

The nanocavity we discussed in the preceding section exploits shape resonances of nanoholes to achieve transmission through sub-wavelength array. Incorporating 1D photonic crystal on top of our nanohole structure can potentially lead to emission enhancement via coupling of optical Tamm states. In addition, the PhC structure can also be designed to suppress the forward-scattering of pump beam through the structure. In the following section, we explore optical Tamm state resonance with a view to improving nanocavity performance.



### 4.3.1 Optical Tamm State

Tamm state is a type of surface state which was first observed in solid-state physics at the edge of truncated periodic atomic potential [73]. Much like the solid-state analog, optical Tamm state (OTS) is one type of a surface mode. Unlike surface plasmon polariton mode, optical Tamm state can be excited by normal incidence of light with zero inplane wavevector component. This is because, its dispersion line lies below the light line. It can also be coupled via light of both transverse electric and transverse magnetic polarization. In recent years, OTS has been investigated for applications in biosensing, optical filters, optical diodes, and photovoltaics [74, 75, 76].

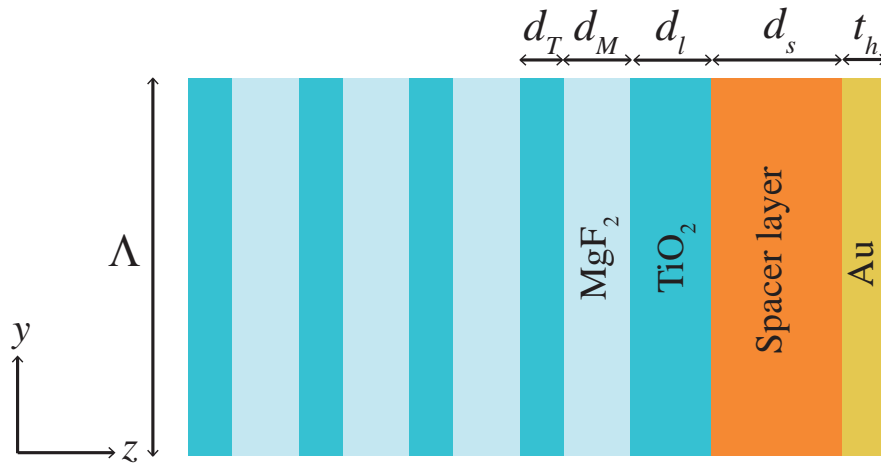


Figure 4.10: Schematic of the structure demonstrating optical Tamm resonance.

Optical Tamm state is observed at the interface between two photonic crystals and also at the interface between a photonic crystal and a metal layer [75, 77]. In our study, we concentrate mostly on the optical Tamm resonance occurring at the photonic crystal-metal interface. At resonance, high field intensity near the metal layer is observed. In this section, we will study the resonance properties of the structure shown in Fig. 4.10. This structure includes a 1 dimensional photonic crystal

structure consisting of alternating layers of  $\text{TiO}_2$  and  $\text{MgF}_2$ . This photonic crystal is deposited on a dielectric spacer layer ( $n=1.51$ ) which is followed by an 100 nm thick Au layer. The thickness of  $\text{TiO}_2$  and  $\text{MgF}_2$  are 108 nm and 165 nm respectively. However, the thickness of the last  $\text{TiO}_2$  layer connecting the PhC to spacer layer,  $d_l$  is 200 nm. The thickness of the spacer layer,  $d_s$  is 325 nm.

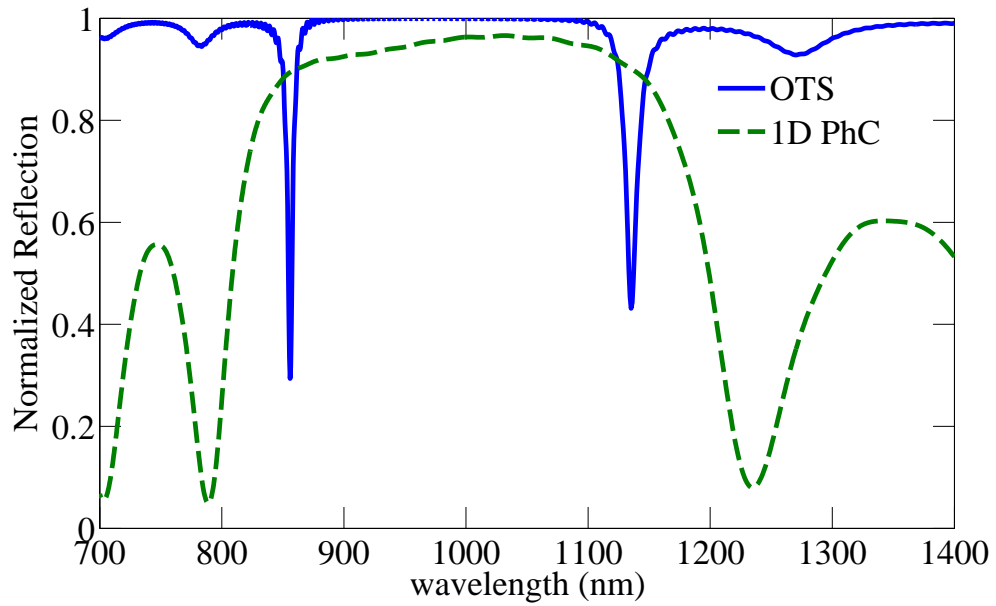


Figure 4.11: Normalized reflection spectra of the OTS structure and 1D photonic crystal.

The reflectivity of this structure can be analytically calculated using transfer-matrix method [78, 79]. We present the numerical calculation of reflection spectra of this structure upon normal incidence of light and compare it that of a bare photonic crystal structure (without the spacer and metal layer) in Fig. 4.11. Both structures consist of five pairs of  $\text{TiO}_2$  and  $\text{MgF}_2$  layers. From this plot, we note two dips in the reflectivity for the OTS structure at wavelengths 870 nm and 1140 nm. At these wavelengths optical Tamm resonance is observed. We also note that, these resonances occur in the stopband regime of the bare PhC structure. Essentially, terminating the

1D PhC by a metallic layer has created reflection minima in the stopband of the PhC structure.

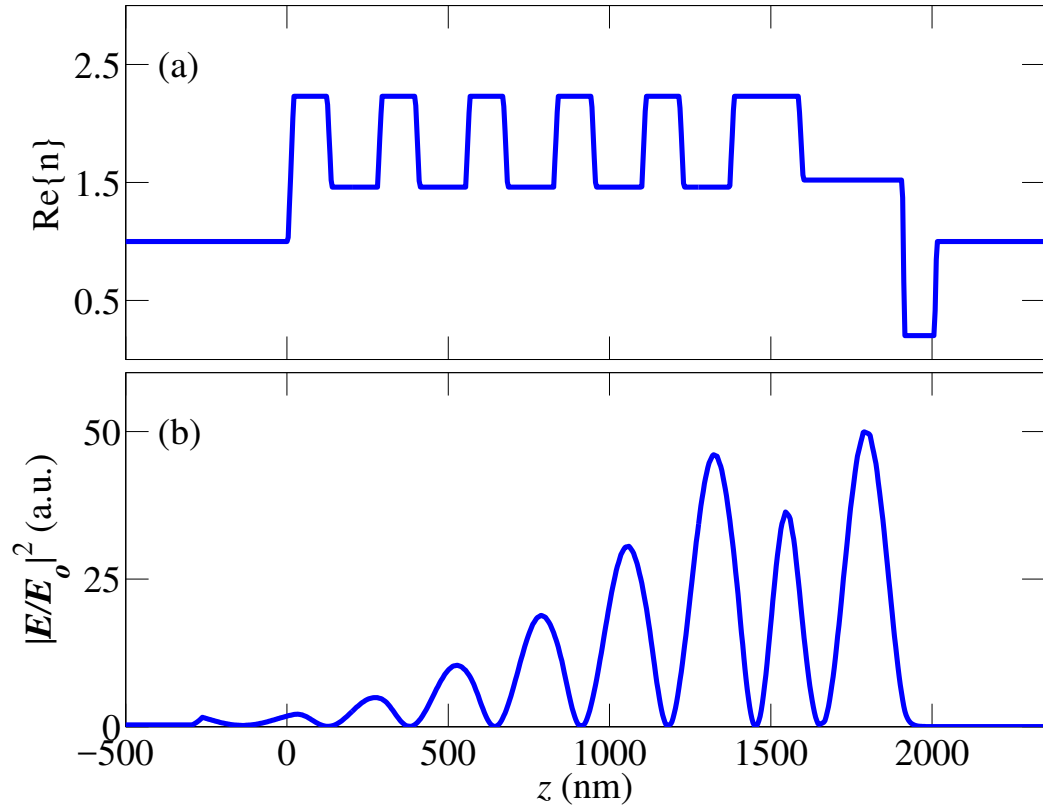


Figure 4.12: (a) Refractive index profile of the OTS structure. (b) Normalized electric field intensity distribution in OTS structure.

To investigate the underlying mechanism of OTS resonance, we plot electric field intensity profile throughout this OTS structure in Fig. 4.12 at 870 nm wavelength. As seen from this figure, we get approximately  $50\times$  enhancement of electric field intensity in the spacer region near the Au layer. This increased electric field intensity leads to enhanced absorption at resonant wavelength. While this behavior of increased absorption at metal-dielectric interface is similar to surface plasmon polariton resonance, it is to be noted that the confinement achieved in OTS is not due to the negative real value of dielectric permittivity of metal, it is rather due to the

stopband of PhC [75].

Spectral position of this resonance is highly sensitive to the thickness of the spacer layer,  $d_s$  and the thickness of the last TiO<sub>2</sub> layer,  $d_l$ . For optically thin metals, the resonant wavelength also depends on film thickness to some extent [76]. In Fig. 4.13, calculated the reflection spectra for variation of  $d_s$  and  $d_l$  is shown. Redshifting of reflection dip with increasing spacer thickness and terminating TiO<sub>2</sub> is observed.

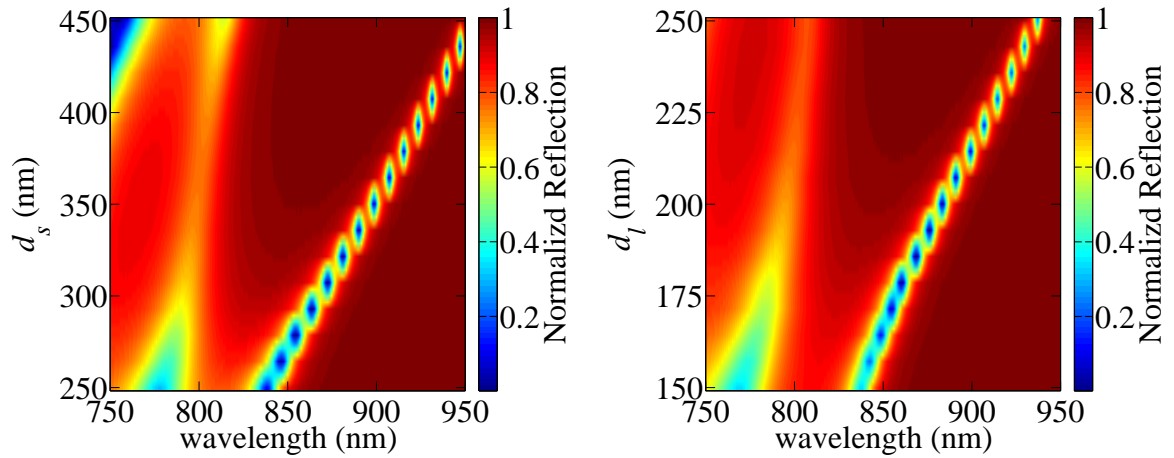


Figure 4.13: Reflection spectra demonstrating the behavior of OTS resonance as spacer thickness,  $d_s$  and terminating TiO<sub>2</sub> thickness,  $d_l$  are varied.

In the following section, we explore how the optical Tamm state can be exploited to increase transmission through sub-wavelength hole array and improve our plasmonic nanocavity performance.

### 4.3.2 Optical Tamm State Enhanced Transmission through Sub-wavelength Hole Array

As mentioned previously, optical Tamm states have been reported to increase emission through single nanoapertures. However, to our knowledge, there is no report of

using this resonance to enhance emission through metallic nanohole arrays with sub-wavelength periods. In this section, we will incorporate 1D PhC on top of plasmonic nanohole array cavity to improve emission characteristics. In addition to that, we will explore the feasibility of tuning extraordinary emission resonance wavelength by engineering the PhC layers.

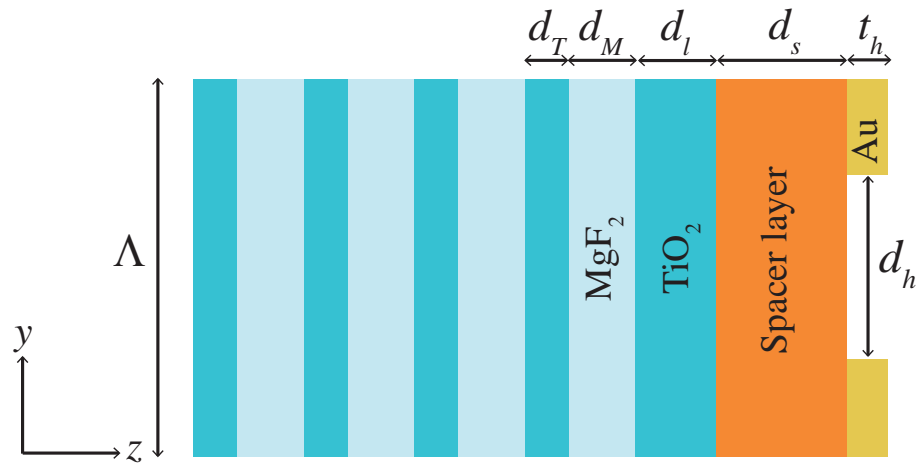


Figure 4.14: Cross-sectional view of the proposed nanohole array structure using 1D PhC.

The proposed structure for this study is similar to the one described in the preceding section. However, in this case, the 100 nm thick Au layer was perforated with periodic square holes of sub-wavelength dimensions. The lattice period of the hole array is 350 nm and the width and breadth of the square hole are 170 nm. Apart from the nanohole array, the dimensions of the PhC constituents and spacer layer remain unchanged. Cross-sectional view of the structure is shown in Fig. 4.14. For this structure, light is normally incident from the photonic crystal side of the structure. We measure the normalized transmission through the nanoholes as a function of wavelength. In Fig. 4.15 we compare the emission spectra of the bare nanohole array (with spacer layer, without PhC) and the proposed OTS structure. There are few

things to note in this plot. Inclusion of PhC structure to the nanohole array leads to substantial improvement of transmission intensity. Additionally, the linewidth of the transmission spectra also narrows significantly which indicates stronger resonance. Moreover, the the transmission at 800 nm is significantly reduced. As a result, if such structure is used as nanocavity, the forward scattering of pump beam to output will be significantly suppressed.

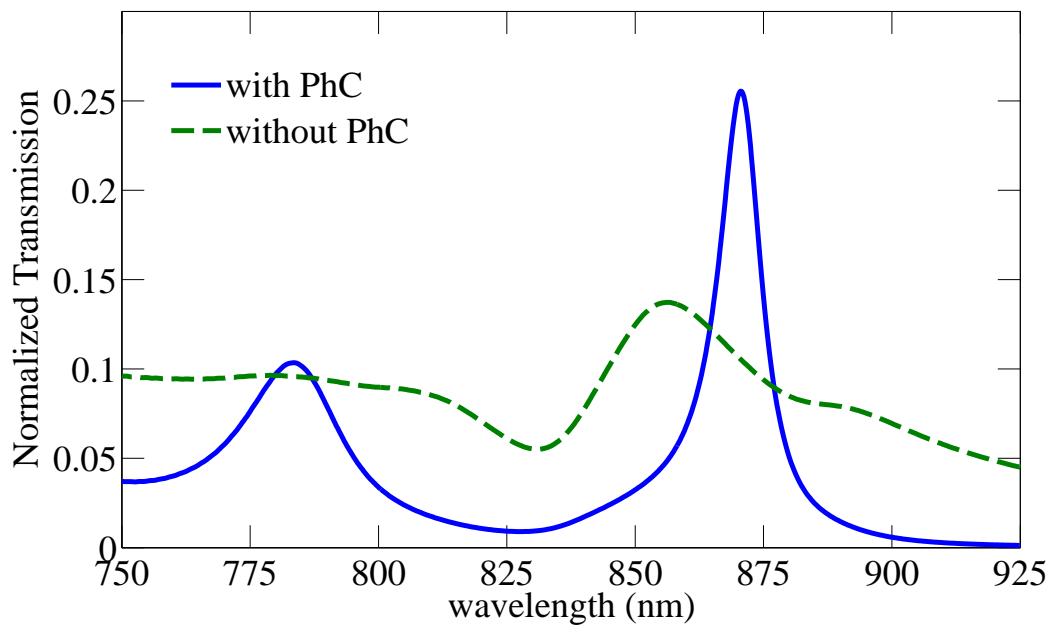


Figure 4.15: Transmission spectra showing the increased transmission through nanohole array due to inclusion of 1D PhC.

To probe the effect of PhC on periodic nanohole structure, we plot the electric field intensity distribution throughout the structure at resonant transmission wavelength. From Fig. 4.16 we note increased intensity of electric field in the vicinity of the spacer layer similar to what observed in the previous section at OTS resonant wavelength. Electric field confinement at the edges of square hole is also observed which shows the localized hole resonance contributing to extraordinary transmission. Therefore, even for periodic nanohole array, field enhancement associated with optical Tamm state

can lead to increased coupling to radiative modes through sub-wavelength holes.

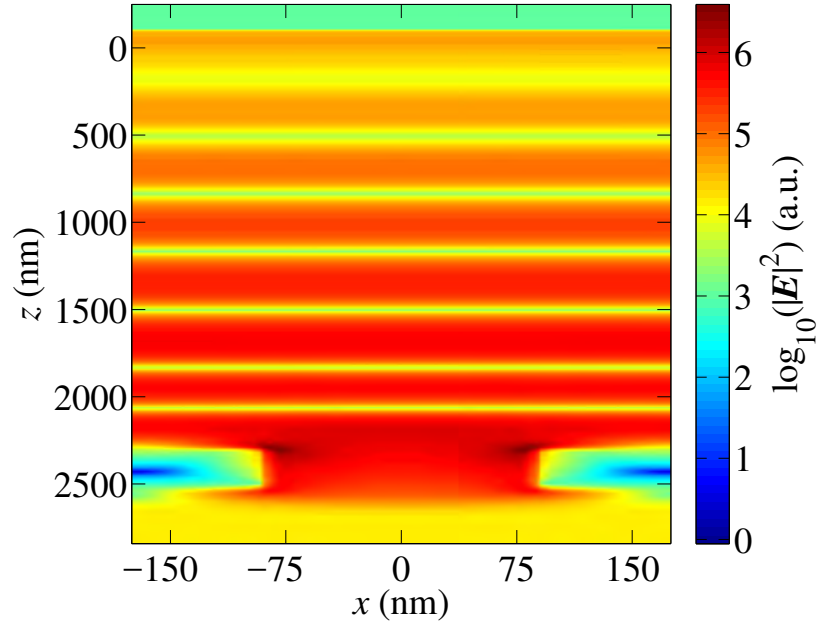


Figure 4.16: Electric field intensity distribution throughout the structure with 1 dimensional photonic crystal on top of square nanohole array.

As discussed in previous section, reflection dip in OTS structure shows high sensitivity to a number of structural parameters. In this part of the study, we explore the feasibility of tuning the transmission peak of the proposed nanohole array structure in similar manner. We have varied the spacer layer thickness,  $d_s$  and terminating  $\text{TiO}_2$  layer thickness,  $d_l$  and calculated the transmission spectra. Figure 4.17 shows that peak transmission wavelength changes significantly as  $d_s$  and  $d_l$  are varied. We also note that this change of peak transmission correlates well with the reflection minima previously observed in Fig. 4.13. In designing our plasmonic nanoresonator with this structure, it provides a convenient approach to tune the resonant wavelength of the cavity. Moreover, compared to spectral shift in resonance due to changing hole shape, dimension or metal thickness, changing PhC layer thickness provides the opportunity to tune resonance over a wider range of wavelengths.

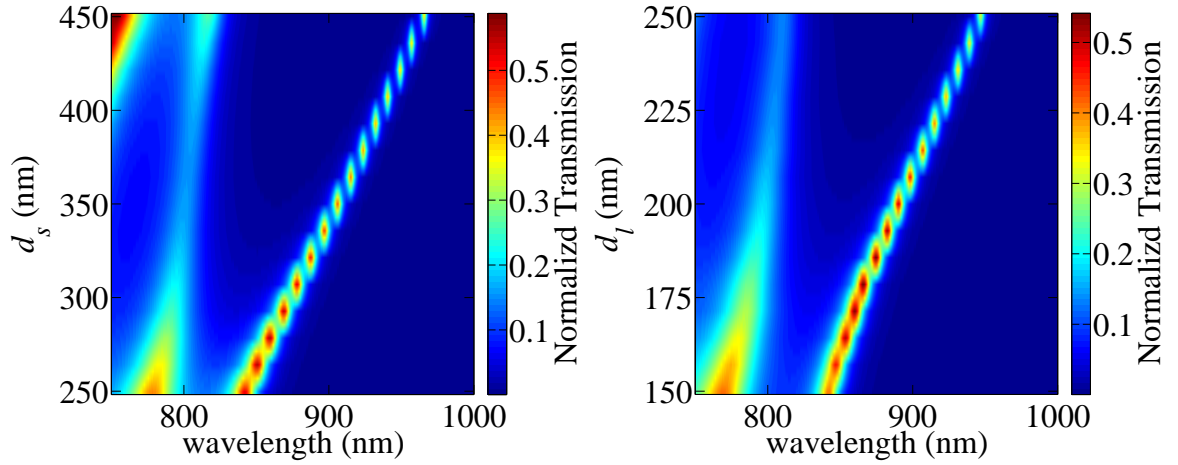


Figure 4.17: Normalized transmission spectra as spacer thickness,  $d_s$  and terminating  $\text{TiO}_2$  thickness,  $d_l$  are varied.

## 4.4 Summary

In this chapter, we have investigated plasmonic nanocavity design in great detail. Among different types of nanocavity designs, we concentrated on metallic nanohole array based plasmonic nanoresonator. Then, we studied shape resonance occurring in such periodic nanohole structures, and designed a structure suitable for nanolaser operation in near-IR region. However, as we discovered, plasmonic nanohole array alone led to inefficient laser performance. To improve this nanocavity response, we explored the idea of using 1 dimensional photonic crystal structure on top of the metallic nanohole array. Using the optical Tamm state surface mode near the metallic interface, we were able to achieve almost 90% improvement in emission intensity. Moreover, the forward scattering of pump beam through the nanohole structure was also reduced by approximately 80%. Inclusion of photonic crystal on top of plasmonic structure also facilitated convenient tuning of the nanoresonator over a wide band of wavelength. All of these improvements make this plasmonic nanohole array structure with 1D PhC a viable nanocavity to achieve highly efficient plasmonic nanolasing. In



the next chapter, we investigate the performance of a plasmonic nanolaser using this optimized cavity.

# Chapter 5

## Proposed Nanolaser

In the previous chapter, we have discussed our design methodology of plasmonic nanocavity for nanolaser. The structure is based on plasmonic nanohole array with sub-wavelength periods. To enhance the performance and efficiency of this cavity, a 1 dimensional photonic crystal was added on top of this metallic nanohole array. Previously, we have measured the transmission and reflection characteristics of the passive nanocavities in absence of gain medium. In this chapter, we will conduct laser simulation with active gain medium and optical pumping. We will investigate and analyze the lasing performance of the designed nanolaser in response to different optical pumping intensity. In addition, we will explore the contribution of the photonic crystal structure and the plasmonic nanohole array structure in operation of laser design. We will also study how the thicknesses of gain layer and photonic crystal affects the stimulated emission spectra. Moreover, we will analyze the far-field radiation pattern and calculate divergence angle of the designed nanolaser structure.

## 5.1 Nanolaser Design and Simulation Setup

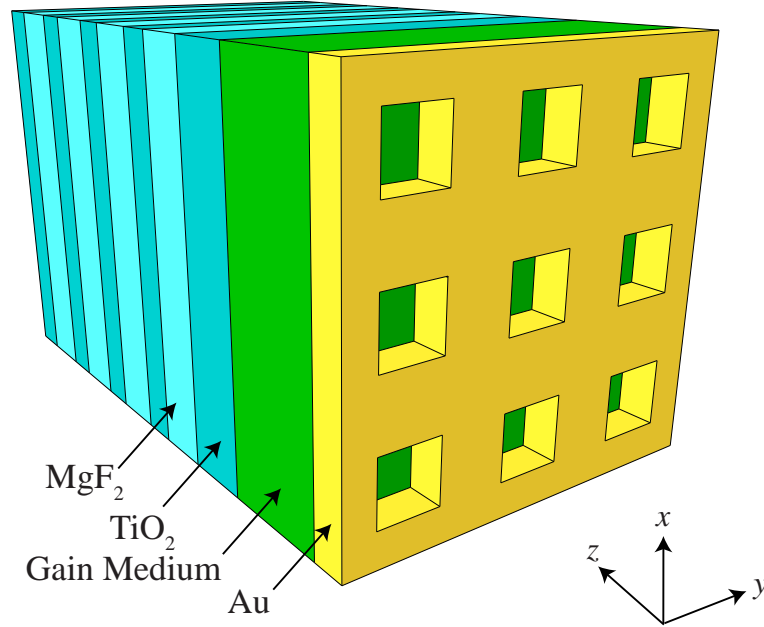


Figure 5.1: Schematic of the Nanolaser structure consisting of 1D photonic crystal terminated by Au nanohole array with square holes. The 1D PhC is formed by alternating layers of  $\text{TiO}_2$  and  $\text{MgF}_2$ . Gain material thickness is 350 nm and metallic layer thickness is 100 nm. The holes have width and breadth of 170 nm and periodicity of 350 nm.

The proposed plasmonic nanolaser structure in this work uses the optimized plasmonic nanocavity structure designed in the last chapter. However, the spacer layer in that structure is substituted by the gain medium. The schematic of the laser structure is shown in Fig. 5.1. Cross-sectional view of the proposed structure is illustrated in Fig. 5.2. This nanolaser structure consists of Au layer perforated with periodic square nanohole array. This structure is covered by a gain medium. The gain medium is Polyurethane(PU) layer mixed with near infrared fluorescence dye molecule IR-140 [16]. Alternating layers of  $\text{TiO}_2$  and  $\text{MgF}_2$  is deposited on top of the gain material which forms a 1 dimensional photonic crystal (PhC) structure. We denote the number

of pairs of  $\text{TiO}_2$ - $\text{MgF}_2$  layers in PhC by  $N$ . The  $\text{TiO}_2$  and  $\text{MgF}_2$  layer thicknesses of the PhC are denoted by  $d_T$  and  $d_M$  respectively. A  $\text{TiO}_2$  layer of thickness  $d_l$  connects the photonic crystal structure to the laser gain medium. The nanohole width and thickness are represented by  $d_h$  and  $t_h$ .

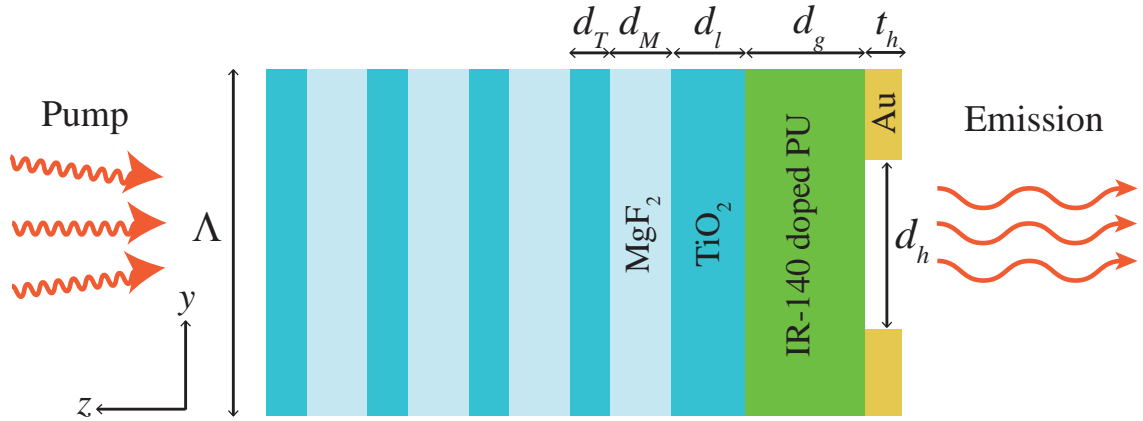


Figure 5.2: Cross-sectional view of unit cell of the proposed nanolaser structure. This section is taken through the center of the square nanohole. Here,  $t_h = 100$  nm,  $d_g = 325$  nm,  $d_l = 200$  nm,  $d_M = 165$  nm,  $d_T = 108$  nm,  $d_h = 170$  nm,  $t_h = 100$  nm, and  $\Lambda = 350$  nm.

We have numerically solved the structure using a full-field vectorial electromagnetic simulator Lumerical FDTD Solutions. The optical parameters of Au was taken from Johnson and Christy [54]. The electromagnetic simulator uses multi-coefficient model to account for the dispersive nature of Au in near-IR region. The refractive indices of  $\text{TiO}_2$  and  $\text{MgF}_2$  are set to be 2.23 and 1.36 respectively. The gain material of this laser device IR-140 is modeled as 4-level 2-electron system. Theory of this material modeling was discussed in section 3.4.1. Since, IR-140 is mixed in Polyurethane, the base refractive index of the gain material was chosen to be that of the Polyurethane (1.51). Unless otherwise specified, number of pairs of  $\text{TiO}_2$ - $\text{MgF}_2$  layers,  $N$  is 5. In numerical simulation, the structure was assumed to be infinitely

periodic in  $x$  and  $y$  direction. Therefore, periodic Bloch boundary condition was chosen in both  $x$  and  $y$  direction. Perfectly matched layers (PML) was set on the  $z$  boundaries. Due to its periodicity, we only simulated a single unit cell of the structure spanning  $\Lambda = 350$  nm in  $x$  and  $y$  direction to calculate the response of the complete structure. Considering the symmetry of the device in  $x$  and  $y$  direction, symmetric and anti-symmetric boundary conditions were applied to reduce the computational time significantly.

Our proposed device is designed for room-temperature operation under optical pumping. In simulation, the structure was pumped using a 40 fs plane wave pulse, centered at 800 nm wavelength. Unless otherwise specified, pump pulse is assumed to be normally incident from the PhC side of the device and emission is observed from the other side. To record lasing emission, a frequency domain field monitor is placed on the emission side. Emission at different wavelengths was calculated by integrating the poynting vector normal to this field monitor.

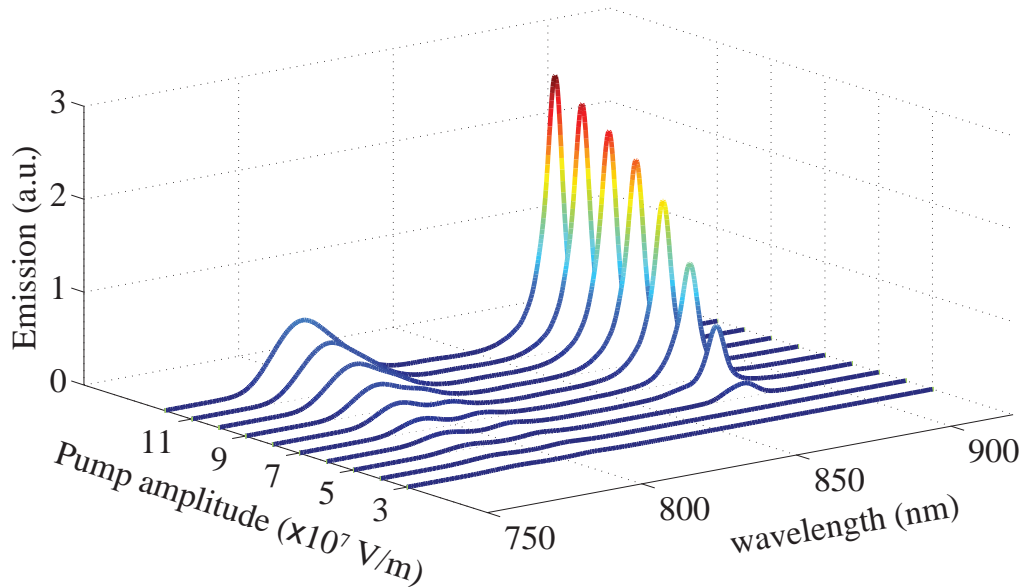


Figure 5.3: Emission spectra for different pump intensities.

## 5.2 Performance Analysis

We have simulated the structure under optical pumping for a range of pumping amplitudes and the recorded emission spectra is presented in Fig. 5.3. As we can see from this figure, for pump amplitudes below  $5 \times 10^7$  V/m, there is negligible emission around the lasing wavelength. As pumping amplitude is increased beyond this value, onset of lasing emission around 870 nm is observed. We can also observe that, the linewidth of the emission narrows to approximately 4-5 nm from 11-12 nm with increasing pumping intensity.

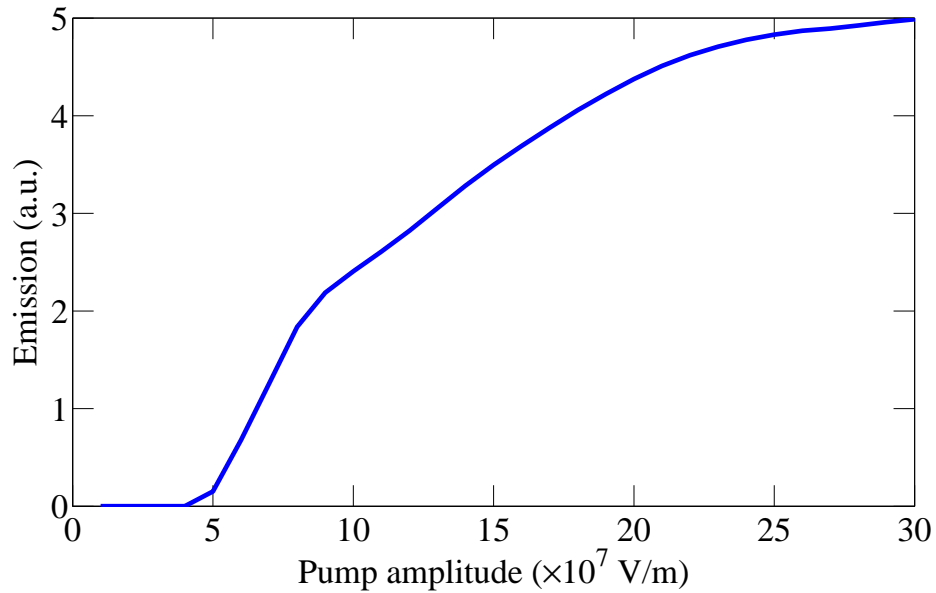


Figure 5.4: Emission characteristics of the nanolaser as a function of pumping amplitude. This laser shows threshold behavior at approximately  $5 \times 10^7$  V/m of input pump amplitude.

Figure 5.4 shows the peak of lasing emission as function of input pump amplitude. From this figure, the threshold behavior at  $5 \times 10^7$  V/m is quite apparent. As pumping intensity is increased, intensity of lasing keeps on increasing almost linearly. However, for peak pump amplitude beyond  $2.5 \times 10^8$  V/m, we note that emission begins to

saturate. The occurrence of lasing within this structure is evidenced by narrowing of linewidth, threshold and saturation behavior.

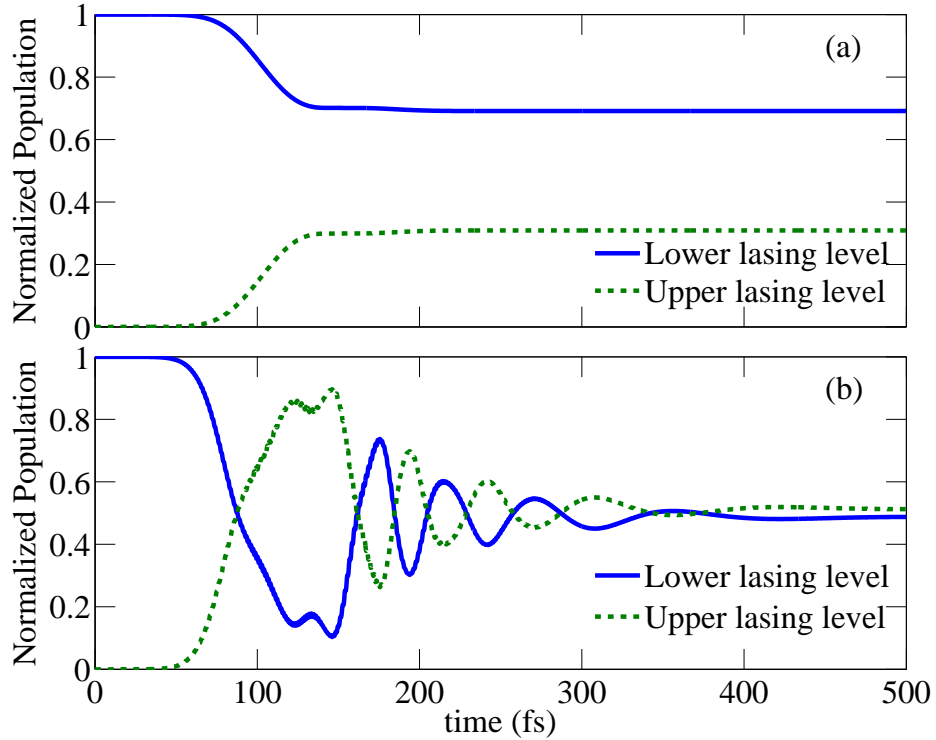


Figure 5.5: Time evolution of normalized population densities of upper and lower lasing levels. This measurement is taken at a point 10 nm away from nanohole edge (a) for  $0.8 \times$  pump threshold (b) for  $1.2 \times$  pump threshold.

To observe temporal response of the gain medium modeled by 4-level 2-electron system, we have plotted the normalized population of two lasing levels in Fig. 5.5. Figure 5.5(a) shows the case when pumping amplitude is just below threshold ( $4 \times 10^7$  V/m). At this pumping intensity, lasing levels fails to reach inverted populations. For pumping above threshold ( $6 \times 10^7$  V/m) as shown in Fig. 5.5(b), population inversion is achieved at approximately 100 fs. We also note the onset of lasing emission as evidenced by the drastic change of populations levels around 150 fs.

### 5.3 Effect of 1D PhC

The proposed laser is capable producing single mode lasing emission at room temperature in the near-IR range. The nanohole arrays in the structure couples highly confined plasmonic modes which supports extraordinary transmission. The feedback necessary for lasing action is obtained from these plasmonic resonant modes coupled in the near-IR wavelengths. Moreover, to further improve the lasing performance, we have incorporated 1 dimensional photonic crystal on top of the gain medium. This PhC structure forms optical Tamm state (OTS) which produces field enhancement near the metallic layer and leads to substantial improvement of lasing emission compared to the bare nanohole array structure with the gain medium.

We have systematically investigated the role of photonic crystal structure in improving lasing emission of the proposed structure. In the previous chapter, we have looked into the optical response of the passive structure. The normalized transmission spectra for this passive structure with and without PhC layers was plotted in Fig. 4.15. In absence of PhC, the Au nanohole array shows a relatively broad emission peak at 860 nm. This peak corresponds to single hole resonance of square nanohole array. However, when PhC is added on top of this nanohole structure, we observed approximately two-fold enhancement in emission and significant narrowing of transmission linewidth. We also observed reduced transmission around 800 nm wavelength. This reduced transmission aids in suppressing frequency components of pumping pulse in the output emission. To understand how these improvements of transmission spectra translates into laser performance, we look into results from complete laser simulations with gain material.



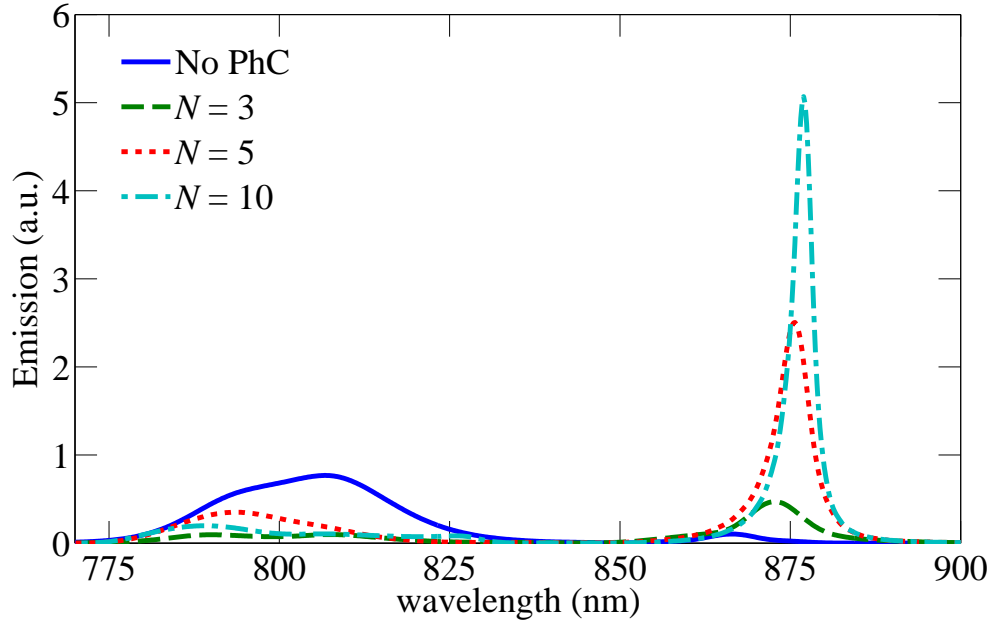


Figure 5.6: Emission spectra of the proposed nanolaser structure for different number of 1D PhC layers. Here,  $N$  = pairs of  $\text{TiO}_2$  and  $\text{MgF}_2$  layers in PhC.

In Fig. 5.6 we compare the emission spectra of a laser device with varying number of  $\text{MgF}_2$ - $\text{TiO}_2$  pairs,  $N$  with a design without the PhC. For the structure without PhC, the gain material is sandwiched between a 200 nm thick  $\text{TiO}_2$  and metal hole array with thickness of 100 nm. Very low intensity and broad emission around 860 nm is observed for this design. However, as increasing numbers of PhC layers are added to the structure, we notice that emission intensity increases almost by an order of magnitude. Additionally, the emission shows increased spectral coherence as pronounced linewidth narrowing is observed. Moreover, inspecting the spectrum around 800 nm wavelength, we note that adding layers of PhC suppresses the components of scattered pump beam in output side.

To summarize, including PhC layer in nanohole array nanolaser design improves laser performance in three ways. Firstly, emission intensity increased as efficiency of outcoupling to free space radiation is improved via optical Tamm state resonance.

Secondly, increased spectral coherence is achieved as a result of linewidth narrowing. Thirdly, the scattering of pump pulse to the output side is suppressed.

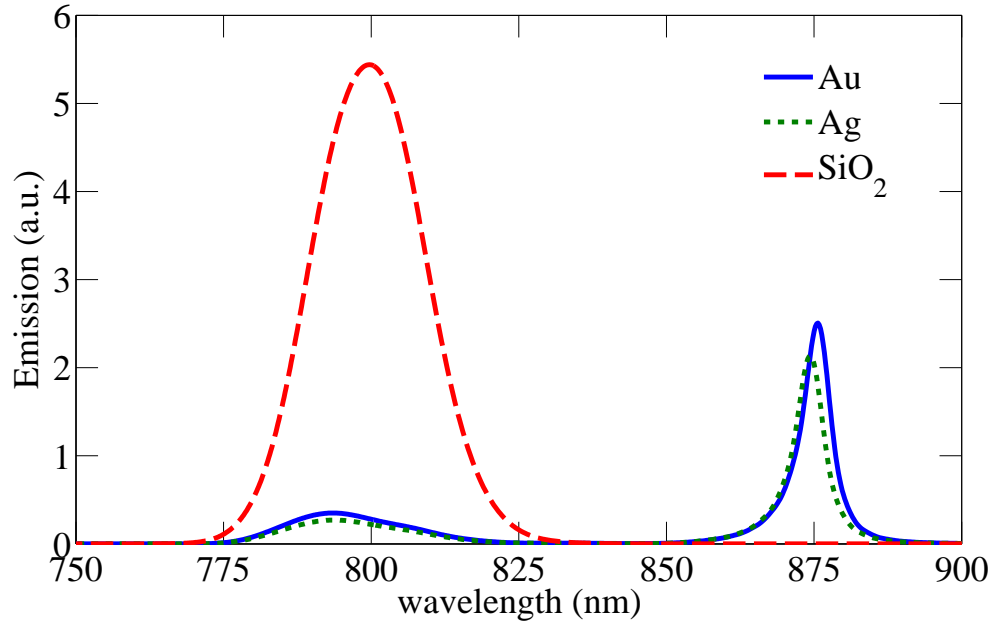


Figure 5.7: Emission spectra for nanolaser structures with Au, Ag, and Silica nanohole array of the same dimension.

To delineate the vital contribution of plasmonic mode in the operation of this device, we have simulated few other structures replacing the Au nanohole array. Firstly, the Au nanohole array was substituted by a Silica nanohole array of the same dimensions and lattice period. We observe that even for high pumping intensity, there was no lasing in such device. The emission spectra for this structure is shown in Fig. 5.7. Upon further investigation of the population levels of this structure, we found that at high enough pump, the gain medium reaches population inversion, but fails to support lasing emission. This is due to the fact that, despite the high population inversion, Silica nanohole array cannot provide sufficient feedback essential for lasing action. We also experimented with Ag nanohole array, which produced lasing emission by facilitating feedback action through plasmonic modes between Ag

and gain material.

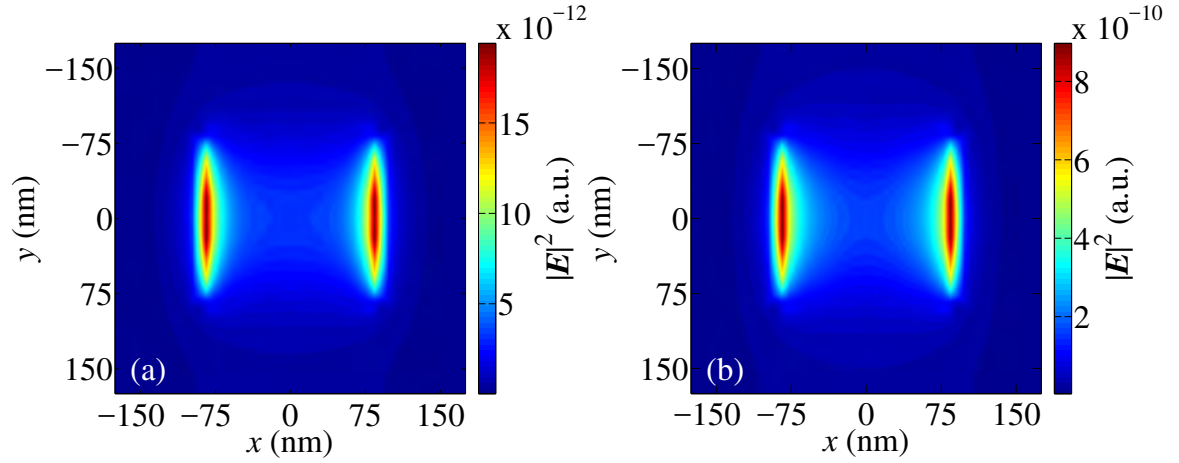


Figure 5.8: E-field intensity in the vicinity of the square hole array at lasing frequency(XY plane). (a) Bare plasmonic nanohole array structure (b) Proposed nanolaser structure with 1D PhC.

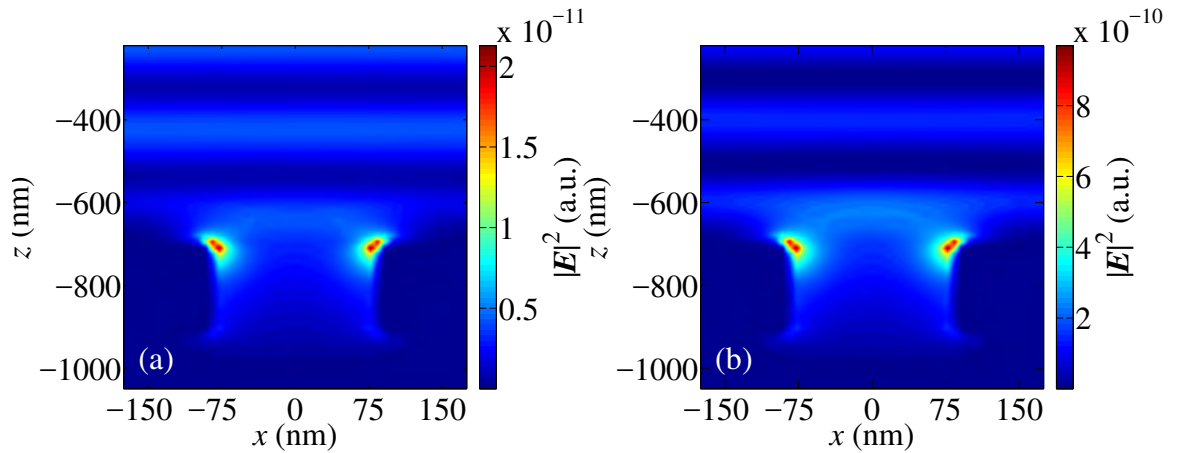


Figure 5.9: E-field intensity in the vicinity of the square hole array at lasing frequency(XZ plane). (a) Bare plasmonic nanohole array structure (b) Proposed nanolaser structure with 1D PhC.

To further our understanding of the underlying mechanisms of lasing and contribution of PhC structure, we have looked into electric field distributions at different

sections of the laser structure. Figure 5.8 shows electric field intensity distribution of the unit cell of the nanolaser at the interface between Au nanohole array and gain medium. For bare nanohole array structure, as shown in Fig. 5.8(b), we observe field enhancement on the sides of square holes. This field profile is characteristic to localized surface plasmon modes. Moreover, the resonance observed in this figure is for single hole resonance, as mode coupling between adjacent holes is negligible. We conclude that resonances of individual nanoholes leads to lasing emission from the device. In Fig. 5.8(a), field profile along the same nanohole array-gain medium interface is shown for the structure with 1D PhC. While the mode profile is similar to that of the bare nanohole array structure, we observe from the scale bar that intensity is enhanced by two orders of magnitude due to inclusion of PhC structure. We attribute this enhancement to coupling of optical Tamm state modes from 1D PhC resulting in increased coupling of plasmonic mode which in turn leads to improved lasing emission. Figure 5.9 shows the field profile of proposed nanolaser structure and bare nanohole array structure along the XZ plane taken through the center of nanohole. Similar field enhancement and high confinement of modal profile is observed in this plane as well.

## 5.4 Tuning Mechanisms of Emission Wavelength

Emission of proposed plasmonic nanolaser structure can be engineered in a multitude of ways. Spectral position of plasmonic resonance depends on the nanohole array structure, its dimension and periodicity. Moreover, the optical Tamm state resonance can be tuned with the dimensions of the dielectric layers and the gain layer.

### 5.4.1 Terminating TiO<sub>2</sub> Layer Thickness

It was observed from the study of optical Tamm state resonant modes that the spectral position of the resonances is highly sensitive to the thickness and refractive index of the terminating layer of 1D photonic crystal.

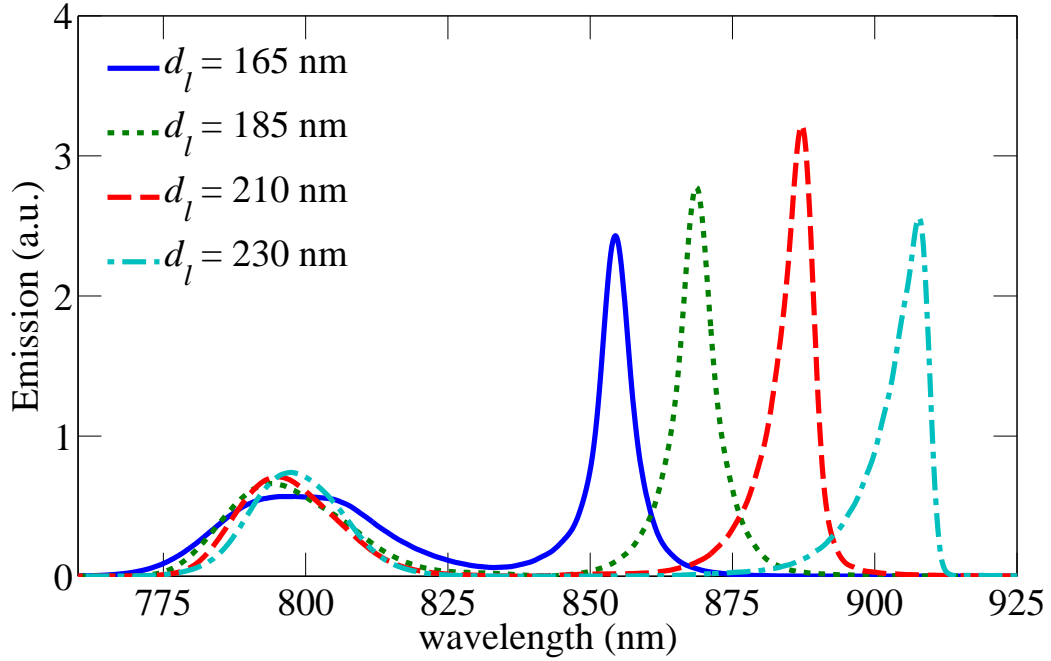


Figure 5.10: Emission spectra of the laser for different TiO<sub>2</sub> layer thicknesses,  $d_l$ .

In proposed structure, we have varied the thickness of the terminating TiO<sub>2</sub> layer,  $d_l$  and observed significant shifting of lasing emission. In our study, emission of proposed nanolaser for values of  $d_l$  from 165 nm to 245 nm were calculated. The results are illustrated in Fig. 5.10. We note that, varying the thickness of this dielectric layer, emission can be tuned from 855 nm to 920 nm. Emission intensity reaches its maxima for layer thickness of 210 nm. We note that emission peak reduces as the peak emission wavelength moves away from 870 nm. This is due to the fact that fluorescence spectra of IR-140 gain medium is centered around 870 nm. As the optical Tamm state resonance moves away from this wavelength, the efficiency of

energy transfer between plasmonic mode and gain medium is reduced. As a result, reduced emission intensity is observed.

### 5.4.2 Gain Layer Thickness

Figure 5.11 shows the emission spectra for different gain layer width ranging from 275 nm to 415 nm. In this figure, we observe that, the peak wavelength of lasing emission shifts from 860 nm to 920 nm. The peak intensity of the emission reaches maximum when the gain medium thickness is around 320 nm. Further increment of gain medium width did not result in lasing emission. As the gain medium thickness is varied, the spectral characteristics around 800 nm wavelength change.

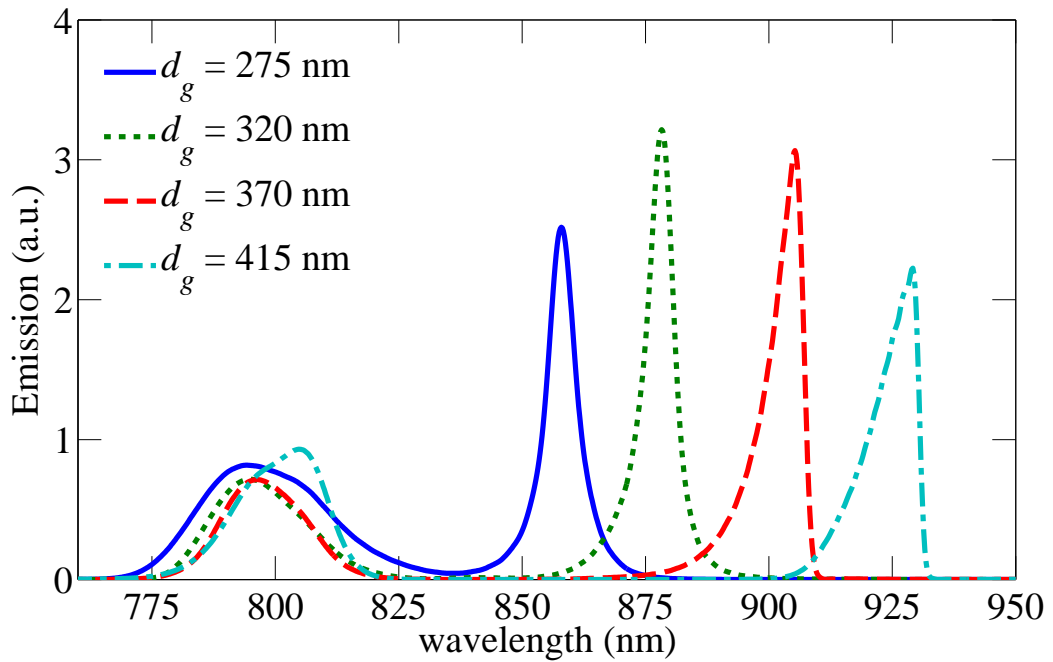


Figure 5.11: Emission spectra of the laser for different gain material thicknesses,  $d_g$ .

### 5.4.3 Nanohole Depth and Width

We have studied the effect of variation of nanohole depth ( $t_h$ ) and width ( $d_h$ ) on the proposed nanolaser performance. Compared to the variation of gain and terminating TiO<sub>2</sub> layer thickness, relatively small spectral shift of lasing emission is observed. The results are presented in Fig. 5.12. Hole depth,  $t_h$  was varied from 50 nm to 400 nm and hole width,  $d_h$  was varied from 50 nm to 200 nm. Lasing emission demonstrates shift of approximately 3 nm for hole depth variation and 15 nm for hole width variation. We see that, for low values of hole depth, high intensity lasing is observed. When the depth is increased, lasing intensity decreases monotonically (Fig. 5.12(a)) and lasing is not observed beyond 300 nm of hole depth. Lasing peak remains within  $886 \pm 1.5$  nm. Similarly, Fig. 5.12(b) shows spectral response for variation of width of the square nanoholes from 50 to 200 nm. We observed as hole width is increased, peak lasing wavelength changes from 892 nm to 877 nm. We note that, plasmonic lasing intensity is significantly reduced with decreasing hole width. This can be attributed to the increased metallic loss in the nanohole array. The gain material cannot sufficiently compensate this loss which results in reduced lasing emission.

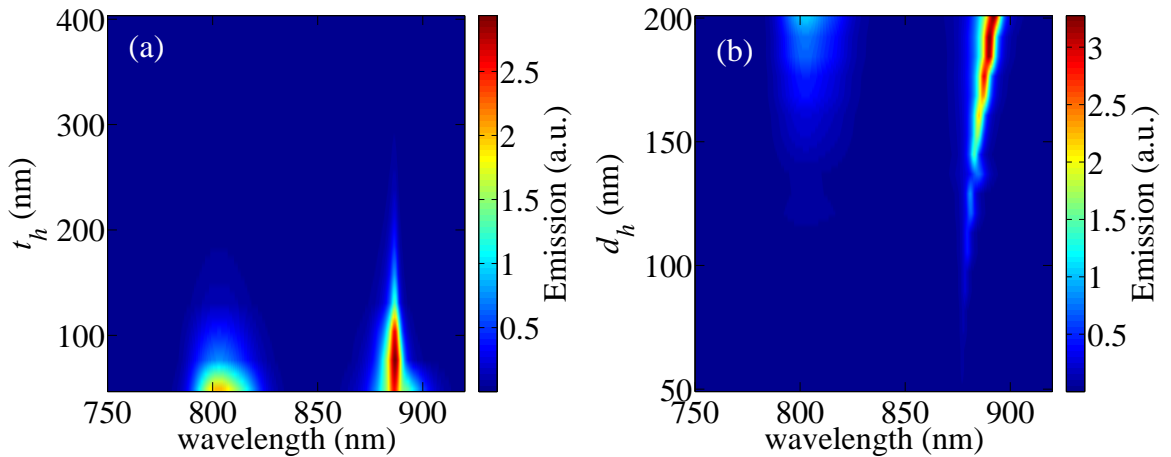


Figure 5.12: Effect of (a) hole depth and (b) hole width on lasing spectra.

#### 5.4.4 Angle of Incidence of Pump Pulse

The results and analysis of the proposed structure mentioned thus far in this work has used input pump pulse normally incident on the nanolaser structure. In this section, we analyze the system with obliquely incident pumping pulse. Figure 5.13 presents transmitted spectra for pumping pulse incident at a number of angles. The incident angle has been varied from  $0^\circ$  to  $25^\circ$ . As angle of incidence is increased, the lasing intensity decreases monotonically. Moreover, the lasing emission shows blueshift from 880 nm to 858 nm. This blueshifting of lasing emission can be explained with theoretical calculation by transfer matrix method [80]. The linewidth of the emission remains sufficiently narrow despite the spectral shift.

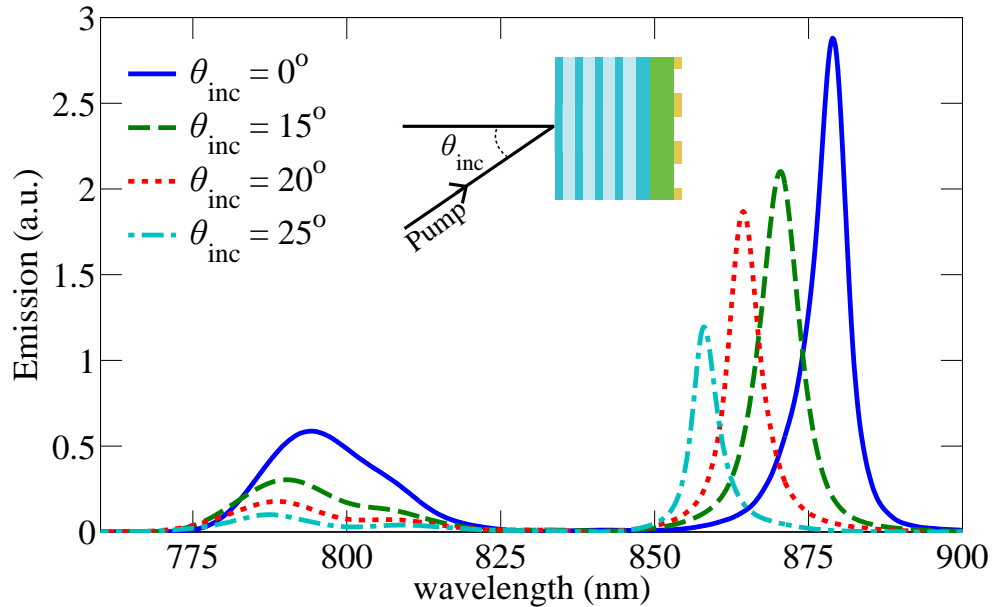


Figure 5.13: Emission spectra of the laser for different angles of incidence.

From the preceding discussions, we can see that lasing emission is highly sensitive to gain layer and terminating  $\text{TiO}_2$  layer thicknesses. These parameters can be utilized to engineer the laser emission peak. However, the spectral shift induced by the



different angle of incidence provide the option to tune laser emission in real-time.

### 5.4.5 Polarization of Incident Pump Pulse

Our proposed structure has symmetry along both x and y axes. As a result, the emission spectra is identical for  $0^\circ$  and  $90^\circ$  polarization of pump beam. In Fig. 5.14, emission spectrum for normally incident pumping pulse with polarization of  $45^\circ$  to high symmetry axis is shown. At this polarization, the lasing emission occurs at the same wavelength for polarization along high symmetry axis.

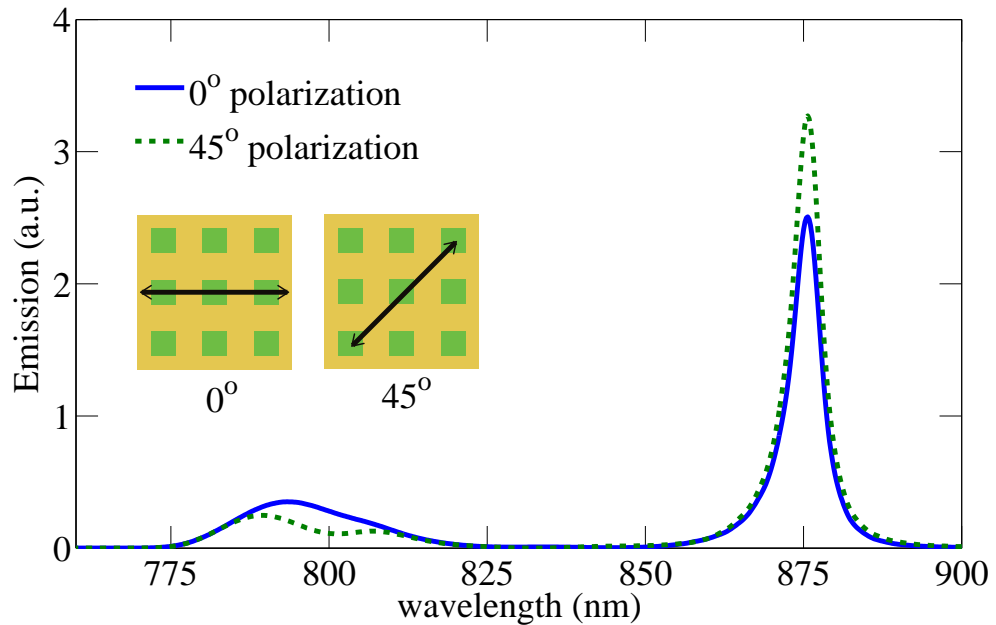


Figure 5.14: Emission spectra of the laser for different polarizations of input pulse.

## 5.5 Far-field Directionality

Achieving far field directional radiation is one of the challenges of plasmonic lasers. Structures using propagating modes at metal-dielectric interface suffers from the difficulty associated with coupling the interface-confined surface plasmon polariton mode

to the radiative mode in free space. As surface plasmon polariton dispersion lies below the light line, there is a huge mismatch between the wave-vectors of plasmonic mode and that of the free-space mode, which in turn results in diverging beams from such structures.

To calculate the far field emission patten of the given laser structure, Near field to far field transformation tool included in Lumerical FDTD solutions was used. The far field data was obtained by transforming near field data obtained with a frequency domain field profile monitor placed on the emission side of the laser. The lasing simulations were carried out using periodic boundary conditions, which assumes the structure to be infinitely periodic. However, to obtain far field data, the finite dimensions of the device along x and y axis is necessary. For far field simulation the structure was assumed to spanning  $70 \mu\text{m}$  in both x and y direction.

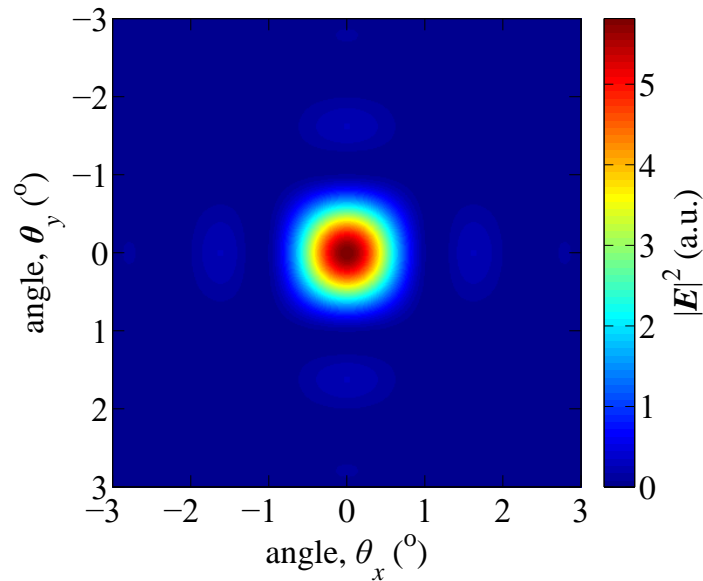


Figure 5.15: Far field E-field intensity distribution. Far-field simulations were run considering a structure of  $70 \mu\text{m} \times 70 \mu\text{m}$  dimension with plane wave incident on the structure.

Apart from the dimensions of the periodic structure, ‘top hat’ type illumination

was assumed for pumping pulse. As opposed to ‘Gaussian’ illumination, ‘top-hat’ illumination assumes that the pumping beam width is much larger than total device dimension. In other words, total device is uniformly illuminated by the source.

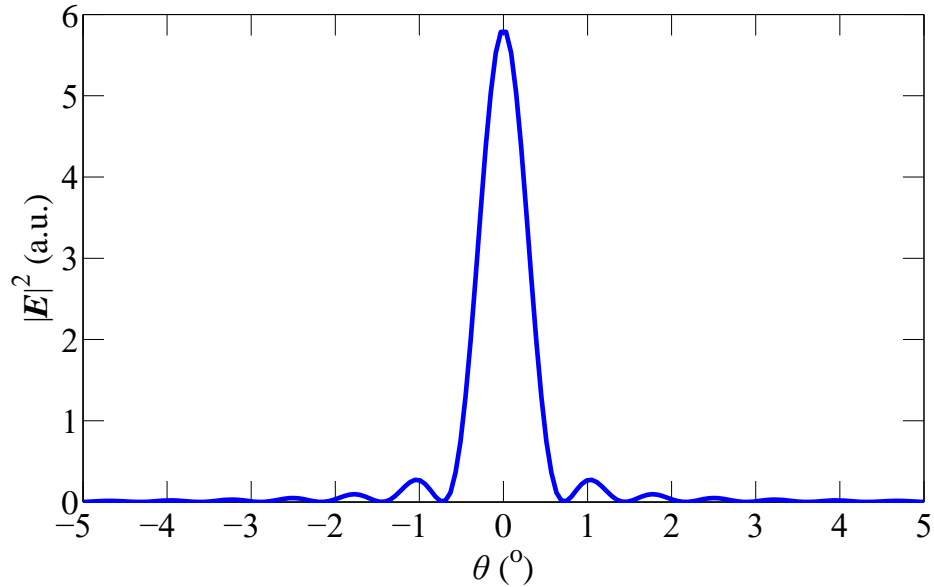


Figure 5.16: Far field E-field intensity distribution as a function of polar angle,  $\theta$ .

The plasmonic mode utilized in the proposed structure is localized mode present in individual holes. In this structure, the square holes can be assumed to be acting as dipole emitters radiating coherent spherical waves. These spherical waves interfere constructively in far field to produce directional emission in along the surface-normal direction. The resulting far-field emission at 1m is presented in Fig. 5.15. In this figure,  $\theta_x$  and  $\theta_y$  denotes the angle the surface normal (along z-axis) forms along x and y axis respectively. We observe very small divergence angle of  $\approx 1^\circ$ . This order of divergence angle is in agreement the experimental reports of extraordinary transmission with subwavelength periodic perforations [15]. The Fig. 5.16 shows the far field emission profile for a range of polar angle,  $\theta$  for fixed value of azimuthal angle,  $\phi = 0^\circ$ . Along with the small divergence angle centered at  $0^\circ$ , we observe sinc

function like pattern which is expected from rectangular aperture.

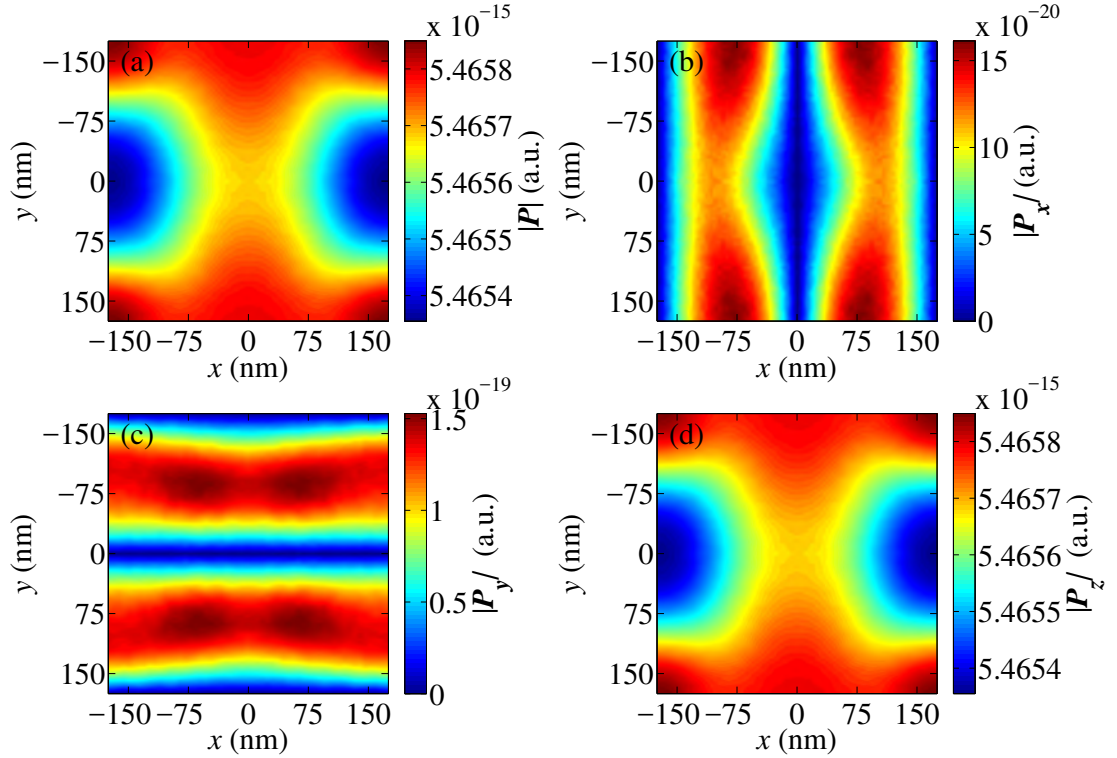


Figure 5.17: Magnitudes of poynting vector recorded in near field monitor at lasing frequency. (a) magnitude of poynting vector (b-d) orthogonal components of poynting vector.

To further analyze the low divergence emission of proposed structure, we look into the magnitude and vectorial components of poynting vectors at the near field monitors. Poynting vector denotes the direction of propagation of a plane wave. Therefore, for a highly directed beam, we expect the component of poynting vector along that direction to significantly dominate over other orthogonal components. Figure 5.18 shows three different orthogonal components of the poynting vector along with its magnitude plot. These data are recorded from the near field monitor placed on the emission side of plasmonic nanolaser. As expected, we observe that the magnitude of poynting vector component along the propagation direction (z-axis) is at least four

orders of magnitude higher than that of other orthogonal components.

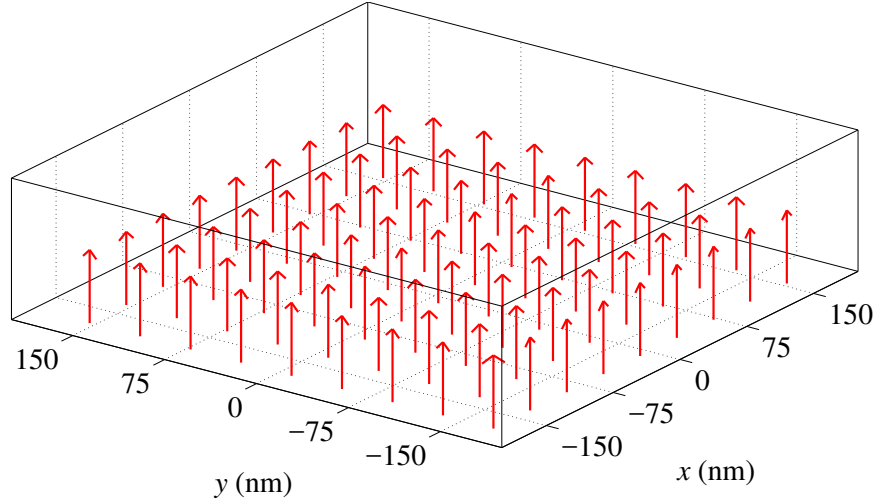


Figure 5.18: Vector diagram of the poynting vectors drawn on the plane of the near field monitor.

Another point we note from this figure is that the  $z$  component of the poynting vector has almost uniform magnitude over the span of the frequency monitor. The consequence of this observation becomes more apparent from Fig. 5.18, where the vector diagram of the poynting vector is drawn on the  $XY$  plane of the near field monitor. Since the magnitude of  $P_z$  is quite uniform throughout the monitor and it dominates significantly over other two orthogonal components, the direction of resultant poynting vector is along  $z$  direction throughout the  $XY$  plane. These results supports the low divergence angle obtained from the near to far-field transformations.

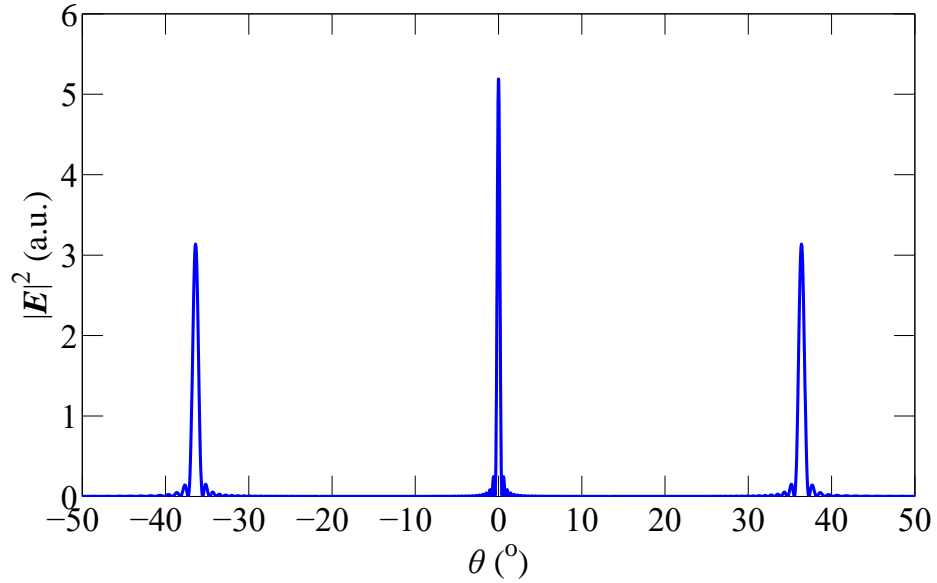


Figure 5.19: Far field distribution of at 800 nm wavelength for a structure with lattice period of 900 nm.

Another important consideration for designing this structure that stemmed from far-field emission was its periodicity. The period of the nanohole arrays was chosen to be 350 nm which is sub-wavelength in the region of operation. Due to this sub-wavelength periodicity, the emission occurs only for zeroth order mode and higher order modes are cut-off. In case of periodicity in the order of wavelength, emission would be distributed into multiple order of diffracted mode. Far field emission at 800 nm for a structure of 900 nm lattice period is demonstrated in Fig. 5.19. In this figure we see off-normal emission at  $\pm 37^\circ$ . Such diffracted modes causes emitted power to be divided into each of these modes. Therefore, to achieve single narrow-beam emission normal to the device, sub-wavelength period was chosen.

## 5.6 Summary

In this chapter, we have presented our proposed plasmonic nanolaser structure and investigated its performance and design criteria thoroughly. To improve nanocavity performance, we have incorporated 1D PhC on top of the sub-wavelength nanohole array. Doing so improves the cavity performance drastically. This improvement is translated to substantial increase in emission intensity and narrowing of linewidth. Moreover, addition of PhC provides a number of ways to engineer the peak emission wavelength of laser over a wide range of wavelengths. We have thoroughly studied the effect of different design parameters on laser performance. In addition, this plasmonic crystal-based design is also capable of producing highly directional emission in the far-field.

# Chapter 6

## Conclusion and Future Works

In this thesis, we have presented our work on designing an efficient plasmonic nanolaser capable of producing near-IR narrow-beam emission at room temperature. To design such nanolaser, we have studied plasmonic light-matter interaction in metal-dielectric structure and identified fundamental limits and bottlenecks affecting plasmonic nanolaser performance. From the study of previous generations of plasmonic lasers, we have found that laser designs using surface plasmon polariton modes at metal-dielectric layers are prone to the issue of highly divergent lasing emission. For this reason, to design the nanocavity for proposed laser, we chose to focus on plasmonic crystal based structure for its inherently better far-field emission performance. Existing plasmonic crystal based nanolaser exhibits few issues which affect their performance. In many of the such lasers, the emission is coupled into multiple orders of diffracted modes. As a result, lasing energy is distributed into a number of modes leading to reduced intensity. In addition to that, we note that lasing emission is observed in both the transmission side and the reflection side of device. This is another source of inefficiency in such lasers. We proposed designs to increase performance of plasmonic crystal based nanolasers by solving these issues.

To design plasmonic nanocavity, we have chosen square nanohole array in thin



film Au. The lattice period of the nanohole array was chosen to be sub-wavelength. This structure exhibits resonant zero order transmission at wavelengths corresponding to the localized shape resonance of the square holes. Due to the sub-wavelength dimension of the lattice period, only zeroth order diffracted mode can occur under normal incidence. As a result, lasing emission of this nanocavity with gain medium is confined to a single diffracted mode. However, from transmission and reflection spectra, we noted couple of issues with this design. Firstly, emission at lasing wavelength was observed in both the transmission side and reflection side of the device. In addition to that, transmission spectra showed considerable forward scattering of pump beam through the device, which is undesirable in laser output.

To rectify these issues, we explored different approaches to increase extraordinary transmission through the structure. Additionally, we needed to suppress the forward scattering of pump beam in output side. To engineer the spectral property of the nanocavity, we added a one dimensional photonic crystal structure on top of the plasmonic nanohole array design. This photonic crystal was designed in such way that it couples to optical Tamm state modes at lasing wavelength. At optical Tamm resonance, high electric field at the vicinity of metal layer is observed. This enhancement leads to increased coupling to radiative mode through the nanocavity. Consequently, approximately 90% improvement in transmission intensity was achieved. Moreover, the forward scattering of pump beam through nanohole structure was reduced by 80%. Hence, using this nanocavity design, laser simulation produced drastic increase in lasing emission intensity and suppressed pump beam in output spectra. Thus, we could fulfill our primary objective of this thesis of designing an efficient plasmonic nanolaser. In this plasmonic crystal-based design incorporating photonic crystal, we managed to efficiently confine laser emission to the transmission side through the zeroth order of diffraction mode.

Apart from increasing efficiency of the nanolaser system, 1D PhC allows us to

engineer the lasing emission wavelength. By controlling the thickness of PhC layers, we can tune the emission peak over a 60 nm range. Whereas, we can shift the emission wavelength by approximately 15 nm via changing the dimensions of plasmonic nanocrystals. Furthermore, the lasing emission wavelength can be tuned by approximately 20 nm in real-time by changing angle of incidence from  $0^\circ$  to  $25^\circ$ .

In this work, we have also investigated the far-field radiation pattern of the proposed nanolaser design. We have numerically simulated the far-field emission pattern from near-field monitors placed on the transmission side. From calculations, we found this nanolaser shows very narrow-beam emission with divergence angle of approximately  $1^\circ$ . To understand far-field property of this design, the components of Poynting vectors in the near-field monitors were calculated. We observed that the component of Poynting vector normal to the surface of the nanolaser dominates all other components by several orders of magnitude. Therefore, the resultant Poynting vector is oriented along the surface-normal of the device which results in highly collimated beam with very low divergence.

## 6.1 Future Works

While this proposed laser shows remarkable improvement in laser performance, there are still a number of ways to achieve further refinement of device operation.

- The proposed nanocavity is resonant only at lasing frequency. If the cavity can also be made resonant at pumping frequency, it could lead to higher pumping efficiency. One way it could be achieved is through coupling of multiple optical Tamm states. Recently, studies have been published reporting occurrence of multiple Tamm state modes within the stopband of PhC [76]. This phenomena can be explored to reach higher pumping efficiency by designing the structure so that one of the Tamm resonance occurs at pumping frequency and other at

lasing frequency. Another approach that could be taken is to use additional dielectric or metallic nano-particles to induce localized or collective resonance at pumping frequency.

- Metallic corrugations around single nanoapertures have been studied extensively to produce enhanced transmission. To increase emission efficiency of this nanolaser, effect of such corrugations in output side of metallic hole array could also be explored.
- A significant source of loss in this nanolaser design is ohmic loss at metal interface. One way to reduce this loss is to use dielectric spacer layer between gain medium and the metal layer. This could potentially increase spectral coherence of lasing emission.

# Bibliography

- [1] N. Ledentsov, “Quantum dot laser,” *Semiconductor Science and Technology*, vol. 26, no. 1, p. 014 001, 2010.
- [2] A. N. Oraevsky, M. Scully, and V. L. Velichansky, “Quantum dot laser,” *Quantum electronics*, vol. 28, no. 3, pp. 203–208, 1998.
- [3] C.-Z. Ning, “Semiconductor nanolasers,” *Physica Status Solidi (b)*, vol. 247, no. 4, pp. 774–788, 2010.
- [4] D. J. Bergman and M. I. Stockman, “Surface plasmon amplification by stimulated emission of radiation: Quantum generation of coherent surface plasmons in nanosystems,” *Physical Review Letters*, vol. 90, no. 2, p. 027 402, 2003.
- [5] M. T. Hill, Y.-S. Oei, B. Smalbrugge, Y. Zhu, T. De Vries, P. J. Van Veldhoven, F. W. Van Otten, T. J. Eijkemans, J. P. Turkiewicz, H. De Waardt, *et al.*, “Lasing in metallic-coated nanocavities,” *Nature Photonics*, vol. 1, no. 10, pp. 589–594, 2007.
- [6] G. Plotz, H. Simon, and J. Tucciarone, “Enhanced total reflection with surface plasmons,” *JOSA*, vol. 69, no. 3, pp. 419–422, 1979.
- [7] A. Sudarkin and P. Demkovich, “Excitation of surface electromagnetic waves on the boundary of a metal with an amplifying medium,” *Sov. Phys. Tech. Phys*, vol. 34, no. 764766, p. 57, 1989.

- [8] J. Seidel, S Grafström, and L Eng, “Stimulated emission of surface plasmons at the interface between a silver film and an optically pumped dye solution,” *Physical Review Letters*, vol. 94, no. 17, p. 177 401, 2005.
- [9] M. Noginov, V. A. Podolskiy, G Zhu, M Mayy, M Bahoura, J. Adegoke, B. Ritzo, and K Reynolds, “Compensation of loss in propagating surface plasmon polariton by gain in adjacent dielectric medium,” *Optics Express*, vol. 16, no. 2, pp. 1385–1392, 2008.
- [10] R. F. Oulton, V. J. Sorger, T. Zentgraf, R.-M. Ma, C. Gladden, L. Dai, G. Bartal, and X. Zhang, “Plasmon lasers at deep subwavelength scale,” *Nature*, vol. 461, no. 7264, pp. 629–632, 2009.
- [11] R.-M. Ma, R. F. Oulton, V. J. Sorger, G. Bartal, and X. Zhang, “Room-temperature sub-diffraction-limited plasmon laser by total internal reflection,” *Nature Materials*, vol. 10, no. 2, pp. 110–113, 2011.
- [12] A. A. Govyadinov and V. A. Podolskiy, “Gain-assisted slow to superluminal group velocity manipulation in nanowaveguides,” *Physical Review Letters*, vol. 97, no. 22, p. 223 902, 2006.
- [13] F. van Beijnum, P. J. van Veldhoven, E. J. Geluk, M. J. de Dood, W Gert, and M. P. van Exter, “Surface plasmon lasing observed in metal hole arrays,” *Physical Review Letters*, vol. 110, no. 20, p. 206 802, 2013.
- [14] F. van Beijnum, P. J. van Veldhoven, E. J. Geluk, G. W’t Hooft, and M. P. van Exter, “Loss compensation of extraordinary optical transmission,” *Applied Physics Letters*, vol. 104, no. 6, p. 061 112, 2014.
- [15] X. Meng, J. Liu, A. V. Kildishev, and V. M. Shalaev, “Highly directional spaser array for the red wavelength region,” *Laser & Photonics Reviews*, vol. 8, no. 6, pp. 896–903, 2014.

- [16] W. Zhou, M. Dridi, J. Y. Suh, C. H. Kim, D. T. Co, M. R. Wasielewski, G. C. Schatz, T. W. Odom, *et al.*, “Lasing action in strongly coupled plasmonic nanocavity arrays,” *Nature Nanotechnology*, vol. 8, no. 7, pp. 506–511, 2013.
- [17] J. Y. Suh, C. H. Kim, W. Zhou, M. D. Huntington, D. T. Co, M. R. Wasielewski, and T. W. Odom, “Plasmonic bowtie nanolaser arrays,” *Nano Letters*, vol. 12, no. 11, pp. 5769–5774, 2012.
- [18] H.-Y. Wu, L. Liu, M. Lu, and B. T. Cunningham, “Lasing emission from plasmonic nanodome arrays,” *Advanced Optical Materials*, vol. 4, no. 5, pp. 708–714, 2016.
- [19] M. Noginov, G. Zhu, A. Belgrave, R. Bakker, V. Shalaev, E. Narimanov, S. Stout, E. Herz, T. Suteewong, and U. Wiesner, “Demonstration of a spaser-based nanolaser,” *Nature*, vol. 460, no. 7259, pp. 1110–1112, 2009.
- [20] Z.-J. Yang, N.-C. Kim, J.-B. Li, M.-T. Cheng, S.-D. Liu, Z.-H. Hao, and Q.-Q. Wang, “Surface plasmons amplifications in single Ag nanoring,” *Optics Express*, vol. 18, no. 5, pp. 4006–4011, 2010.
- [21] D. Handapangoda, I. D. Rukhlenko, M. Premaratne, and C. Jagadish, “Optimization of gain-assisted waveguiding in metal–dielectric nanowires,” *Optics Letters*, vol. 35, no. 24, pp. 4190–4192, 2010.
- [22] S. A. Maier, “Surface plasmon polaritons at metal/insulator interfaces,” *Plasmonics: Fundamentals and Applications*, pp. 21–37, 2007.
- [23] A. Trügler, *Optical properties of metallic nanoparticles*. Springer, 2011.
- [24] S. Lal, S. Link, and N. J. Halas, “Nano-optics from sensing to waveguiding,” *Nature Photonics*, vol. 1, no. 11, pp. 641–648, 2007.

- [25] P. Andrew and W. Barnes, “Energy transfer across a metal film mediated by surface plasmon polaritons,” *Science*, vol. 306, no. 5698, pp. 1002–1005, 2004.
- [26] P. Anger, P. Bharadwaj, and L. Novotny, “Enhancement and quenching of single-molecule fluorescence,” *Physical Review Letters*, vol. 96, no. 11, p. 113 002, 2006.
- [27] J. Mock, M Barbic, D. Smith, D. Schultz, and S Schultz, “Shape effects in plasmon resonance of individual colloidal silver nanoparticles,” *The Journal of Chemical Physics*, vol. 116, no. 15, pp. 6755–6759, 2002.
- [28] T. W. Ebbesen, H. J. Lezec, H. Ghaemi, T. Thio, and P. Wolff, “Extraordinary optical transmission through sub-wavelength hole arrays,” *Nature*, vol. 391, no. 6668, pp. 667–669, 1998.
- [29] A Degiron and T. Ebbesen, “The role of localized surface plasmon modes in the enhanced transmission of periodic subwavelength apertures,” *Journal of Optics A: Pure and Applied Optics*, vol. 7, no. 2, S90, 2005.
- [30] E. Economou, “Surface plasmons in thin films,” *Physical Review*, vol. 182, no. 2, p. 539, 1969.
- [31] J. Burke, G. Stegeman, and T Tamir, “Surface-polariton-like waves guided by thin, lossy metal films,” *Physical Review B*, vol. 33, no. 8, p. 5186, 1986.
- [32] T Onuki, Y Watanabe, K Nishio, T Tsuchiya, T Tani, and T Tokizaki, “Propagation of surface plasmon polariton in nanometre-sized metal-clad optical waveguides,” *Journal of Microscopy*, vol. 210, no. 3, pp. 284–287, 2003.
- [33] E. Verhagen, A. Polman, and L. K. Kuipers, “Nanofocusing in laterally tapered plasmonic waveguides,” *Optics Express*, vol. 16, no. 1, pp. 45–57, 2008.
- [34] K. Catchpole and A. Polman, “Plasmonic solar cells,” *Optics Express*, vol. 16, no. 26, pp. 21 793–21 800, 2008.

- [35] V. E. Ferry, M. A. Verschuuren, H. B. Li, E. Verhagen, R. J. Walters, R. E. Schropp, H. A. Atwater, and A. Polman, "Light trapping in ultrathin plasmonic solar cells," *Optics Express*, vol. 18, no. 102, A237–A245, 2010.
- [36] P. Reineck, G. P. Lee, D. Brick, M. Karg, P. Mulvaney, and U. Bach, "A solid-state plasmonic solar cell via metal nanoparticle self-assembly," *Advanced Materials*, vol. 24, no. 35, pp. 4750–4755, 2012.
- [37] S Pillai, K. Catchpole, T Trupke, and M. Green, "Surface plasmon enhanced silicon solar cells," *Journal of Applied Physics*, vol. 101, no. 9, p. 093 105, 2007.
- [38] J. Homola, "Present and future of surface plasmon resonance biosensors," *Analytical and Bioanalytical Chemistry*, vol. 377, no. 3, pp. 528–539, 2003.
- [39] J. Homola, S. S. Yee, and G. Gauglitz, "Surface plasmon resonance sensors: Review," *Sensors and Actuators B: Chemical*, vol. 54, no. 1, pp. 3–15, 1999.
- [40] A Melikyan, L Alloatti, A Muslija, D Hillerkuss, P. Schindler, J Li, R Palmer, D Korn, S Muehlbrandt, D. Van Thourhout, *et al.*, "High-speed plasmonic phase modulators," *Nature Photonics*, vol. 8, no. 3, pp. 229–233, 2014.
- [41] N Pala and M. Shur, "Plasmonic terahertz detectors for biodetection," *Electronics Letters*, vol. 44, no. 24, pp. 1391–1392, 2008.
- [42] A. J. Haes and R. P. Van Duyne, "A nanoscale optical biosensor: Sensitivity and selectivity of an approach based on the localized surface plasmon resonance spectroscopy of triangular silver nanoparticles," *Journal of the American Chemical Society*, vol. 124, no. 35, pp. 10 596–10 604, 2002.
- [43] K. A. Willets and R. P. Van Duyne, "Localized surface plasmon resonance spectroscopy and sensing," *Annu. Rev. Phys. Chem.*, vol. 58, pp. 267–297, 2007.



- [44] F. Beck, A. Polman, and K. Catchpole, “Tunable light trapping for solar cells using localized surface plasmons,” *Journal of Applied Physics*, vol. 105, no. 11, p. 114310, 2009.
- [45] T. Temple, G. Mahanama, H. Reehal, and D. Bagnall, “Influence of localized surface plasmon excitation in silver nanoparticles on the performance of silicon solar cells,” *Solar Energy Materials and Solar Cells*, vol. 93, no. 11, pp. 1978–1985, 2009.
- [46] N. Lawandy, “Localized surface plasmon singularities in amplifying media,” *Applied Physics Letters*, vol. 85, no. 21, pp. 5040–5042, 2004.
- [47] K. S. Yee *et al.*, “Numerical solution of initial boundary value problems involving maxwells equations in isotropic media,” *IEEE Trans. Antennas Propag*, vol. 14, no. 3, pp. 302–307, 1966.
- [48] A. Taflove, S. C. Hagness, *et al.*, “Computational electrodynamics: The finite-difference time-domain method,” *Norwood, 2nd Edition, MA: Artech House, 1995*, 1995.
- [49] K. S. Kunz and R. J. Luebbers, *The finite difference time domain method for electromagnetics*. CRC press, 1993.
- [50] J.-P. Berenger, “A perfectly matched layer for the absorption of electromagnetic waves,” *Journal of Computational Physics*, vol. 114, no. 2, pp. 185–200, 1994.
- [51] J. A. Roden and S. D. Gedney, “Efficient implementation of the uniaxial-based PML media in three-dimensional nonorthogonal coordinates with the use of the fdtd technique,” *Microwave and Optical Technology Letters*, vol. 14, no. 2, pp. 71–75, 1997.

- [52] C. M. Rappaport, “Perfectly matched absorbing boundary conditions based on anisotropic lossy mapping of space,” *IEEE Microwave and Guided Wave Letters*, vol. 5, no. 3, pp. 90–92, 1995.
- [53] W. Yu and R. Mittra, “A conformal finite difference time domain technique for modeling curved dielectric surfaces,” *IEEE Microwave and Wireless Components Letters*, vol. 11, no. 1, pp. 25–27, 2001.
- [54] P. B. Johnson and R.-W. Christy, “Optical constants of the noble metals,” *Physical Review B*, vol. 6, no. 12, p. 4370, 1972.
- [55] S.-H. Chang and A. Taflove, “Finite-difference time-domain model of lasing action in a four-level two-electron atomic system,” *Optics Express*, vol. 12, no. 16, pp. 3827–3833, 2004.
- [56] A. Boltasseva, T. Nikolajsen, K. Leosson, K. Kjaer, M. S. Larsen, and S. I. Bozhevolnyi, “Integrated optical components utilizing long-range surface plasmon polaritons,” *Journal of Lightwave Technology*, vol. 23, no. 1, p. 413, 2005.
- [57] P. Berini, “Long-range surface plasmon polaritons,” *Advances in Optics and Photonics*, vol. 1, no. 3, pp. 484–588, 2009.
- [58] H. Bethe, “Theory of diffraction by small holes,” *Physical Review*, vol. 66, no. 7-8, p. 163, 1944.
- [59] R. Gordon, D. Sinton, K. L. Kavanagh, and A. G. Brolo, “A new generation of sensors based on extraordinary optical transmission,” *Accounts of Chemical Research*, vol. 41, no. 8, pp. 1049–1057, 2008.
- [60] W. Gao, J. Shu, K. Reichel, D. V. Nickel, X. He, G. Shi, R. Vajtai, P. M. Ajayan, J. Kono, D. M. Mittleman, *et al.*, “High-contrast terahertz wave modulation by gated graphene enhanced by extraordinary transmission through ring apertures,” *Nano Letters*, vol. 14, no. 3, pp. 1242–1248, 2014.

- [61] A. G. Brolo, R. Gordon, B. Leathem, and K. L. Kavanagh, “Surface plasmon sensor based on the enhanced light transmission through arrays of nanoholes in gold films,” *Langmuir*, vol. 20, no. 12, pp. 4813–4815, 2004.
- [62] S. H. Lee, T. W. Johnson, N. C. Lindquist, H. Im, D. J. Norris, and S.-H. Oh, “Linewidth-optimized extraordinary optical transmission in water with template-stripped metallic nanohole arrays,” *Advanced Functional Materials*, vol. 22, no. 21, pp. 4439–4446, 2012.
- [63] K. Van der Molen, F. Segerink, N. Van Hulst, and L Kuipers, “Influence of hole size on the extraordinary transmission through subwavelength hole arrays,” *Applied Physics Letters*, vol. 85, no. 19, pp. 4316–4318, 2004.
- [64] K. Van der Molen, K. K. Koerkamp, F. Segerink, N. Van Hulst, S Enoch, and L Kuipers, “Shape resonances in extraordinary transmission,” in *EQEC’05. European Quantum Electronics Conference, 2005.*, IEEE, 2005, p. 339.
- [65] K. K. Koerkamp, S. Enoch, F. Segerink, N. Van Hulst, and L Kuipers, “Strong influence of hole shape on extraordinary transmission through periodic arrays of subwavelength holes,” *Physical Review Letters*, vol. 92, no. 18, p. 183 901, 2004.
- [66] K. Van der Molen, K. K. Koerkamp, S. Enoch, F. Segerink, N. Van Hulst, and L Kuipers, “Role of shape and localized resonances in extraordinary transmission through periodic arrays of subwavelength holes: Experiment and theory,” *Physical Review B*, vol. 72, no. 4, p. 045 421, 2005.
- [67] R. Gordon and P. Marthandam, “Plasmonic bragg reflectors for enhanced extraordinary optical transmission through nano-hole arrays in a gold film,” *Optics Express*, vol. 15, no. 20, pp. 12 995–13 002, 2007.

- [68] Y. Cui, J. Hu, and S. He, “Nanocavity antenna array for enhancing extraordinary optical transmission of light through a metallic nanoslit,” *JOSA B*, vol. 26, no. 11, pp. 2131–2135, 2009.
- [69] Y. Cui and S. He, “Enhancing extraordinary transmission of light through a metallic nanoslit with a nanocavity antenna,” *Optics Letters*, vol. 34, no. 1, pp. 16–18, 2009.
- [70] W. Yue, Z. Wang, Y. Yang, J. Li, Y. Wu, L. Chen, B. Ooi, X. Wang, and X.-x. Zhang, “Enhanced extraordinary optical transmission (EOT) through arrays of bridged nanohole pairs and their sensing applications,” *Nanoscale*, vol. 6, no. 14, pp. 7917–7923, 2014.
- [71] P. Melentiev, A. Afanasiev, A. Kuzin, A. Zablotskiy, A. Baturin, and V. Balykin, “Single nanohole and photonic crystal: Wavelength selective enhanced transmission of light,” *Optics Express*, vol. 19, no. 23, pp. 22 743–22 754, 2011.
- [72] I. V. Treshin, V. V. Klimov, P. N. Melentiev, and V. I. Balykin, “Optical tamm state and extraordinary light transmission through a nanoaperture,” *Physical Review A*, vol. 88, no. 2, p. 023 832, 2013.
- [73] H Ohno, E. Mendez, J. Brum, J. Hong, F Agulló-Rueda, L. Chang, and L Esaki, “Observation of Tamm states in superlattices,” *Physical Review Letters*, vol. 64, no. 21, p. 2555, 1990.
- [74] A. Kavokin, I. Shelykh, and G. Malpuech, “Optical tamm states for the fabrication of polariton lasers,” *Applied Physics Letters*, vol. 87, no. 26, p. 261 105, 2005.
- [75] M Kaliteevski, I Iorsh, S Brand, R. Abram, J. Chamberlain, A. Kavokin, and I. Shelykh, “Tamm plasmon-polaritons: Possible electromagnetic states at the interface of a metal and a dielectric bragg mirror,” *Physical Review B*, vol. 76, no. 16, p. 165 415, 2007.

- [76] H. Zhou, G. Yang, K. Wang, H. Long, and P. Lu, “Multiple optical tamm states at a metal–dielectric mirror interface,” *Optics Letters*, vol. 35, no. 24, pp. 4112–4114, 2010.
- [77] A. Kavokin, I. Shelykh, and G Malpuech, “Lossless interface modes at the boundary between two periodic dielectric structures,” *Physical Review B*, vol. 72, no. 23, p. 233 102, 2005.
- [78] I. A. Sukhoivanov and I. V. Guryev, *Photonic crystals: Physics and practical modeling*. Springer, 2009, vol. 152.
- [79] H. Zhou, G. Yang, K. Wang, H. Long, and P. Lu, “Multiple optical Tamm states at a metal–dielectric mirror interface,” *Optics Letters*, vol. 35, no. 24, pp. 4112–4114, 2010.
- [80] Y.-S. Huang, S.-Y. Hu, C.-C. Huang, Y.-C. Lee, J.-W. Lee, C.-C. Chang, Z.-K. Wun, and K.-K. Tiong, “Incident-angle-dependent reflectance in distributed Bragg reflectors fabricated from ZnO/MgO multilayer films,” *Optical Review*, vol. 21, no. 5, pp. 651–654, 2014.